

University of Windsor

Scholarship at UWindor

Electronic Theses and Dissertations

Theses, Dissertations, and Major Papers

Winter 2014

Virtual methodology for predicting whistling noise over the front grill of a vehicle

Tyler Bevan
University of Windsor

Follow this and additional works at: <https://scholar.uwindsor.ca/etd>



Part of the [Mechanical Engineering Commons](#)

Recommended Citation

Bevan, Tyler, "Virtual methodology for predicting whistling noise over the front grill of a vehicle" (2014). *Electronic Theses and Dissertations*. 5010.
<https://scholar.uwindsor.ca/etd/5010>

This online database contains the full-text of PhD dissertations and Masters' theses of University of Windsor students from 1954 forward. These documents are made available for personal study and research purposes only, in accordance with the Canadian Copyright Act and the Creative Commons license—CC BY-NC-ND (Attribution, Non-Commercial, No Derivative Works). Under this license, works must always be attributed to the copyright holder (original author), cannot be used for any commercial purposes, and may not be altered. Any other use would require the permission of the copyright holder. Students may inquire about withdrawing their dissertation and/or thesis from this database. For additional inquiries, please contact the repository administrator via email (scholarship@uwindsor.ca) or by telephone at 519-253-3000ext. 3208.

VIRTUAL METHODOLOGY FOR PREDICTING WHISTLING NOISE OVER THE FRONT GRILL
OF A VEHICLE

by
Tyler Bevan

A Thesis
Submitted to the Faculty of Graduate Studies
through Mechanical Engineering
in Partial Fulfillment of the Requirements for
the Degree of Master of Science at the
University of Windsor

Windsor, Ontario, Canada

2013

© 2013 Tyler Bevan

VIRTUAL METHODOLOGY FOR PREDICTING WHISTLING NOISE OVER THE FRONT GRILL
OF A VEHICLE

by
Tyler Bevan

APPROVED BY:

Dr. R. Barron
Department of Mathematics and Statistics

Dr. G. Rankin
Department of Mechanical Automotive and Materials Engineering

Dr. R. Carriveau, Co-advisor
Department of Civil and Environmental Engineering

Dr. D. Ting, Co-advisor
Department of Mechanical Automotive and Materials Engineering

April 30th, 2013

AUTHOR'S DECLARATION OF ORIGINALITY

I hereby certify that I am the sole author of this thesis and that no part of this thesis has been published or submitted for publication.

I certify that, to the best of my knowledge, my thesis does not infringe upon anyone's copyright nor violate any proprietary rights and that any ideas, techniques, quotations, or any other material from the work of other people included in my thesis, published or otherwise, are fully acknowledged in accordance with the standard referencing practices. Furthermore, to the extent that I have included copyrighted material that surpasses the bounds of fair dealing within the meaning of the Canada Copyright Act, I certify that I have obtained a written permission from the copyright owner(s) to include such material(s) in my thesis and have included copies of such copyright clearances to my appendix.

I declare that this is a true copy of my thesis, including any final revisions, as approved by my thesis committee and the Graduate Studies office, and that this thesis has not been submitted for a higher degree to any other University or Institution.

ABSTRACT

This research presents an approach in predicting the presence of a noise source generated by the external flow around a fin-like member of a vehicle front grill. The goal was to determine if a low-resource computational method could be used to capture the pressure fluctuations related to the noise frequencies audible during experimental evaluations on the geometry. Two nearly identical profiles were studied where one would generate wind noise in the presence of high velocity flow and the other would not. Several simulations were run on both shapes in four arrangements using incompressible and compressible solvers in attempts to determine an accurate and efficient way in capturing the phenomenon. Results have shown that incompressible cases will only capture the pressure fluctuations of shedding vortices and that a compressible simulation of multiple profiles arranged similar to the construction of the actual grill component generates results closest to those of the experiments.

ACKNOWLEDGEMENTS

Firstly, I would like to thank Dr. Peter Frise and the Auto 21 organization at University of Windsor for providing me with the unique opportunity to study abroad and conduct research both current and relative to the automotive industry. Their support with the formalities of paperwork and requirements required for graduation, over and above the awarding of partial funding for research, was greatly appreciated and cannot be emphasized enough.

I would also like to thank my University of Windsor co-advisors Dr. Rupp Carriveau and Dr. David Ting for their patience, guidance and support through the completion of this thesis and other topics of research that have come before.

Many thanks go out to Mohammed Malik for his continual support in developing an interesting research package with Kumar Srinivasan and for his knowledge and inspiration reaching beyond the scope of this research

A thank you goes out to Tony Mancini and again Mohammed Malik for arranging resources and partial funding on behalf of the industry partner for this research.

Thanks are extended overseas to the affiliates of the industry partner for their hospitality for the second phase my research. I would like to thank Enrico Ribaldone and Mauro Casella for their guidance and support in the development and implementation of the research methodology.

Thanks are also due to Professor Firrao and Professor Giovanni Belingardi of the Politecnico Di Torino for their collaboration in developing and supporting this dual degree program.

Finally I would like to thank my advisors from the Politecnico, Dr. Giancarlo Genta and Dr. Renzo Arina, for their resources and knowledge available to me throughout my research.

TABLE OF CONTENTS

AUTHOR'S DECLARATION OF ORIGINALITY	iii
ABSTRACT	iv
ACKNOWLEDGEMENTS	v
LIST OF TABLES	viii
LIST OF FIGURES	ix
LIST OF ABBREVIATIONS/SYMBOLS	xii
CHAPTER I INTRODUCTION	1
Background	1
Definition of the Problem	2
Objectives	4
CHAPTER II REVIEW OF THE LITERATURE	5
CFD Solvers	5
Turbulence Models	8
Wall Functions	10
CFD Domain	11
CFD Mesh	12
Aeroacoustics	13
FFT Analysis	18
OpenFOAM	19
Alternative CFD Codes	23
Summary	27
CHAPTER III METHODOLOGY	29
Geometry	29
Domains	30
BlockMesh	34
Fluid Mechanics	36
Boundaries	37

SnappyHexMesh	39
ControlDict	47
Solving the Simulations	50
Simulation Runtime Study	53
Time Step Study	53
Mesh Refinement Study	55
CHAPTER IV RESULTS	57
Simulation Runtime Study	57
Time Step Study	60
Mesh Refinement Study	61
Computational Time	66
Simulation Outputs	68
Power Spectral Density Analysis	78
CHAPTER V DISCUSSION	88
CHAPTER VI CONCLUSION	99
Recommendations	99
REFERENCES	103
APPENDICES	107
Sample BlockMeshDict (CASE 1A)	107
Sample SnappyHexMeshDict (CASE 1A)	109
Sample LESProperties (CASE 1A)	113
Sample turbulenceProperties (CASE 1A)	114
Sample transportProperties (CASE 1A)	115
Sample thermophysicalProperties (CASE 4A)	116
Sample controlDict (CASE1A)	117
Sample fvSchemes (CASE 1A)	120
Sample fvSolution (CASE 1A)	122
VITA AUCTORIS	126

LIST OF TABLES

Table 1: Three Variations of the Simulation Domain.....	31
Table 2: Final Refinement Region Levels	43
Table 3: Mesh Quality Control Parameters	47
Table 4: List of Simulations	48
Table 5: RAS Solver Settings.....	52
Table 6: DES Solver Settings.....	53
Table 7: Mesh Characteristics and Computation Time.....	67

LIST OF FIGURES

Figure 1: Front Grill Structure	30
Figure 2: Original Horizontal Fin Cross-section.....	32
Figure 3: Effects of Symmetry Boundary Conditions.....	34
Figure 4: Effect of Cyclic Boundary Conditions.....	34
Figure 5: BlockMesh Structures of the Three Domain Sizes.....	35
Figure 6: Spectral Density Graph of Experimental Tests	36
Figure 7: Experimental Setup for Flow Test on Isolated Front Grill Component	37
Figure 8: Revised Horizontal Fin Cross-section.....	40
Figure 9: Initial Refinement Regions.....	42
Figure 10: Example Castellated Mesh for Revised Profile	44
Figure 11: Example Snapped Mesh for Revised Profile	45
Figure 12: Example Boundary Layer Mesh for Revised Profile.....	45
Figure 13: Probe Locations	51
Figure 14: Case 1A RAS Velocity Field.....	57
Figure 15: Case 1A DES Velocity Field.....	58
Figure 16: Probe Location Comparison.....	59
Figure 17: Simulation Runtime Study	59
Figure 18: Time Step Study	61
Figure 19: Case 1A RAS Mesh	62
Figure 20: Case 1A RAS Mesh Enlarged	63
Figure 21: Case 1A DES Mesh Enlarged	63
Figure 22: Case 1A DES Mesh Step Region	65
Figure 23: Case 1B DES Mesh Step Region	65
Figure 24: Case 2A and Case 3A DES Meshes Enlarged	66
Figure 25: Case 4A DES Mesh Enlarged	66
Figure 26: Case 1A DES Velocity Field Enlarged.....	68
Figure 27: Case 1A DES Pressure Field.....	69

Figure 28: Case 2A DES Velocity Field Enlarged.....	69
Figure 29: Case 2A DES Pressure Field.....	70
Figure 30: Case 4A DES Velocity Field Enlarged.....	70
Figure 31: Case 4A DES Pressure Field.....	71
Figure 32: Case 1C Compressible DES Velocity Field	72
Figure 33: Case 1C Compressible DES Velocity Field Enlarged.....	73
Figure 34: Case 1C Compressible DES Pressure Field	73
Figure 35: Case 1D Compressible DES Pressure Field.....	74
Figure 36: Case 4C Compressible DES Velocity Field	75
Figure 37: Case 4C Compressible DES Pressure Field	76
Figure 38: Case 4D Compressible DES Velocity Field.....	77
Figure 39: Case 4D Compressible DES Pressure Field.....	77
Figure 40: Case 1A DES Probe Measurements	78
Figure 41: Case 2A DES Probe Measurements	79
Figure 42: Case 3B DES Probe Measurements.....	80
Figure 43: Case 4A DES Probe Measurements	81
Figure 44: Case 1C Compressible DES Probe Measurements.....	82
Figure 45: Case 1C Compressible DES Probe Measurements.....	82
Figure 46: Case 1D Compressible DES Probe Measurements	83
Figure 47: Case 1D Compressible DES Probe Measurements	83
Figure 48: Case 1D Compressible DES Probe Measurements	84
Figure 49: Case 4C Compressible DES Probe Measurements.....	85
Figure 50: Case 4C Compressible DES Probe Measurements.....	86
Figure 51: Case 4D Compressible DES Probe Measurements	86
Figure 52: Case 4D Compressible DES Probe Measurements	87
Figure 53: Case 4D Compressible DES Probe Measurements	87
Figure 54: Results of Experimental Tests.....	88
Figure 55: Case 4C versus Case 4D Compressible DES Probe Measurements.....	90
Figure 56: Case 4C Simulation Pressure at 0 Degrees Probe.....	91

Figure 57: Case 4D Simulation Pressure at 0 Degrees Probe	91
Figure 58: A-Weighted Curve.....	93
Figure 59: Case 4C Probe Sound Pressure Levels	95
Figure 60: Case 4D Probe Sound Pressure Levels	95
Figure 61: Case 4D Pressure Wave Propagation.....	96
Figure 62: Pressure Field over Mesh Resolution	97

LIST OF ABBREVIATIONS/SYMBOLS

AAA	Aeroacoustic Analogies
CAA	- Computational Aero-Acoustics
CAD	- Computer Aided Design
CFD	- Computational Fluid Dynamics
DES	- Detached Eddy Simulation
DDES	- Delayed Detached Eddy Simulation
DFT	- Discrete Fourier Transform
DNS	- Direct Numerical Simulation
FFT	- Fast Fourier Transform
GCI	- Grid Convergence Index
GIS	- Grid-Induced separation
HRN	- Low Reynolds Number
LBM	- Lattice-Boltzmann Method
LEE	Linearized Euler Equations
LES	- Large Eddy Simulation
LRN	- Low Reynolds Number
OpenFOAM	- Open Source Field Operation and Manipulation
PSD	- Power Spectral Density
RAS	- Reynolds Averaged Simulation
RANS	- Reynolds Averaged Navier-Stokes
SGS	- Sub-Grid Scale
STL	- Stereo Lithography
TRANS	- Transient Reynolds Averaged Navier-Stokes
URANS	- Unsteady Reynolds Averaged Navier-Stokes

CHAPTER I

INTRODUCTION

Background

The automobile has rapidly evolved through many technological and innovative improvements over the last century and will experience many more for years to come. Advances in driveline efficiency and overall vehicle architecture continually improve to meet the growing demands of cleaner operation and to meet marketplace expectations of occupant comfort and safety. With these advances the road vehicles of today mechanically perform at greater highway speeds and at quieter levels than previous years. Prior development has acknowledged components, such as the driveline, as major contributors of operational noise being transmitted to the occupants and efforts to reduce their overall levels has unmasked new sources.

A predominant noise source today impacting the comfort and psychoacoustics of the passengers and, more importantly, the driver is the noise generated from the high-speed air flow over the vehicle surfaces, such as the front grill and A-pillars to name a few. With increasing speeds the level noise grows louder, possibly creating a discomfort and distraction for the operator and posing a potential threat to the safety of the vehicle occupants [1-11].

The importance of aerodynamics for road vehicle design is clearly seen as early as the beginning of the 20th century, though the mechanics were only primitively understood. Although initially implemented only in high performance experimental and race vehicles the great advances in heavier-than-air flight throughout the early 20th century exposed a deeper understanding of aerodynamics and further influenced its implementation towards vehicles destined for the assembly line. It has since become a balance of function and form, a compromise between the cosmetic appearance of the vehicle and the overall aerodynamic performance of its surfaces. Today, the task has grown from understanding the behaviours of different fluid-flow regimes over various geometries to accurately predicting the impact these geometries have within their surrounding domain.

With the advent of computer simulation the vast number of calculations to be performed on various fluid and wave equations, such as Navier-Stokes or Lighthill's, can be achieved. Such software programs are referred to as Computational Fluid Dynamics (CFD) and Computational Aero-Acoustics (CAA) codes. Through their growth many variations to these equations, and to the schemes and boundary conditions implemented to solve them, have been derived to better approximate the observed results of physical experimentation. The development of these tools has created an invaluable resource to understanding and predicting the performance of complex geometries and to reduce the number of costly physical prototypes used for testing. Though the currently available software packages have greatly improved our research and development phases for newly proposed products for the marketplace, such CFD and CAA simulations can range anywhere from days to weeks being detailed enough to capture all desired phenomena. As the scales of the finite flow domains are reduced an exponentially growing number of computational resources are required to complete an analysis in a timely manner.

Definition of the Problem

The research within this thesis was in response to a real and current issue presented by an industry partner within the automotive sector. At the time of research, one of their largest sources for noise attributed from air flow over the vehicle was emanating from the front end geometry. They believed that the component creating the high-pitch frequency in question was the front grill. The pitch was measured experimentally within a wind tunnel using a microphone and was found to be approximately 800 Hz and would steadily increase in Decibels in relation to increasing flow speeds. Such issues were present on several of their vehicles with similar grill geometry over the product line of the company. Continuous and discrete tones of this nature can result in customer complaints and dissatisfaction that could potentially harm the reputation of any company experiencing these dilemmas. The resolution for such a problem is also a major undertaking often involving costly vehicle recalls, remedies or

redesigning and retooling of the component causing the grief. The seriousness of this problem is thus evident.

The proposal for research was twofold; can an effective, quick, low resource methodology be developed for determining potential noise sources from concept CAD data and would third-party supported version of the open source code OpenFOAM be capable of achieving these goals. At the time of presenting the objectives only the frequency of the noise and the air speed used to generate it was recorded. The vehicle under observation had relevant CAD data available enabling the construction of a digital simulation to emulate the physical experimentation done. Immediate difficulties were realized such as the measurement of pressures and velocities around key components to validate the simulated data to the experimental results. Another difficulty was that the method used to measure the noise frequency could not determine spatially where it is originating from. This means that a large portion of the vehicle front end would need to be modelled to capture the behaviour of the flow around any potential source region. An analysis like this is quite computationally heavy and would take a great deal of resources to narrow down on the source region. A matter of logistics was at play as well. Being in another country using the facility of one of their affiliates would prove a challenge to send and receive digital and physical materials required for the research.

As research began at the affiliate facility it was discovered that they have conducted research for a problem of the same phenomenon for one of their vehicles. Having done extensive investigation on a similar topic, the proposed research could be tailored to use the data from this vehicle having all the necessary information previously collected from experimental evaluations. Another advantage to the alternative is that the noise source has already been determined to originate from the inner geometry of the grill, even when isolated from its surrounding assembly components. The premise for the research of this particular vehicle done by the affiliate company was that the grill had produced a continuous and discrete tone of approximately 5500 Hz, but upon revision of the tooling for this component the decibel level of this frequency peak was greatly reduced. The only geometrical differences between the original and revised

component was an introduction of a 0.1 mm step on either side of the horizontal and vertical fins towards the trailing edge of the chord length. The shape of the revised geometry was related to production process and was no way a result of aeroacoustic noise generation from the original profile. None the less the availability of experimental results for the original and revised geometry provided a good benchmark to compare the computer simulations of both cases. The proposed research goals were preserved while using the data for the alternate vehicle.

Objectives

The objectives of this research were to:

1. Create CFD simulations of both the original and revised grill component using a supported version of the open source software OpenFOAM.
2. Determine if OpenFOAM is capable of capturing the phenomenon of the discrete tone produced from the front grill through comparison with experimental data.
3. Refine a method to yield representative results in a short timeframe while using minimal computational resources.

CHAPTER II

REVIEW OF THE LITERATURE

A critical element of the research conducted was to ensure that the approach selected to accomplish our goals was not only derived from successful methods but also utilized current and efficient means for predicting noise generation and propagation. The following literature review aims to cover the various aspects of the available methods and the numerous options that can be chosen. Once adequately understanding the results of previous works an approach could be selected to efficiently and accurately simulate the phenomenon captured during experimental evaluations.

CFD Solvers

There are many CFD solvers available today capable of simulating flow characteristics of numerous scenarios, each one tailored for a specific application. Solvers can be categorized in two basic categories; compressible and incompressible, and in the case of aeroacoustic problems either category can be used. The solvers in each category can be further divided into those intended for laminar and turbulent flow. Since noise generation is strongly linked to the presence of vortices a turbulent solver was to be selected.

One method for solving the turbulence within incompressible or compressible flow regimes is to solve them directly through Direct Numerical Simulation, or DNS. This process resolves all scales of turbulent eddies within the computational mesh in which the accuracy of the computation depends on the resolution and quality of the mesh implemented. The attractive quality of this type of simulation is that it is not only capable of solving for the characteristics of flow but acoustic propagation as well [1, 12]. On the other hand, a major disadvantage to this approach is that turbulent flows of high or even moderate Reynolds numbers possess a large range of eddy sizes approaching the Kolmogorov scale requiring a very fine mesh and a large amount of computational resources [6, 7, 12-17]. These computational costs scale approximate in relation to

$Ma_t^{-4} Re^3$ where the Mach number $Ma_t = U_{rms}/a$, U_{rms} being the root mean square value of the instantaneous velocity and “a” the speed of sound [18]. Another issue with obtaining both the fluid and acoustic characteristics simultaneously is the difference in orders of magnitude between the two. The pressure fluctuations of acoustics are much smaller than that of the flow and require special treatment in terms of numerical solution methods. The solution method requires high accuracy spatial and temporal discretization to prevent washing out the small acoustic scales from the simulation [8, 14].

An inexpensive application of DNS is to compute the external flow immediately around the geometry, referred to in acoustics as near field, instead of the entire domain in which the sound waves will propagate, known as the far field. The results from the DNS simulation will be used as a noise source within the larger far field domain where a simpler method is used to efficiently compute the acoustic signal. The advantage to this procedure is the smaller amount of computer memory and storage capacity requirement, because in such cases for acoustical post processing it is enough to store the source information on the boundary of the source region instead of storing the entire volumetric source region information. This greatly enhances the post processing of the acoustic far field region [14].

A popular alternative to the DNS method altogether is to approximate the small scale turbulent eddies with the use of a turbulence model. In this approach only the large scale eddies above a cut-off value are simulated thus leading to the name Large Eddy Simulation or LES for short [8, 12, 13, 15, 19-22]. This method is much more efficient computationally than DNS however, like any method, it does have its shortcomings. LES has some highly limiting restrictions that must be adhered to with respect to the resolution of the mesh near solid boundaries. Specifically, the near-wall resolution must be of the order of $y^+ = 1$ with other dimensions similarly small. The wall y^+ is a non-dimensional distance often used in CFD to describe how coarse or fine a mesh is for a particular flow. It is the ratio between the turbulent and laminar

characteristics within a cell [23]. These restrictions make LES impractical on aerodynamic geometries due to excessively large mesh sizes required.

A method called the Detached Eddy Simulation, or DES, incorporates both the RANS and LES solvers to utilize the strength of each. The DES approach largely eliminates the near-wall problem that LES has but at the sacrifice of its inherent accuracy in the near-wall region. DES functions by implementing unsteady RANS turbulence modelling and mesh spacing in the boundary layer, while employing LES in remainder of the domain as well as in the wake regions. The RANS turbulence model that has been optimized in thin shear layer flow regions, usually using the Spalart-Allmaras turbulent model, has complete control over the solution. LES is used in regions away from wall boundary layers when eddies are too small to be computed with the local grid resolution. These small eddies are considered to be of sub-grid scale, abbreviated as SGS. The solution that DES provides can be considered a good approximation as long as the turbulent eddy scale in the boundary layer is much smaller than within the bulk flow. This is almost always found to be the case for external aerodynamic flows. DES produces a much more accurate and detailed representation of the flow when compared to traditional simulation methods, such as Reynolds-averaged approaches, without sacrificing stability even when the flow exhibits high Courant numbers [6, 8, 15, 24, 25]. This is a benefit for our research since the ability to solve flows of a high Courant number means a more coarse mesh can be used and thus reduces computational effort.

The DES approach has been modified further to perform better with flows of high Reynolds numbers and to cope with grid-induced separations (GIS) phenomena. GIS is the premature separation of flow from a wall boundary object. The separation of the flow using this code is delayed to better reflect what would actually be seen in experimental tests. For this it is called the delayed detached eddy simulation and abbreviates to DDES [25]. Though available in the version of OpenFOAM for this research, it was advised by the industry partner not to use this code for its current lack of validation.

Though used to solve turbulent flows, the RANS solver used within DES is not a good option to be implemented on its own to generate flow characteristics intended for supplying a noise source for aeroacoustic computations. It is found that RANS equations using turbulence modelling and steady-state solution algorithms can fail to capture all time and length scales important to vehicle aerodynamics [8, 15, 24, 26]. An unsteady version of RANS, known better as URANS or sometimes TRANS, has been used in place of LES with success. The equations used in RANS and URANS are the same where the major difference lies with the transient term being retained in the latter. This results in the variables being a function of not only space, as in RANS, but now of time as well. Among all these choices of solvers available and no matter which chosen it is important that the numerical scheme has low dissipation so that it doesn't damp out the acoustical waves that are of interest for aeroacoustic analysis [18].

There exists an entirely different approach from solving for the Navier-Stokes equations in simulating a flow called the Lattice-Boltzmann Method (LBM). This method calculates the propagation and collisions of fictitious particles as they move through the nodes of a lattice mesh laid over the fluid domain. If two or more particles move to occupy the same node a collision rule is allied to change the magnitude and direction of them accordingly. A streaming step is then alternately performed to translate the particles to their new position and any collisions are once again accounted for. Similarly to Navier-Stokes conserving the mass, momentum and energy of flow numerically, the collision rules within the LBM must conserve these items for each particle. Since the LBM did not appear to be available in the third-party version of OpenFOAM selected for use this method was not considered.

Turbulence Models

As it was mentioned in the previous section the ability to model the small scale turbulence rather than resolving these eddies greatly reduces the computational resources required. The scales of turbulent motion can be broken down in three classes; dissipative, inertial and anisotropic in increasing order of relative eddy size. The

theory of energy cascade primarily states that vortices decompose into smaller vortices which generate noise in higher frequency ranges. The two smaller scales can be approximated with a theoretical description based on the universal aspects they adhere to, however, the anisotropic turbulence containing the largest scales of turbulence is not universal in nature and thus turbulence theory does not apply [7].

There are many turbulence models available to approximate the small-scale turbulent eddies that can be categorized into one equation, two equation, and algebraic, or zero equation types. Algebraic models tend to be very simple and often do not account for historic effects of turbulence like diffusion or convection. Though suitable for simple flow problems or to initialize a simulation it was decided that turbulence models of this type would be ruled out as options for this research. The one equation models usually solve for turbulent kinetic energy such as Spalart-Allmaras, one of particular interest for this research. Other examples of one equation turbulence models are Prandtl's, Baldwin-Barth, Baldwin-Lomax, and Rahman-Siikonen-Agarwal. The Spalart-Allmaras model solves a transport equation for a viscous-like variable often referred to as the Spalart-Allmaras variable. This variable, $\tilde{\nu}$, is often referred to as modified turbulent viscosity and is ideally set as $\tilde{\nu} = 0$ for wall boundaries and $\tilde{\nu} = 5\nu$ in free stream for Spalart-Allmaras applications. One influencing factor for the choice of using this particular turbulence model is that its performance was refined through compressible flow analysis over an airfoil, a shape that the horizontal sections of the front grill strongly resemble. The most common turbulence models used are of the two equation type which can be further categorized into k-epsilon, k-omega and realizable. The use of two equations can account for the historic effects of the turbulent energy where the first variable is most often the turbulent kinetic energy and the second a variation of dissipation.

DES traditionally uses the Spalart-Allmaras turbulent model while achieving high numerical accuracy in comparison to simulations based on the RANS equations which, in an industrial context, use k-epsilon or similar models for the integral length scales of turbulence [24]. When comparing the turbulence models directly through drag force it

is seen that Spalart-Allmaras will quickly reach a steady state value while k-epsilon continues to oscillate, however, the mean value of this oscillation better predicts the magnitude of force [27].

Wall Functions

Wall functions are another approach to reducing the computational requirements in obtaining accurate simulation results. Several different wall function models exist to approximate the boundary layer characteristics between near-wall cells and those along the wall itself. This allows for the use of coarser boundary meshes which greatly reduces the total number of cells in the domain and coincidentally the computational time [28]. One of the simplest and earliest is the Prandtl function but experiences poor behaviour as shear stresses at the wall approach zero. Spalding used the Prandtl function as a basis in deriving a function of his own to address these issues. Another popular choice is the log-law function which states that the average velocity of a turbulent flow at a particular point is proportional to the logarithm of the distance between that position and the adjacent wall.

$$\begin{aligned}U^+ &\propto \log(y^+) & U^+ &= \frac{1}{k} \log(y^+) + C^+ \\k &= \text{Von Kàrmàn (typically 0.41)} \\C^+ &= \text{constant (5.0 for smooth walls)}\end{aligned} \tag{1}$$

Wall functions typically work best for a particular magnitude of the dimensionless variable y^+ . This variable has been discussed earlier and can be found in the CFD solvers section. The models can be generally categorized as low or high Reynolds number models, commonly abbreviated to LRN and HRN. The classical HRN wall models tend to work for y^+ values greater than 30 and LRN for values below 1. The Spalding wall function provides a good alternative by relying on LRN approach in regions of low y^+ and HRN for regions of high values. The popular Log-Law or Law-of-the-Wall model is best

suitable for HRN flows [29]. The estimated Reynolds number for all simulations was calculated to be approximately 41 000.

CFD Domain

A CFD domain is basically a container that determines the volumetric limits of an external flow simulation. The overall size of the domain and proximity of its boundaries to the encapsulated geometry will greatly affect the computational time and quality of results. Understandably, the larger the domain the more elements of a particular size are required to discretize this domain. Choosing dimensions that are just large enough to capture the desired flow characteristics will ensure the computation time per time step is optimized in relation to data quality. The minimum size of the domain achievable is one where the boundaries will not influence the flow around the geometry [30]. The distances from the geometry to the surrounding boundaries are often measured in stream-wise lengths of the body. In the case of an air foil, a shape our geometry resembles, this measurement is referred to as the chord length. The papers reviewed use distances ranging from 2.5 to 20 chord lengths to the inlet and cross-stream boundaries and 4 to 29 chord lengths to the outlet [10, 25, 31, 32].

The first major influencing factor on the domain size is whether the simulation to be conducted is of 2 dimensions or 3. There are considerable resource savings to be had if 2D can be used to confidently capture the flow characteristics of the problem at hand. A much finer mesh can be used to capture small scale phenomenon without greatly increasing the number of required calculations [19]. The program used in the research, OpenFOAM, supports both approaches however 2D can be considered to be quasi-2D since the software still requires a finite thickness normal to the plane. Though some authors of the literature reviewed for this research used 2D flow simulations the 3-dimensional nature of a tumbling eddy is neglected. If a 3D simulation was conducted and results compared to those yielded from the equivalent 2D simulation they would likely be different [1]. For this reason the research presented in this thesis used 3D simulations to more accurately capture the turbulent motion.

CFD Mesh

The structure and resolution of the grid plays an important role in the quality and flow characteristics of the simulation. Though accurate results are desired, the ideal mesh required to achieve these results would need a very large number of elements. Simply put, as more elements are introduced more calculations are needed to resolve the flow domain, thus a larger demand for computational resources and simulation time. A practical approach is to find a balance between the accuracy of the results required and the resources available. The acceptable level of accuracy versus time to compute will depend on the desired output and importance of one over the other. In the case of this research, simulation time is a key factor in determining if the procedure used for achieving our goals is successful.

A method in determining the minimal mesh resolution is to use a Grid Convergence Index, or GCI, where the resolution of the grid is gradually increased after each simulation and the results recorded. The results are often plotted against mesh resolution to form a curve which converges on a particular value. From this curve an acceptable level of deviation from the convergence value can be chosen in regards to diminishing returns on computational investment. The conference paper presented by Jones reduced the discretization errors through this process using the mean drag values of subsequent results to create the GCI [1]. A similar approach can be applied to the time step to minimize the number of steps for a desired simulation length improving overall computation time. The cut-off frequency of the resulting mesh of this process must be considered in order to obtain useful data. This is the maximum frequency of pressure and velocity fluctuations calculable and is dependent on both the mesh size and time step [7, 8, 15]. This parameter will have different local values as the mesh density varies and can be increased simply by reducing the mesh size locally. Halving the local grid dimension will double the cut-off frequency in this region. When using a second-order accurate code it was found that at least 20 cells per acoustical wavelength are required to directly resolve the propagation of pressure waves while avoid

numerical diffusion of the signal. This required number of cells becomes lower with higher order schemes. Thus it is important to indicate the noise source locations and expected frequencies in order to optimize an aeroacoustic CFD mesh for a particular scheme [7, 15, 17].

While mesh resolution is important for capturing adequate detail of the flow, the quality of the mesh is important for a robust, accurate and timely convergence of the simulation. Many mesh generation tools have algorithms that evaluate several parameters of its construction as the flow domain is discretized. Some of these items are orthogonality, face pyramid volumes, face areas, face skewness, face interpolation weights, cell volume ratio, face twist and cell determinant. If a number of cells exceeding a defined limit violates any of these set parameter values than the mesh reverts back to a previous error free state [24]. OpenFOAM shares many of these parameters within its mesh generation code where the setting used for the research presented can be found within the method of this paper.

Aeroacoustics

Aeroacoustics is the generation of noise by an object moving in a fluid, or a fluid moving around an object, and can be classified over three different regions; near field, transition region and far field. Near field is where the majority of the sources for turbulent flow are found and far field is where the sound propagates through the medium as acoustic pressure waves [1, 4]. Since it is the near field that houses the source for audible noise in far field, the focus of this research will be within the near field. It has been determined that typical source for flow induced noise is linked to turbulence intensity and the shedding vortices [10, 30]. How the flow is generated depends on the characteristics of the flow and the geometry it moves around. The resulting noise sources are either narrow band or broad band sources. Typically broad band noise contains a range of frequencies and is generally a result of turbulent flow, however, narrow band or tonal noise is often found in the presence of shedding vortices. Tonal noise can be further divided into two classes [15].

The first has a more or less statistical frequency distribution of pressure fluctuation where a particular frequency is transformed into sound and potentially amplified. These mechanisms are usually characterized by having a fixed frequency regardless of flow variation such as Helmholtz resonance, cavity resonance and Aeolian tones. Though Aeolian tones and cavity resonance have a fixed frequency over a range of flow velocities and a harmonic can be produced if the velocity change is extreme, ultimately producing a new fixed frequency for yet another range of velocities. Aeolian tones are produced by the Von Karman Vortex Street effect where the undulation of vortices induce a vibration of the geometry, often studied in flow around circular cylinders, which resonates at its natural frequency and higher harmonics. Cavities often contain two different resonance mechanisms; Helmholtz-type for the lowest frequencies and various types of acoustic resonances for the higher frequencies. The second class can be defined as having variable frequency being linearly dependent on flow velocity such as edge tones [33].

An important profile to be considered before the design of simulations used in this research is that of an airfoil or blade since the horizontal grill sections closely resemble this shape. Airfoils are often a source for noise due to the turbulent boundary layers, the wake generated and the interaction of the geometry within it particularly in the trailing edge region. The level of trailing edge noise is greater than that of turbulent flows of comparable intensity because the aeroacoustic characteristics of the convected vortices are modified by the edge, resulting in efficient conversion of flow energy to acoustic energy. The acoustic radiation is amplified drastically for eddies within one acoustic wavelength from the edge. In addition to the undulating pressures causing noise propagation these eddies and vortices can also induce blade vibration resulting in an additional source of noise [32]. The geometry used in this research can be considered to resemble a thick airfoil with physical experiments resulting in a single frequency or tone for a range of high velocity flow. Thus initial assumptions of the flow characteristics would be undulating vortices shedding from the trailing edge of the

geometry and having the majority of contribution to the noise experienced, either directly and/or through inducing vibration of the horizontal grill section.

Acoustic sources can be classified in another way important to understanding where in the spatial domain the acoustical sources are likely originating from; these are monopole, dipole, and quadrupole noise sources. Monopole sources are found at locations or boundaries where there are density changes or variations in mass influx-outflux over time. Solid surfaces where flow pressure fluctuations are found, such as shedding vortices, classify as dipole sources. Quadrupole noise is caused by the self-interaction of the flow structures within the domain [7, 15, 22]. At low Mach number flows the monopole and dipole acoustic sources dominate over the quadrupole sources and thus the latter can be ignored for scenarios like those found in this thesis [22, 26].

There are two primary approaches to solving for aerodynamic noise. The first is to use DNS to solve for all flow characteristics, including acoustics, as mentioned previously. The second involves dividing the near and far fields into two regions, each with their own set of equations. This is done quite easily at low Mach numbers since the propagation of pressure wave and sound waves are of greatly different magnitudes [12]. CFD is used to solve for the flow in the near field to provide as a noise source where its propagation is then calculated with an acoustic analogy through the far field and has yielded reasonable results with experimental measurements [1, 8, 19, 25, 32, 34].

The CFD solvers available for use in the near field can be of either incompressible or compressible nature and have been discussed earlier [1]. The two most common methods used in CAA to compute noise propagation from a source are Linearized Euler Equations (LEE) and Aeroacoustic Analogies (AAA). With the assumption of small acoustic fluctuations in comparison to the flow field and negligible viscosity effects the LEE can calculate the sound propagation using the mean stationary flow and unsteady turbulent fluctuations from a CFD analysis. AAA's are reformulated versions of the Navier-Stokes equations rearranged with the source terms on the right hand side to yield an inhomogeneous wave equation that expresses a linear wave in a medium at

rest. The sources are again derived from the transient flow field predicted from a CFD simulation. The most common AAA equation is the Lighthill analogy and the basis for most other theories created to investigate aerodynamic noise such as Curle, Ffowcs Williams Hawkins, Phillips and Lilley [8, 16].

The second method of dividing the near and far field is often used because of its numerous advantages. One advantage in separating the flow and the acoustic computation is that the two parts can be setup differently. They can use different domains, meshes and time steps. The fluid mesh domain needs only to cover the area necessary to accurately capture the flow and the area that generates source terms and typically requires a finer mesh than the acoustical domain [8, 16, 18], but the acoustical domain needs a much smaller time step in relation to mesh size to cope with the waves traveling at the speed of sound [16]. The acoustical mesh encompasses any objects that the user would like to include in evaluating their effect in the acoustical domain. The fluid and the acoustical domain do not need to cover the same space and, in fact, many acoustic analogies are inconsistent in near fields which house the vortex fluctuations. An advantage to this is that a finer mesh can be constructed in a smaller domain to more accurately capture the flow characteristics without demanding large amounts resources [16]. Depending on the formulation of the method the acoustical domain may or may not need to extend all the way to the observer [18].

There is a concern with separating the sound propagation from the sound generation such that the acoustic field cannot affect the flow field. It also ignores the effect the mean flow has on the acoustic wave propagation. In general the acoustic and the flow fields cannot be separated, however, in most low Mach numbers flows the assumption that the flow does not depend on the acoustics is useful and most aerodynamic modelling is based upon this [8, 12, 16, 18]. For our case, the flow of 28 m/s over the grill profile results in a very low Mach number 0.08 and so this approach would be applicable.

Before the results of the CFD can be used as a source for the acoustic domain an additional operation has to be performed on this data. Since the acoustical solver works

in frequency domain and the CFD solver works in the time domain the near field data needs to be transformed. This is done by computing the Discrete Fourier Transform, or DFT, of the source terms at each node. Computing the DFT directly from its definition is computationally very expensive and thus an approximate algorithm is usually used. These algorithms are called the Fast Fourier Transform or FFT [18, 19]. These results are often interpolated from the finer CFD mesh to the more coarse acoustic mesh however there are often energy losses associated with this process [19].

As it was with CFD codes there are many potential sources for error while implementing computational aeroacoustic methods that must be considered in order to avoid or at least minimized their effect. Some of these exist only within a particular analogy, for example Nilsson [18] found that Lighthill's simplification through neglecting the viscous effects in the wave propagation and the compressible portion of the equation introduces an error which is shown to be proportional to Ma^2 . These assumptions make Lighthill's equations good for incompressible simulations at low Mach numbers. For compressible flow simulations the assumption that the acoustic field is separated from the flow field becomes weaker [18, 32]. This detail is considered as the thesis presented progresses from incompressible to compressible evaluations. Other sources of errors exist in varying degrees throughout the available methods. One major source of error is dispersion and dissipation which is derived from the aeroacoustic equations and has been a major problem for commercial codes in the past. Numerical dispersion occurs when there is variation in the group velocity of a numerical scheme and numerical dissipation is a product of partial differential equation discretization. There is also acoustic dissipation which is the conversion of acoustic energy to fluid turbulence which is then converted into heat by molecular viscosity. Another consideration to account for is the reflection of outgoing acoustic, vorticity and entropy waves crossing the boundaries at the domain limits and often evident as artificial acoustical resonance. They can be acknowledged by imposing special boundary conditions designed to either absorb all the outgoing waves preventing their reflection back into the domain or allow the waves to exit. Often these types of boundaries are

not necessary for most CFD simulations though are often recommended for compressible cases. Furthermore there is the issue of spurious short waves inevitably supported by high-order schemes which must be damped or filtered out selectively to avoid polluting the solution. These waves are the erroneous propagation in the opposite direction of what is correct. Unfortunately, high order schemes result in a better representation of the actual acoustic propagation and are often preferred; 7 point optimized stencils being both very accurate and highly efficient in computational time. When a 7 point stencil is not applicable, such in situations near computational boundaries, a 5-point or a 3-point damping stencil can be used [17, 35, 36]. In numerical analysis a stencil is a group of adjacent nodes in relation to a point of interest within the discretized domain. They are commonly used to numerically solve partial differential equations such as those derived for CFD computation.

Aeroacoustic analogies have been used not only to simulate the propagation of sound waves but also in attempts to identify the location of noise sources within the domain. Though a novel idea, one particular paper in general has gone as far as to show how these analogies are completely incapable of identifying the correct source, only pointing to quadrupoles as the contributor. Tam [37] also argues how any method can accurately predict radiated noise if the source itself changes with the choice of variables or operators that describe the propagation, which differ across theories. Another concern he raises is that the analogies are not self-contained and that variables such as turbulence need to be supplied to the equations in order to obtain results. It is finally presented that turbulence plays no role in the formulation of acoustic analogies resulting in their inability to distinguish whether a flow is laminar or turbulent and thus challenges how these theories can accurately predict turbulence generated noise [37].

FFT Analysis

It is common to use an FFT to move the resulting simulated pressure characteristics from a time domain to the frequency domain. This allows us to visualize the flow in a more meaningful representation. An FFT that will accurately capture the

frequency peaks of pressure and their amplitude requires an adequate amount of data [15, 19, 26]. As it is for mesh resolution, there is a balance between simulation time and accuracy of data. A large data set means a longer simulation time and thus more computation. Again, there is a decision to be made on how to balance these two properties and is approachable in a manner similar to GCI. Authors of the papers reviewed in this thesis used simulated times from 0.1 to 1 second [7, 8, 24]. Another factor affecting the quality of an FFT is the data included in the set. For example, it takes a large number of iterations from when the simulation is started before the solution converges towards a steady set of values. This initial period needs to be eliminated from the data set in order to obtain a more accurate FFT. It is easiest if the raw data are graphed so a decision can be visually made as to where the transient part of the solution has ended [7, 24]. Since steady-state simulations do not contain time-accurate information or spectral information FFT analyses can only be applied to transient results [15].

OpenFOAM

Since the software has been predetermined for this thesis it is wise to understand its strengths and weaknesses in comparison to other popular software available which several of the papers reviewed were found to do just that.

Tóth et al [14] found that the OpenFOAM code provides only a sequential solution method for the governing equations meaning that the coupling between the momentum, pressure correction and energy equation is not satisfied accurately. It does, however, support the opportunity to modify the existing solver algorithms providing an opportunity to reduce this error at the expense of higher computational cost. They also found that the pressure-based algorithm used in OpenFOAM is showing higher dispersion and dissipation error than the density-based solution method native to the Fluent code. Unfortunately, OpenFOAM is only capable of pressure-based simulation and the associated errors are pronounced when using non-iterative time step advancement.

Piellard and Bailly [19] have found that OpenFOAM had slightly better results for their internal flow simulations when comparing frequency spectrums to results of Fluent and Argo, with exception to the mid frequency range of the results from 1000 to 1700 Hz. The solver used was of an incompressible LES type.

Takahashi et al [20] conducted research on external flow edge tones with the use of compressible LES 2D and 3D solvers within OpenFOAM to generate the source data and calculate the acoustic propagation through the use Lighthill's and Howe's vortex equations. They have chosen to perform the calculation of the flow dynamics and the sound field it generates simultaneously. This required the use of a domain large enough to capture both the near and far field behaviour. The simulations must satisfy the requirements of small time step to describe the propagation of sound and a fine enough mesh to reproduce the small scale vortices. Since the mesh construction is more impacting to the quality of results for aeroacoustics, they have used a structured mesh approach often preferred for sound propagation calculations. Their results stated that the 2D simulations accurately reflected those of the 3D analysis. They also recorded that the pitch of the noise generated increased linearly with flow velocity.

Miyamoto et al [21] used a direct approach to solve the fluid and acoustic equations simultaneously over the leading edge of a reed rather than the more commonly used hybrid approach found in most aeroacoustic evaluations. The simulations were solved for using a 2D compressible LES simulation. Further acoustic propagation analyses were performed using Lighthill's equations in which the results overlap with the shedding eddies from the reed predicted by CFD. This conclusion supports the Powell-Howe vortex sound theory that a major part of the sound created is a result of the moving vortices.

Singh et al [31] have used OpenFOAM to evaluate the flow characteristics of both an Ahmed and FSAE body with comparison to the software codes Fluent and Metacorp Technologies' CFD++. They have evaluated the speed-up, calculation time per iteration, and overall efficiency to compare OpenFOAM and CFD++ on meshes of 2 and 22 million cells using the 1024 CPU supercomputer, Eka. It was found that OpenFOAM

performed better than CFD++ for speed-up and overall efficiency however, it has a slower time per iteration thus a longer total run time. Iteration time is approximately even when more than 500 parallel CPU's are used. Steady RANS simulations with the use of a realizable k-epsilon turbulence model were completed in all three software packages and the drag coefficients used to compare the experimental results of the Ahmed body. They initially experienced some solution convergence issues which were resolved with a combination of discretization and numerical schemes. Using the OpenFOAM utility potentialFoam to initialize the fluid domain parameters over the entire mesh aided in achieving good convergence. Moving from a first order divergence scheme for the initial time steps to a second order Gauss Linear scheme also contributed to successful simulations.

Islam et al [24] performed a DES simulation in OpenFOAM over detailed structures of an automotive body and compared the results to that of an actual wind tunnel performed on the same geometry through the use of lift and drag values and select point surface pressure values. The simulations were initialized with potentialFoam and run for 2.5 seconds to flush out any iterations within the start-up transient phase, using only the final 0.25 seconds of the results. The result of the OpenFOAM proved to be a successful representation of the physical evaluations.

Baeder et al [38] used OpenFOAM to compare a RANS k-omega SST simulation and a DDES Spalart-Allmaras simulation against experimental results for fluid flow characteristics over a quarter scale SAE vehicle. The simulation time was 1.1 seconds and found, as expected, that DDES predicts the characteristics of the wake more accurately than RANS but requires more computation time.

Krastev and Bella [27] compared the realizable k-epsilon and Spalart-Allmaras turbulence models while using a URANS OpenFOAM solver called pimpleFoam to evaluate an Ahmed bluff body. RANS simulations were also provided using the simpleFoam code as a benchmark to compare results. The results revealed that Spalart-Allmaras reached steady state drag values after 0.15 seconds where the k-epsilon method was observed to continuously oscillate, however, Spalart-Allmaras was not as

accurate in predicting the magnitude. After evaluating the solvers they suggest that if time dependent information is considered an essential design parameter it would best to use an LES or hybrid solver such as DES in place of URANS.

An evaluation of an SAE super-mileage using a RANS simulation and a k-omega SST turbulence model in OpenFOAM was performed by Gagnon et al [29] resulting in relatively large prediction errors of the pressure field. This was done through applying the chosen method to an Ahmed body of known results and comparing the output. They spent a good deal of time choosing a wall model since their simulation contains a large range of y^+ values along the wall of the vehicle. Through testing of various wall models they decided to use the classical log-law wall function since it was most suitable to set the k and omega values along the wall. Though knowing that this wall model may over predict the pressure forces simulated they felt this approach would acknowledge the range of y^+ values along the geometry[29].

Wojciak et al [28] also compared the RANS and URANS solvers for flow over a car body within OpenFOAM, called simpleFoam and pimpleFoam respectively. They also used two different turbulence models; k-omega SST and realizable k-epsilon. The time step chosen was sufficiently short enough to achieve a small Courant number to maintain the pressure-velocity coupling and the total simulation time run for 0.4 seconds. They found the k-epsilon model to converge slightly faster with fewer iterations than the realizable k-epsilon. When compared to k-omega SST the k-epsilon models were more accurate, the nonlinear k-epsilon performing best when evaluating the predicted drag force. For the study of vehicle yaw within the flow, the nonlinear k-epsilon overestimated the yaw moment but the realizable k-epsilon overcame these deficiencies with much better accuracy for this parameter, including the side and down force. The overall conclusion for the use of URANS in OpenFOAM was that it does not meet the standards set by commercial CFD codes.

Alternative CFD Codes

This section provides a perspective of how other CFD codes fared in predicting flow characteristics and additional methods not covered in the OpenFOAM research previously discussed. The literature here also provides additional benchmark for parameters such as simulation time, time step and mesh sizes that were used to obtain conclusive results.

Leep-Apolloni et al [4] used the CFD code PowerFLOW to perform a RANS simulation coupled with wave number-frequency spectra for the flow regimes to calculate vibrations in order to determine the sound pressure level spectrum at the driver's ear. The time step used is directly related to the smallest wave length expected, in this case 13.2 μs was used to capture frequencies up to 38 kHz according to the Nyquist sampling theory. Acoustic data was captured for 20 periods of the lowest frequency of interest, this being 50 Hz, after eliminating the start-up period of 1000 time steps. In comparison to experimental wind tunnel data, the results demonstrated the ability of their chosen method to correctly predict both the spectral noise trends and the resulting SPL at the driver's ear with high accuracy. They mention in their conclusions that if a direct computation of the time-accurate surface pressure information was conducted, like with DNS or DES, then the actual pressure spectra could be determined instead of using the generic spectra Wind Noise Modeller provided by PowerFLOW[4].

The code SCRTU Tetra for calculating the fluid flow domain and FlowNoise for the resolution of the aeroacoustic pressure were used by Park and Lee [5] to evaluate the internal flow of an HVAC duct. The results from the RANS simulation were used for the noise source for the Ffowcs-Williams and Hawkings equations to reproduce the experimental whistling noise.

Lokhande et al [22] used a transient LES simulation within Fluent to compare the results to those of a Ffowcs-Williams Hawkings acoustic analogy. They found success with the CFD code for external flow frequencies up to 1000 Hz with a time step of 6E-05 seconds and a mesh of 3 mm along the side mirror under evaluation. An FFT was

performed on 0.078 seconds of the recorded pressure field to obtain the frequency spectra and the pressures transformed from Pa to dB. Pressure and Decibel are related with the following equation:

$$\Delta SPL = 10 \cdot \log(p_{rms}^2/p_{ref}^2) = 20 \cdot \log(p_{rms}/p_{ref}) \quad (2)$$

Where p_{rms} is the value returned from the FFT analysis and p_{ref} is the reference pressure, often set at around 20 μ Pa for air. Lokhande et al found that the SPL predicted in their CFD analysis closely represents the experimental results with a 5 dB mean deviation for most of the probe positions.

STAR-CCM+ was used by Mendonça et al [15] to evaluate the noise reduction of a landing gear modification for an aircraft. A hexahedra mesh of 0.75 mm at the object surface was used to compute 0.25 seconds of simulated flow time using several solvers. They found DES to correctly predict the noise reduction in the range of 300-10,000 Hz, however over-predicting the reduction in lower frequency ranges. The source for this inaccuracy is thought to be a result of assuming a perfectly rigid structure for the landing gear.

Using SWIFT-CFD to perform a hybrid CAA simulation Védý et al [6] determined that the results of the power spectral densities are in good agreement with most probe positions of the experimental data of a side mirror for frequencies above 400 Hz, much like Mendonça et al had noticed. The author of this paper suggested that the inaccuracies of the low frequencies may be the result of inadequate simulation time to accurately obtain the spectra through FFT.

A CFD evaluation was performed on a side mirror model using the PowerFlow software package. Lepley et al [7] used the Lattice Boltzmann Method to solve the Boltzmann equations, rather than the tradition Navier-Stokes, resolving the anisotropic turbulent scales directly while modelling the dissipative and inertial ranges with a k-epsilon turbulence model. The domain was initialized from results of a more coarse mesh simulated with uniform velocity and pressure conditions. The transient simulation

time was run for 1 second on a mesh of 1.25 mm near the geometry wall with a time step of $6.8E-6$ seconds where the first 0.4 seconds of measurements were excluded from the data used for the FFT.

A Hybrid approach was used by Ayar et al [8] using both LES and DES in Fluent as well as STAR-CD to generate the noise sources and Sysnoise to calculate the sound propagation. Most simulations performed were run for 0.5 seconds with a time step of $2E-4$ seconds. The results from the CFD run are compiled into dipole and quadrupole sources to suit the AAA and an FFT is performed to transform the data into the frequency domain to be interpolated onto the CAA mesh. It was found that the peak frequency prediction was generally more accurate than the prediction of the peak magnitude with best results from fine CFD meshes.

Kato [16] had also performed a hybrid approach using LES and Lighthill's analogy for 0.0289 seconds with a mesh resolution of 0.5 mm along the wall of the mirror. He found that this method was sufficient in accurately representing the vortices due to flow separation.

Biermeier and Becker [9] performed an acoustic analysis on an HVAC vent which resembles the array of horizontal fins of the front grill investigated in this thesis. They found that the frequency of the emitted tonality does not change with the mass flow rate but will decrease with increasing chord length and vice versa. They found a linear correlation between the normalized chord length of the flaps (relative to the height of the channel) and the normalized frequency (relative to the maximum frequency) for different mass flow rates. The authors believe it is probable that the investigated frequency is the sound decoupled from a resonating sound wave above and below the flap, possibly the same phenomenon present in the experimental results of this thesis.

Lai and Luo [39] used an LES flow simulation and Ffowcs Williams Hawkings acoustic analogy to perform a hybrid analysis on a cavity flow. The time step was chosen using a CFL number of unity which corresponds to about $2.5E-4$ seconds. They found that the shedding vortices break up into smaller ones which are irregular and

highly 3D, thus the mesh should be suited to capture the 3-dimensional nature of turbulent flow.

The SWIFT-CAA code was again used by Murad et al [34] to employ a SIMPLE solver while initially using a turbulence k-epsilon model and switching to the Reynolds Stress Model (RSM). The results were analysed through an FFT to obtain a Power Spectral Density to conclude that the code is capable of predicting the propagation of noise from the A-pillar of a vehicle for scale models.

A trailing edge evaluation was conducted in two different papers by Wang [30, 32] to directly compare the measured sound pressure spectra to that computed through a hybrid LES/Lighthill's simulation. This was done first by solving a coarse meshed domain with a RANS simulation to initialize a smaller mesh for LES computation followed by a Ffowcs Williams analogy to compute noise propagation. It was found that good agreement is achieved in the intermediate frequency range within 10 Hz and suggests that any over prediction and under prediction in the low and high frequency ranges, respectively, are likely due to the boundary layer lacking the expected small scale structures. He states, however, that this would not prove to be a problem for predicting the noise propagation. It was also noted that the shedding vortices were of a 2D nature with little motion in the direction parallel to the trailing edge. For this reason the analysis of the vortex structures perpendicular to the edge are most useful because they proved the predominant acoustic sources.

Yamamoto et al [40] performed an acoustic analysis using compressible DES with a Spalart-Allmaras turbulence model within the CFD code JAXA to evaluate an edge used in aircraft during take-off. They succeeded in obtaining the acoustic propagation, though it required narrowing the pressure field plot to a 0.002 Pa range to visualize the wave structure. A similar graphic will be generated in this research in attempts to visualize the pressure wave propagation from the noise source generated from the grill.

Li et al [10] used the code NAGARE to simulate wind flow over a vehicle. They began with a steady state solution and a large time step to initialize a mesh with elements of approximately 4 mm along the geometry surface and performed a DNS with

time steps of $1E-4$ seconds. This transient solver used diffused small vortices rendering the approach as a pseudo-direct numerical simulation where results agreed well with previous LES simulations on the same mesh.

Once again the code SCRYU was used to perform aeroacoustic analysis of the vortex shedding from the front a pillar using a frontal car model. Lighthill-Curle's equation is used by Zhu et al [26] to calculate the noise propagation after an incompressible RANS is used to provide a source. No turbulence model was used and the mesh grid was too coarse to use LES properly, however proper tuning of the spatial and temporal resolutions resulted in an efficient method to adequately predict the phenomenon. The resulting time step was $1E-4$ seconds generating a maximum Courant number of 0.4.

Greschner et al [25] performed a comparison between a hybrid IDDES-FWH analysis and experimental results for a NACA 5510 airfoil in high load and camber. A time step of $1E-6$ was used on a mesh with a grid size of 0.5 mm by 0.25 mm along the geometry surface. Their results clearly revealed the propagation of noise from the vortex structures in the turbulent boundary layer passing over the trailing edge and good agreement with the experimental results between frequencies of 1 and 5 kHz.

Summary

To conclude the literature review OpenFOAM possesses the same efficient solvers and turbulence models found in commercial codes that could provide reasonably accurate results while attempting to simulate the experimental phenomenon. A DES approach will be used in both incompressible and compressible applications and the Spalart-Allmaras turbulence model selected. The domain will encompass the cross-section of the horizontal grill members and its mesh will be of an unstructured type with fine resolution near the geometry and regions of expected vorticity wake. The boundaries will be varied over several simulations to determine if the fin array can be appropriately represented with Symmetric or Cyclic arrangements. Pressure probes will be set in array around the geometry and their recorded values

operated on with an FFT analysis in attempts to graphically capture the pressure fluctuation frequencies and their amplitudes. The specific details for all the variables involved with creating the simulations will be determined and presented in the following chapters and their results compared against the experimental phenomenon.

CHAPTER III

METHODOLOGY

The conceptual phase for the design of the simulations used to numerically evaluate the problem at hand plays a critical role in relation to the required resources and simulation time required to complete them. Many aspects must be considered such as the extent of the geometry used, domain size, mesh refinement level, boundary conditions, time step etc. Each aspect was carefully thought out to ensure that the simulations performed were efficient and would approach a solution representative of the physical phenomenon experienced.

Geometry

One of the first decisions to be made that greatly reduced the final mesh size of all the following designed simulations was the choice of geometry to be used. The size of the geometry and its bounding domain directly impacts the required resources and simulation time. Since the horizontal and vertical fins were the only areas affected from the tooling revision implemented that eliminated the generation of noise from the grill it was decided that the focus of the analysis should be on these regions. It was hypothesised that the horizontal fins would likely contribute considerably more to the noise generation than the vertical counterparts due to the closer proximity within their array. It was thought that this small distance would enable complex interactions of their individual wakes with one another. The difference in vertical and horizontal spacing is visually depicted in Figure 1. This figure also shows that the horizontal fins form a parallel array of four equally spaced bodies where each is of identical geometrical shape. The outer perimeter of the grill was excluded from the simulation for further simplification. With the assumptions and simplification imposed on the geometry it was decided that an extrusion of the horizontal cross-section would be used for the simulations. Several simulations have been run to compare the effects of one fin in

relation to an array of three. This is to determine if the noise phenomenon is the effect of complex interactions of flow from adjacent fins or if it can be recreated with only one.

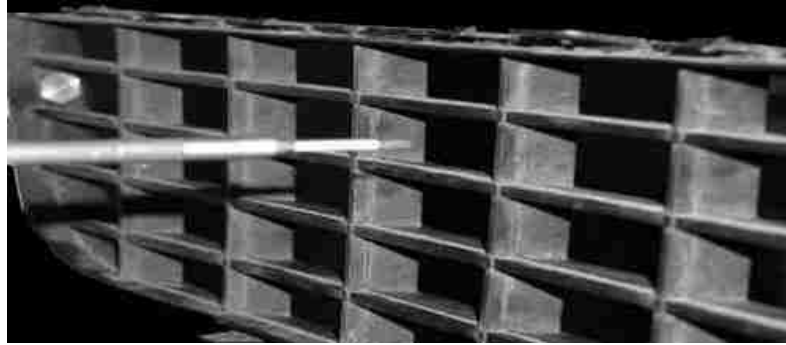


Figure 1: Front Grill Structure

Domains

The next major consideration impacting the final mesh size of each simulation is the domain in which the fluid flow will be calculated. The position of the domain boundaries must be chosen in such a way that they do not impact the flow characteristics of the fluid around the geometry. OpenFOAM offers two basic choices in creating a volume mesh for the fluid domain. The volume can either be constructed in CAD software to be imported into OpenFOAM as an STL or a basic three dimensional block, referred to as a blockMesh, can be defined using vertices within the OpenFOAM blockMeshDict dictionary file. For simplicity, the blockMesh method was chosen resulting in the location of six boundary faces to be determined.

As stated in the previous section it was planned to evaluate the differences between a single profile and an array. When considering the boundary conditions to be used in each simulation, outlined in the following section, several different approaches are available within OpenFOAM, each resulting in different boundary specifications. Firstly an array can be created with three individual bodies spaced appropriately within a single domain. The other two options are to use symmetry or cyclic boundary conditions to emulate the presence of adjacent geometry of the same dimensions. For

the particular problem being analyzed both the symmetry and cyclic boundary conditions are applied to a domain of the same dimensions. This results in the definition of three domains of different dimensions which are listed in Table 1 summarizing the distance of their boundaries from the outer most profile which will be described in detail.

	Array	Inlet	Outlet	Sides	Top and Bottom
Domain 1	Single	> 5 x Chord Length	> 10 x Chord Length	> 2 X Profile Thickness	> 5 x Chord Length
Domain 2	Symmetric/ Cyclic				0.5 x Array Offset
Domain 3	Offset				> 5 x Chord Length

Table 1: Three Variations of the Simulation Domain

The first dimension to be considered was the width of the domain which ultimately determines the width of the profile extrusion for the geometry. This was chosen to be a factor of the profile thickness being the limiting dimension for the largest eddy diameter to shed from the trailing edge of the body. This value can be found from the profile of the horizontal cross-section shown in Figure 2. Using at least twice this dimension for the distance between the domain boundaries at the extruded profile limits would reduce the possibility of these boundaries affecting the flow characteristics at the midpoint of the extruded span.

Next the inlet and outlet boundaries were determined in a similar manner using a multiple of the profile chord length. The upstream inlet boundary was chosen to be at least five chord lengths from the front edge of the profile. The outlet downstream of the trailing edge of the profile was decided to be at least ten chord lengths to allow adequate evolution of the wake in order to capture its flow characteristics.

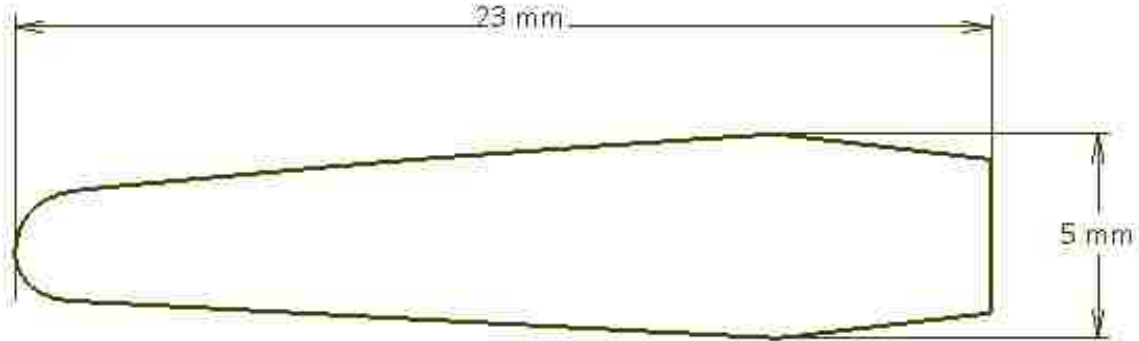


Figure 2: Original Horizontal Fin Cross-section

Finally the location of the boundaries above and below the profile is to be determined. For the cases of a single profile and the array created from geometrical offsets the boundary is once again chosen to be at least 5 chord lengths from the outermost profile to ensure they do not impinge on the fluid flow characteristics. As for the arrays created from symmetric and cyclic emulation the upper and lower boundaries need to be placed at half the array offset. The array offset refers to the distance between two adjacent horizontal profiles in the front grill of 22 mm. The chosen values of chord length distance were influence by the works of previous authors presented in the CFD Domain section of the literature review. Incompressible results for a single grill section of the original profile were obtained using the boundary positions determined for Domain 1 (Table 1) and compared to those recorded when moving the inlet, outlet, upper and lower boundaries in towards the geometry. These boundaries were moved inward by half a chord length and yielded results of no significant differences from those using the defined values in Table 1.

Symmetric boundaries function by assuming that exact values of the mesh nodes adjacent to the boundary exist beyond the domain as if looking in a mirror. Calculations performed in these regions use this premise to produce a flow that behaves as if an equal but reflected event is occurring about the boundary. This setting only works for geometry that is symmetric about a plane parallel to the boundary set with the

symmetry condition. Since the profile in question is nearly symmetrical it was deemed acceptable to compare the results of this simulation with the others. It should also be noted that just because the geometry is symmetrical does not mean that the flow will be symmetrical. The final FFT results of this approach will be compared to those of the three-fin array to determine if symmetric boundaries are a reasonable assumption.

Cyclic boundaries behave in a similar manner as symmetric but take the values adjacent to one boundary and apply them along another at the opposite end of the domain. The cyclic boundary condition is more commonly referred to as a periodic boundary condition in other CFD software codes. This method is reasonable to use on any array of geometry even if it is not symmetrical about a plane parallel to the cyclic boundaries. Figure 3 and Figure 4 show the effects of symmetrical and cyclic boundary conditions respectively. The flow is from left to right and the wake created from the presence of the geometry is represented by the two splines protruding from its trailing edge. The centerline represents the boundary assigned the condition where the dashed lines illustrate the emulated effects of another body and its wake adjacent to the actual geometry modelled and will not be actually calculated or graphically represented beyond the extent of the fluid domain. The same concept applies to the boundary at the opposite side of the domain.

The purpose of running the symmetry and cyclic array cases is to determine if they can achieve the same solution as that of the array of offset geometry. The advantage presented, if it is to work, is a much smaller fluid domain resulting in a greatly reduced mesh size. A smaller mesh will ultimately reduce computational time and resources as these are the overall goals.

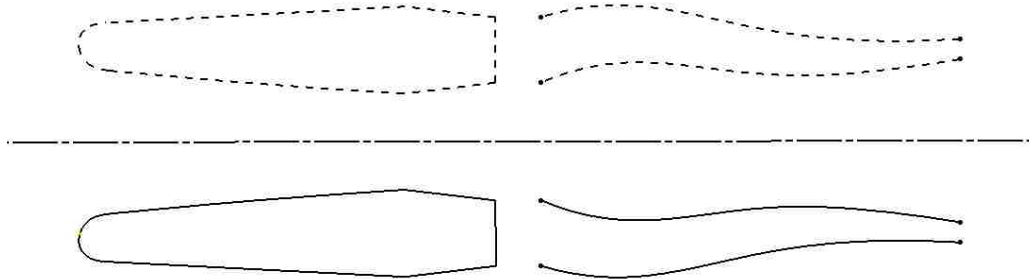


Figure 3: Effects of Symmetry Boundary Conditions

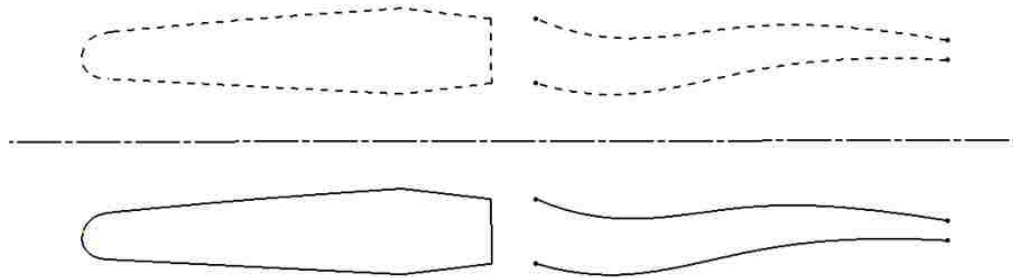


Figure 4: Effect of Cyclic Boundary Conditions

BlockMesh

The controlling factor for the actual position of the boundaries relied on the definition of the blockMesh described earlier. The final meshing process, which will be described later, involves importing the desired geometry into the blockMesh and will be meshed around in a later step. It is required for this operation that the blockMesh contains at least one interior cell face that intersects the imported geometry. It was decided that since the upper and lower boundaries for the symmetric and cyclic simulations are the only ones that require an exact location value they will determine the largest blockMesh cell size chosen for all the meshes created. This will ensure consistency of mesh resolution between simulations for comparing results against one another.

As described earlier the upper and lower boundaries need to be 11 mm from the centerline of the geometry for the cyclic and symmetric cases. Thus this dimension was chosen to be the size of the blocks to populate the blockMesh domain in a cubic fashion. Figure 5 illustrates the cell construction of the blockMesh for each simulation.

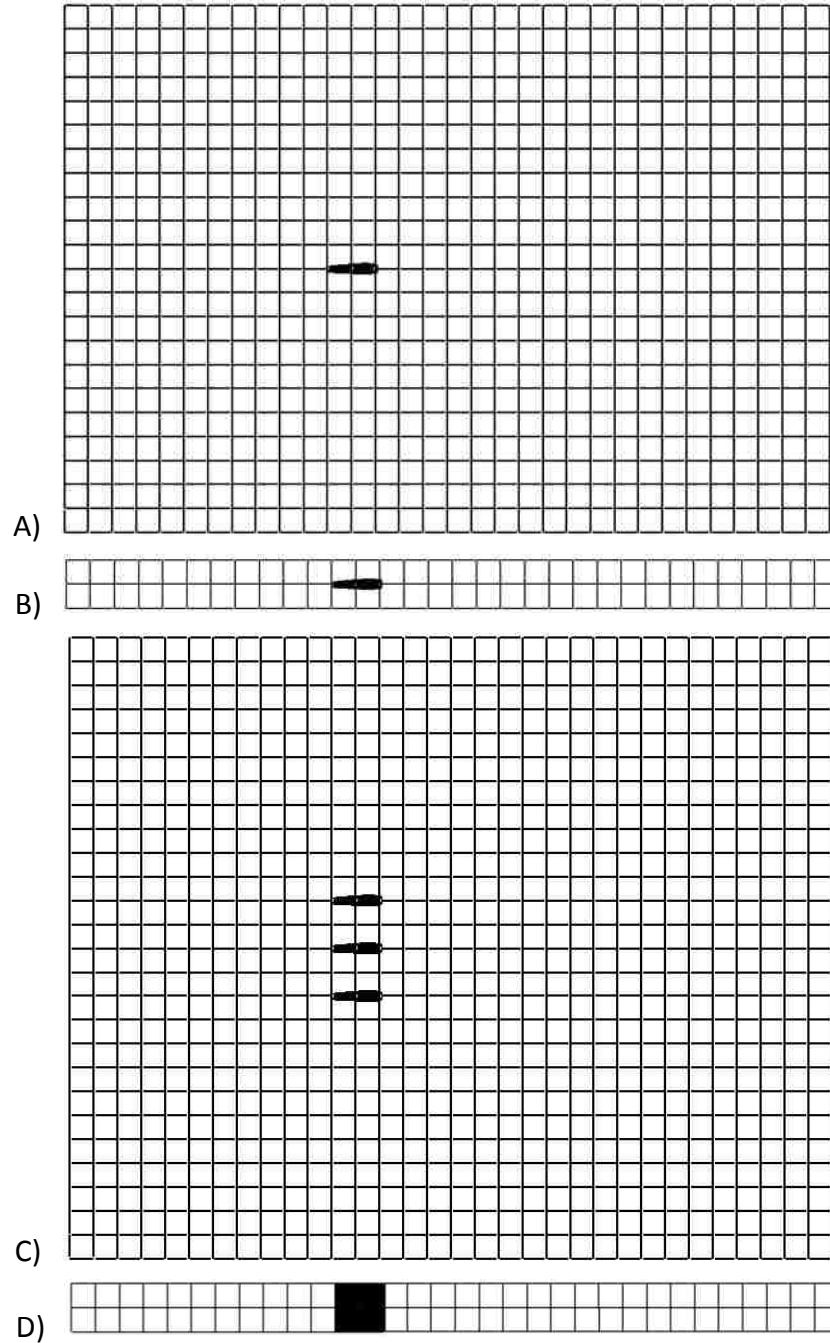


Figure 5: BlockMesh Structures of the Three Domain Sizes

A) Side view of Domain 1: Single Profile, B) Side view of Domain 2: Symmetric and cyclic, C) Side view of Domain 3: Offset Profiles, D) Top view representative of all domains. Flow is from left to right.

Fluid Mechanics

This section briefly covers the choice of using incompressible and compressible fluid equations in solving the simulations outlined earlier. It was decided to run the cases both with incompressible and compressible settings. The reason is to determine if incompressible simulations can capture the fundamental phenomenon of the problem and compare these results to that of the compressible nature. It was initially theorized that the source of the noise is due to a complex interaction of the adjacent wakes of the array and thus the related pressure fluctuations can only be accurately reproduced through a compressible fluid mechanics simulation. Though if the noise source is determined to be emanating from a single profile its local pressure fluctuations may be captured through an incompressible evaluation and the results representative of the physical phenomenon. This would pose another reduction in computational time since the set of incompressible equations is one less than that of compressible resulting in fewer calculations and shorter computation time.



Figure 6: Spectral Density Graph of Experimental Tests

Boundaries

The boundaries must be chosen carefully for they will define the characteristics of flow within the domain. The choice of incompressible or compressible flow equations within the flow domain will also require particular boundary conditions to be applied.

This first boundary condition to be considered is the inlet. Physical testing of the front grill noise was conducted at flow velocities ranging from 90 to 120 km/h (25.0 to 33.3 m/s) and achieved a discrete tone of the same frequency between 95 and 105 km/h (26.4 and 29.2 m/s) as shown in Figure 6, the spectral density graph for the experimental testing. Figure 7 shows the setup used to perform the flow tests on the isolated front grill component. It was thus decided that a uniform and fixed inlet speed of 100 km/h (27.8 m/s) will be used for all simulations.



Figure 7: Experimental Setup for Flow Test on Isolated Front Grill Component

The outlet to complement the presence of an inlet is found at the opposite side of the inlet and will have two different settings amongst the simulations. For the incompressible analyses the outlet is set with a uniform and fixed pressure of 0 Pa since the mechanics of incompressible flow only depend on pressure gradients and not absolute values of pressure. For the compressible simulations it is required that the initial pressure conditions at the boundaries and throughout the domain are approximated close to ambient values. The outlet is revised from a fixed and uniform value of 0 Pa to a wave transmissive boundary condition with uniform initial values of 100 kPa. The initial conditions for the interior mesh nodes are also assigned this value.

Transmissive boundary conditions will allow the pressure wave to “pass through and leave” the domain as opposed to be reflected back as with the other options available. For them to work properly the gamma value for air and the frequency of pressure fluctuation need to be supplied. These values should be a good estimate of what is expected at the solution of the simulation.

The boundaries at the sides of the domain that limit the extrusion of the profile are again consistent across all simulations and set as symmetry planes. This will treat the domain to be solved as if the fin is extruded beyond the limits of the boundary positions.

The choices for the top and bottom boundaries are what impact the behaviour of the model the most regarding the research being conducted. For the simulations containing the single and three fin profiles these boundaries are once again set as symmetry planes. Their relatively far-field position from the geometry will have little effect on the local flow around the region of predicted noise generation. There are several other boundary setting that could have been selected for this simulation, however, the symmetry plane will achieve nearly the same results in the flow domain around the profile and are easiest to implement. For the analysis evaluating the effects of an array through the use of symmetry undoubtedly uses symmetry planes for the top and bottom planes as well. The only difference between the single fin domain and the symmetry array is the proximity of the upper and lower boundaries to the geometry.

These boundaries of the latter will have a definite impact on the flow characteristics around the horizontal grill section acting as if in the presence of others both above and below. The upper and lower boundaries for the cyclic array are set simply as having cyclic conditions and work as described throughout the previous sections. As it was for the outlet in compressible flow simulation these boundaries have different settings than those used for incompressible. The ideal condition for these boundaries that would yield the most realistic results would be those of wave transmissive. Wave transmissive conditions can only be set on boundaries defined as outlets and so all compressible simulations have the same values and parameters for the upper, lower and outlet boundaries. This non-reflective boundary condition was chosen for its availability within OpenFOAM and support from the third party software provider on its use.

The final boundary to be defined was for the surfaces of the geometry to be removed from the fluid domain. This was simply set as a wall with a no slip velocity condition and zero pressure gradients. It should be clarified that the zero pressure gradient boundary condition option available in OpenFOAM is applied perpendicular to the wall and not along the wall as the following equations show.

$$\vec{\nabla}p \cdot \hat{n} = \begin{pmatrix} \frac{\partial p}{\partial x} \\ \frac{\partial p}{\partial y} \end{pmatrix} \cdot \begin{pmatrix} 0 \\ 1 \end{pmatrix} = \frac{\partial p}{\partial y} = 0 \quad (3)$$

\hat{n} = a vector normal to a horizontal boundary

SnappyHexMesh

Once the domain and boundaries have been defined the surfaces listed in the STL representing the geometry of the fin can be removed from the blockMesh domain. This is done with the OpenFOAM utility called snappyHexMesh which creates hexahedral mesh within the defined domain. The mesh is then decomposed into tetrahedral and pyramid elements using the center positions of the cell volume and cell faces of the hexahedral entities. The controls for this application are defined in the

snappyHexMeshDict and are used to determine boundary layers, mesh refinement regions and mesh quality.

As mentioned earlier all the simulations were performed twice, each on two different but very similar geometries resembling the profile of the horizontal grill fin before and after the tooling revision. Where Figure 2 illustrates the profile of the original fin Figure 8 highlights the differences between the two geometries used within the circled regions. The overall length and width of the profiles remain constant between the two geometries.

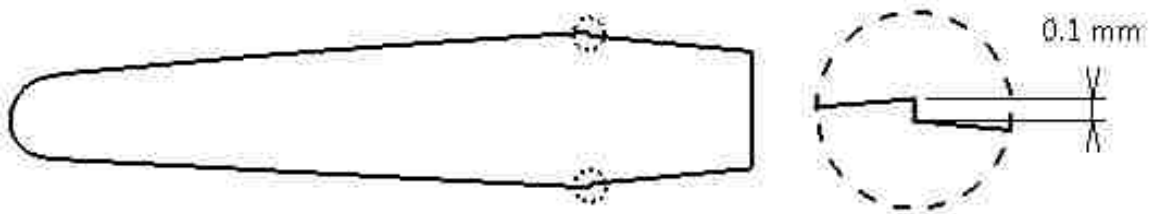


Figure 8: Revised Horizontal Fin Cross-section

SnappyHexMesh creates the desired mesh in four fundamental steps. The first step performs mesh refinements in the regions defined by the user inputs into the snappyHexMeshDict. The regions can be defined as the volume within a sphere or block of given coordinates and dimensions. Since the blockMesh domains created are of rectangular shape and the flow is mostly unidirectional the refinement regions will also be rectangular.

The refinement method with this OpenFOAM automated meshing utility works on a definition of levels. Level 0 refers to the largest and most coarse cell sizes present in the mesh. Since the blockMesh cells were created with equal sides of 11 mm this will be the largest cell size found in the domain and is assigned Level 0. As the levels progress numerically the length of each cell face is halved. In the case of the cells used in this research Level 1 will have cubes one half the length of Level 0. Level 2 will have cubes one half the length of Level 1, or one quarter the length of Level 0 and continues like this to the final and highest level. The simulations in this research all use a basic set

of regions common across them. To capture the geometric detail around the profile being analyzed three regions surround the shape with increasing levels of refinement and one refinement region to capture the detail of the flow characteristics within the wake of the object. Figure 9 shows a side view of the initial generic refinement regions used for all simulations which are extruded the entire width of the domain. The graphic is only a section of the mesh and extends beyond the dash perimeter shown.

Image A contains two horizontal dashed lines through the domain to represent the extent of the domain for both the symmetric and cyclic array simulations. The two small regions on either side of the profile labeled Step Refinement Regions are used to further increase the mesh resolution around the revised geometry to improve the detailed captured and thus are not present for the domains housing the original geometry. It must be pointed out that the refinement level of the cells contacting the profile can also be defined and assigned a thickness in number of cell layers. The initial levels of refinement for all regions was selected on the basis of capturing adequate detail of the geometry and was evaluated to decide upon the need for further refinement. This mesh refinement study is described in detail in the following section. Table 2 lists the regions of refinement, their refinement levels and the effective cell size. It is important that the mesh density does not change too rapidly across the domain as it will impact the quality of the results obtained in simulation. With this said it was decided that each refinement level will have a minimum of three layers in any direction before the adjacent level takes effect.

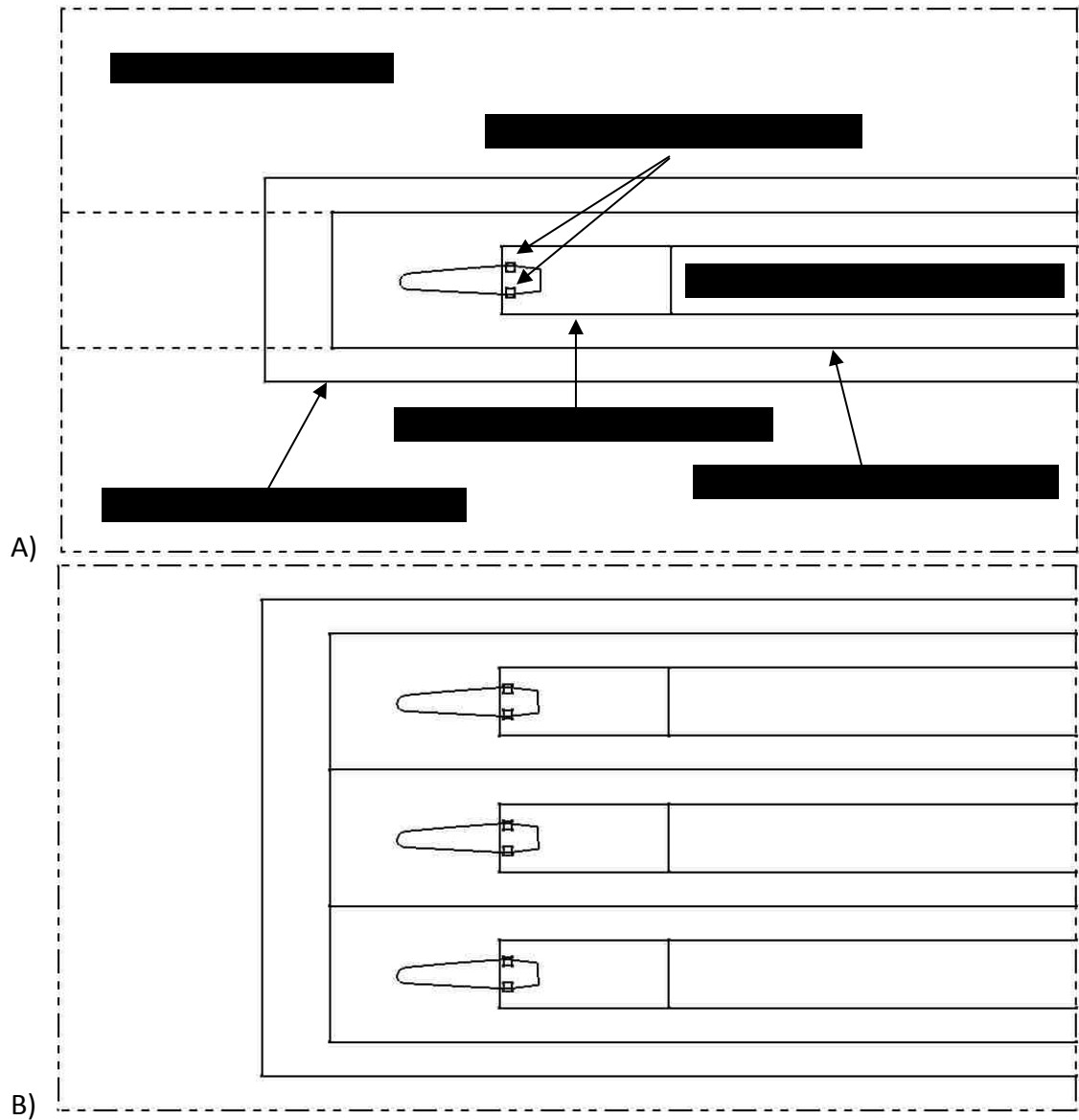


Figure 9: Initial Refinement Regions

A) Refinement regions representative for all single fin simulations. Dashed lines within domain represent the upper and lower boundaries for symmetric and cyclic analyses. B) Refinement regions representative for all three fin array simulations.

Refinement Region	Refinement Level	Effective Cube Length
blockMesh	Level 0	11.000 mm
Outer	Level 3	1.375 mm
Inner	Level 4	0.688 mm
Vortex	Level 5	0.344 mm
Wake	Level 5	0.344 mm
Profile	Level 6	0.172 mm
Step	Level 7	0.086 mm

Table 2: Final Refinement Region Levels

The final mesh resolution will ultimately limit the maximum frequency that can be visually plotted across the domain without aliasing. This can be determined using the Nyquist sampling theory presented in the equations below.

$$f_s > 2f \quad (4)$$

$f_s = \text{Sampling frequency}$

$f = \text{Frequency band measured (5550 Hz)}$

To relate this equation to the mesh resolution the relationship $f = v/\lambda$ can be substituted as follows:

$$\frac{v}{\lambda_s} > 2f \quad \rightarrow \quad 30\,900 > 11\,100$$

$v = \text{Wave propagation velocity (340 m/s in air)}$

$\lambda_s = \text{Largest mesh cell size (0.011 m)}$

Substituting all the giving values into the previous equation reveals that even the largest cell size is capable of plotting the 5550 Hz phenomenon without aliasing. In fact

the largest cells should be capable of plotting frequencies up to 15000 Hz. A similar maximum frequency limit for the simulations is related to the time step chosen. This will be discussed in the time step study section in the following chapter.

Now that the refinement regions and their levels have been defined the second step that the snappyHexMesh utility performs is a castellated mesh. This process removes the profile from the domain by removing the previously defined cells whose major volume lies within of the volume of the geometry and retaining those that do not. Figure 10 is an example of what a section of the mesh looks like after the castellation process for the revised geometry. It is clear that this step is not enough to capture the true shape of the profile indicated by the dashed lines thus a mesh snapping process proceeds.

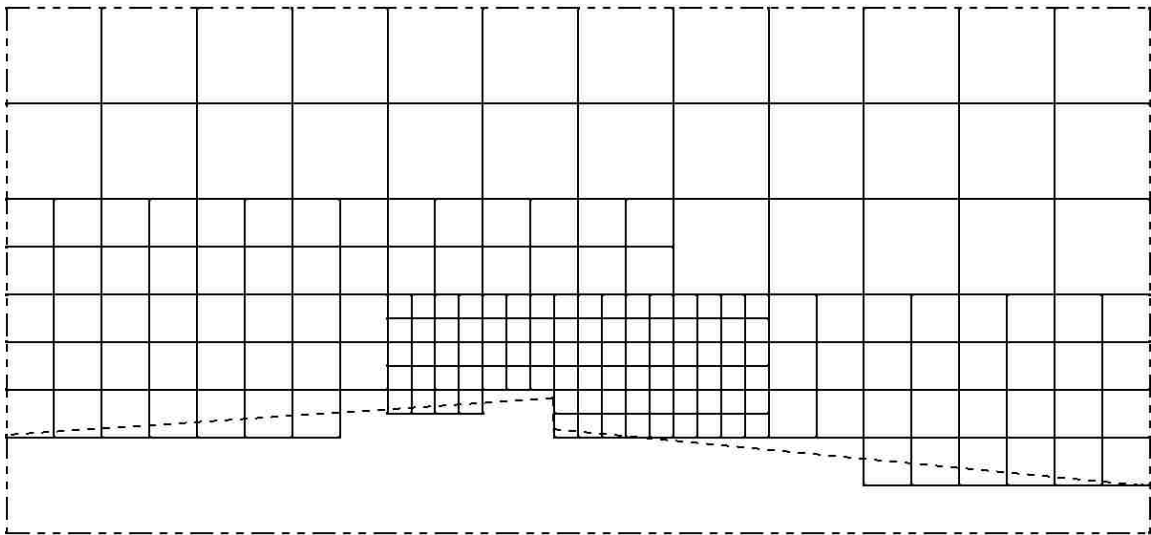


Figure 10: Example Castellated Mesh for Revised Profile

During mesh snapping the vertices of the cells intersected by the geometry are moved to the geometry surface based on their relative distance to the profile and the result from its application on Figure 10 is provided in Figure 11. Controls are available within the snappyHexMeshDict for this process as well but were left relatively at their default values in obtaining adequate results.

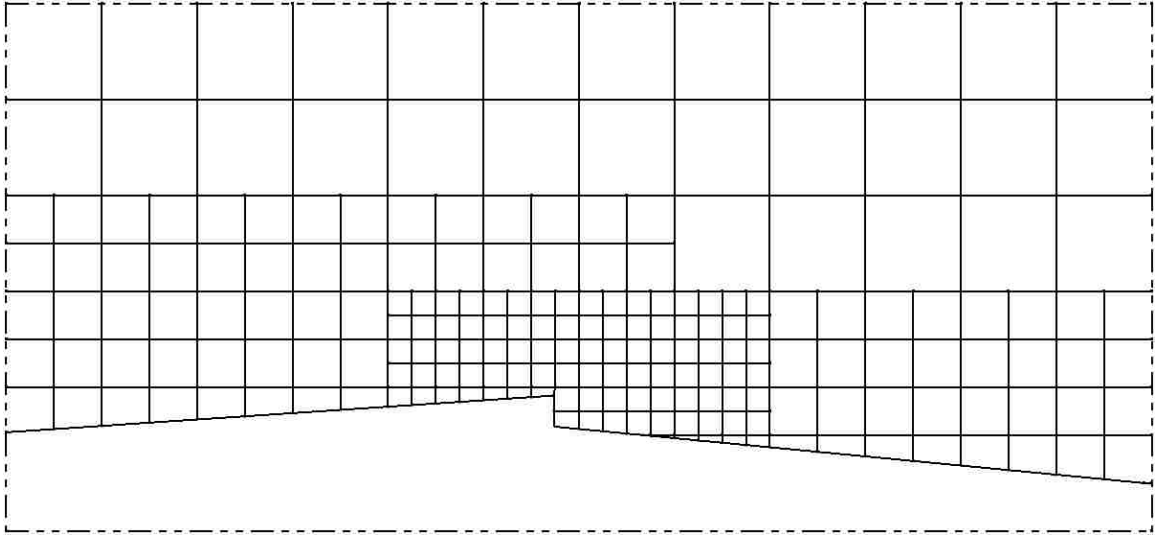


Figure 11: Example Snapped Mesh for Revised Profile

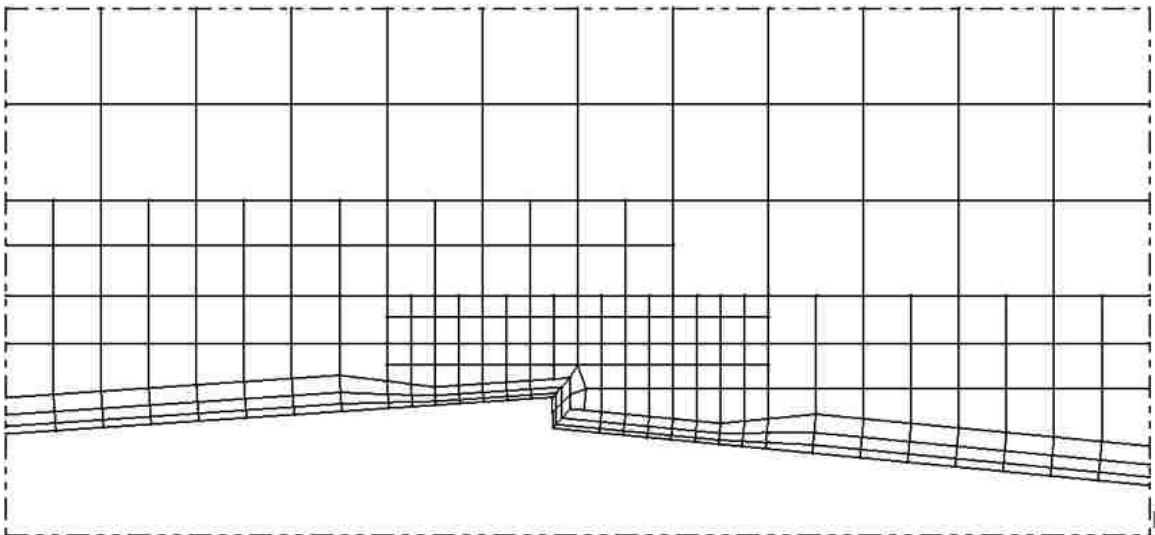


Figure 12: Example Boundary Layer Mesh for Revised Profile

The fourth and final step to follow is the boundary layer process. These cells will be placed along any boundary chosen and its cell thickness, number of layers and expansion ratio defined in the `snappyHexMeshDict` file. For all the simulations performed in this experiment the only boundary that these layers will be applied to is the geometry surface. The number of layers chosen was three and the expansion ratio

was set to 1.5 meaning that each layer is one and a half times larger than the previous moving in a direction away from the surface. The thickness of all the layers in total was selected to be 75% of the adjacent refinement region cell size. Boundary layers help in capturing the highly gradient flow characteristics that occur along the geometry surface. Figure 12 illustrates an example of how the boundary layer meshes are created along the profile of the geometry. During the whole process of building each mesh the quality control parameters listed in Table 7Table 3 and set within the snappyHexMeshDict file are checked at every iteration throughout all phases of construction.

With all the domains, boundary conditions and meshes determined the simulations can now be run. Table 4 summarizes all the cases that will be run for evaluation of the problem at hand. The case number refers to the geometric array in the domain where the case letter refers to the combination of profile and equations to be solved. Before every case was run a mesh refinement and time step study were conducted on Case 1A to determine if the solution obtained was within a reasonable percentage of error. The refined mesh parameters and the adequate time step value chosen would be used across all meshes.

Quality Control Parameter	Description	Value
maxNonOrtho	Maximum non-orthogonally allowed	65
maxBoundarySkewness	Max boundary face skewness allowed	20
maxInternalSkewness	Max internal face skewness allowed	4
maxConcave	Max concaveness allowed	80
minFlatness	Ratio of minimum projected area to actual area	0.5
minVol	Minimum pyramid volume	1e-15
minTwist	Minimum face twist	0.05
minDeterminant	Minimum normalised cell determinant	0.001
minFaceWeight	Minimum face weight	0.05
minVolRatio	Minimum volume ratio	0.01
minTriangleTwist	Minimum Triangular Twist	-1
nSmoothScale	Number of error distribution iterations	4
errorReduction	Amount to scale back displacement at error points	0.75

Table 3: Mesh Quality Control Parameters

ControlDict

This dictionary file controls the run of each simulation case. Within it defines start time, end time and the time step in which to advance the calculation of the mesh domain. The solutions produced at each time step can be written at any desired interval creating a separate data file for each time step written. The time step can be fixed or automatically adjusted based on the Courant number calculations performed before

proceeding to the next cycle of calculations. The latter option will be used for the compressible cases that deal with the propagation of the pressure fluctuations. Since the number of time steps will determine the simulation end condition there are no need to define convergence criteria. If convergence criteria are use the simulation may stop short of the determined simulation time required for an accurate FFT where its value will be introduced later in the simulation run time study section. In this dictionary there are also controls for the format and precision of the written data. In addition to the time controls an important section of the controlDict is the option for what are called functions. There are many functions to choose from, however, for the research presented only those of importance will be described.

Case Name	Array	Profile	Flow Equations
Case 1A	Single	Original	Incompressible
Case 2A	Symmetry		
Case 3A	Cyclic		
Case 4A	Three		
Case 1B	Single	Revised	Incompressible
Case 2B	Symmetry		
Case 3B	Cyclic		
Case 4B	Three		
Case 1C	Single	Original	Compressible
Case 4C	Three		
Case 1D	Single	Revised	Compressible
Case 4D	Three		

Table 4: List of Simulations

The first to add is the courant function which was set to display and print to file the calculated minimum, maximum and average courant number for each time step. Every function has its own file in which it saves the calculations for each time step as a new line item. This function provides a visual check for the compressible cases to ensure that the revised time step between calculations results in a courant number lower than the chosen value of 1. For incompressible cases it offers a means to estimate the quality of the solution while using a fixed time step.

The second added was the lift and drag function which was set to print to file. The function requires the lift and drag direction, frontal area, chord length, reference point and wheel base. The wheel base variable is used when computing flow over a two-axle vehicle to obtain the down force at each axle and will be discarded from the results obtained since we are not interested in this output. The lift direction is simply defined as a normalized vector in the positive vertical direction and similarly for the drag direction which is parallel to the direction of flow. The chord length was calculated from the use of CAD software to be 0.0228 m with a reference area of 501.6 mm² using the domain width defined previously. The position of the reference point is arbitrary and impact on the intensity of lift and drag fluctuation is not important since the amplitude of the resulting FFT performed on this data has no significance. The spectral density of the collected lift and drag data only correlates to the frequency of the pressure fluctuations and was only added to the controlDict functions to verify the placement of the pressure probes.

The final function to be discussed is the addition of probes into the flow domain. Probes are single point coordinates within a domain in addition to the points that create the fluid mesh. These probes can be set to report any variable calculated at each time step. A single file is created for all the probes listed in which each column holds the data for each probe defined and rows are populated by the calculations for each time step. The positions of the probes defined were chosen to be on a plane parallel to the flow at mid distance between the two sides of the domain. This would reduce the impact of the boundary and its conditions on the probe measurements.

The probes were oriented in two different patterns depending on the orientation of the geometry. The fins were chosen to be a distance of approximately 2 chord lengths from the geometry to avoid the capture of pressure fluctuations generated by eddy turbulence near its surface. Using the mid-point of the chord length the probes were arranged in a circular fashion around the profile for the simulations involving a single fin. For all other array cases oval shape is used with a major axis 2 chord lengths from the center and a minor axis equal to that of the upper and lower boundaries found in the symmetrical and cyclic simulations. Figure 13 shows these probe locations.

Solving the Simulations

All simulations conducted in this research began with initializing the meshes with a RAS solution in efforts to reduce the number of computations performed using the DES solver. RAS requires fewer resources than DES and its use can help minimize the number of time steps needed to move from transient to quasi-steady state conditions during DES computation. The RAS was run for 5000 time steps of 1 second to ensure the solution over the entire mesh has reached a quasi-steady state. The size of the time step isn't of much importance during RAS since the solution is only used as an initial value set, however, the time step chosen can still impact convergence time. To further reduce overall computation time the mesh used for RAS were nearly the same as those for DES but of a coarser resolution. The number of nodes and their locations do not have to match between both RAS and DES meshes, the results from the prior can easily be interpolated onto the latter. The setting used for RAS are listed in Table 5.

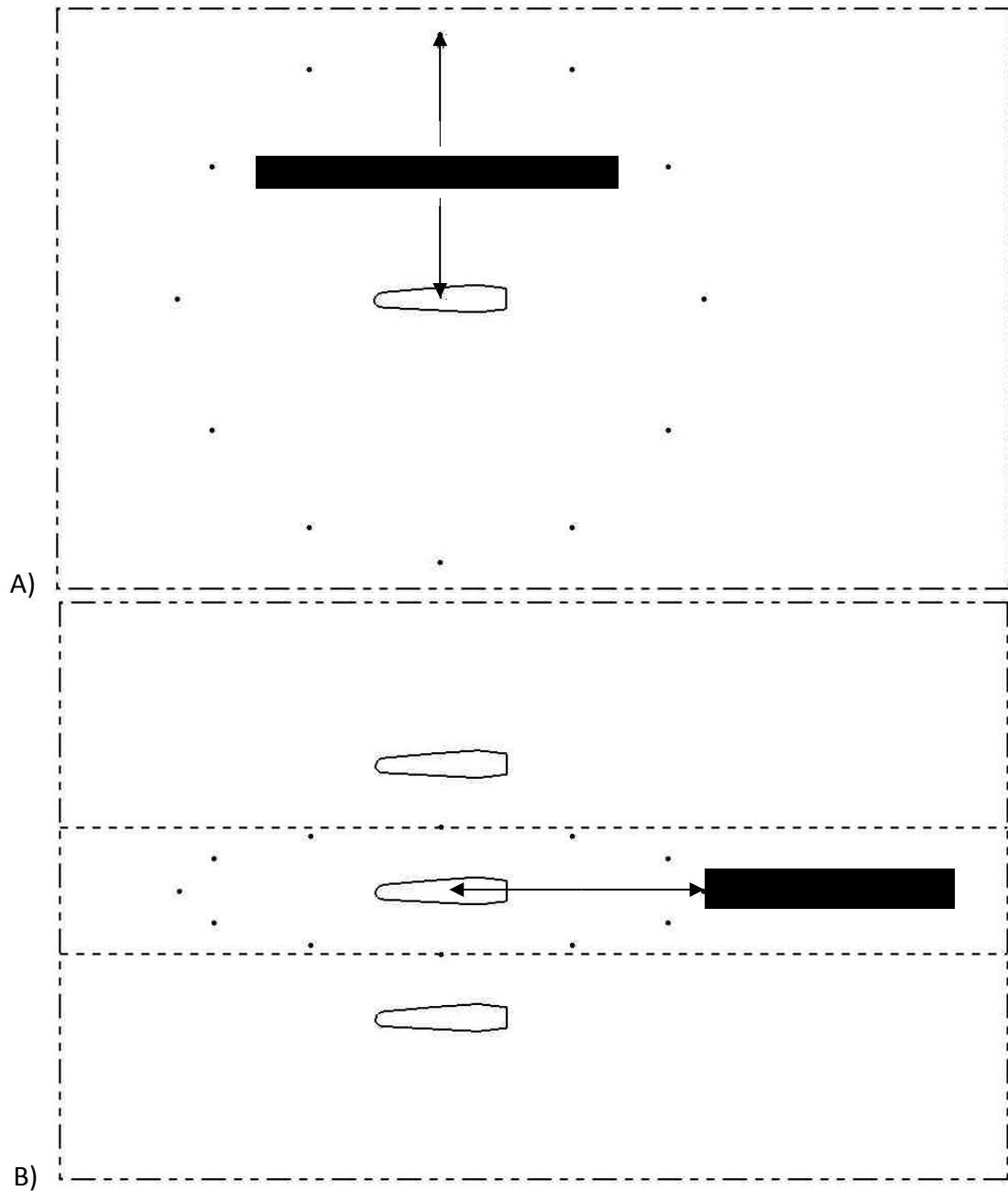


Figure 13: Probe Locations

A) Probe locations for all single fin simulations. B) Probe locations representative for all single and three fin array simulations. Dashed lines within domain represent the upper and lower boundaries for symmetric and cyclic analyses.

Parameter	Setting		Definition
Numerical Schemes	Time ($\partial/\partial t$)	steadyState	No time derivatives solved
	Gradient	Gauss	Second order Gaussian interpolation
	Divergence	linearUpwind	First/Second order bounded
	Interpolation	linear	Linear interpolation
	Laplacian	Limited 0.333	Blended: 0.333 Unbounded second order conservative 0.666 Bounded first order non-conservative
Surface Normal Gradient	Limited 0.333	Limited non-orthogonal correction	
Turbulence Model	Spalart-Allmaras		
Wall Function	nutkWallFunction		

Table 5: RAS Solver Settings

It was decided to use the Spalart-Allmaras turbulence model since its performance was refined for use with airfoils, a geometry that is closely resembled by the profiles used in this research. The frequency of positive comments regarding the performance of the Spalart-Allmaras model within previous works reviewed has also influenced its choice of use. Once the RAS results are interpolated on their respective DES meshes the incompressible and compressible solvers are run to obtain the final solutions that will be compared in the following chapter. The settings used for these cases are provided in Table 6. The schemes and models excluded in this table have the same settings used previously in RAS.

Parameter	Setting		Definition
Numerical Schemes	Time ($\partial/\partial t$)	backward	Second order implicit
Wall Model	Incompressible	nuSgsWallFunction	
	Compressible	muSgsWallFunction	

Table 6: DES Solver Settings

Simulation Runtime Study

The simulation runtime study was a simple evaluation to determine the required amount of time the simulation must run to capture enough information about the flow characteristics to obtain a spectral density graph that adequately depicts the frequencies of pressure oscillation. This was done by running Case 1A for a simulation time of 1 second and performing a series of FFT's on various sizes of the captured data. Evaluation was done through comparison of the resulting spectral density graphs and the outcome of this study is described in the following chapter.

Time Step Study

A second study was performed to determine the time step required to accurately capture the characteristics of flow and again yield an adequate spectral density graph of the pressure fluctuation frequencies. An important variable to consider while selecting a time step is the relationship between this time step to that of the smallest cell length in the direction of flow. This variable is called the Courant number and is expressed as

$$C_o = U \cdot \frac{dt}{dx}$$

Where dt is the time step, dx is the length of the smallest cell in the direction of flow and U is the speed of flow, usually the speed of sound. It is ideal that a Courant value of 1 or less is achieved throughout the entire mesh to ensure that an accurate solution of

the flow is obtained. A Courant value of 1 simply states that at the given velocity a particle or eddy will travel one cell length for a chosen time step. This method was applied to the compressible simulation cases to obtain accurate results of pressure wave propagation for evaluation of the effects of adjacent flow regimes. As described in the controlDict section the time step is adjusted as the solution progresses to ensure this value remains below the chosen value of 1.

For the incompressible cases pressure propagation is instantaneous across the entire fluid domain and the Courant number for the speed of sound is no longer accurate. To determine an initial value for the time step the speed of sound in the Courant number equation was substituted for the average speed of flow. Rearranging this equation and selecting a cell length of 1 mm as an overall average of the domain a time step of 5e-5 seconds was yielded. The study was performed on Case 1A by halving this value and comparing the results of the spectral density graphs. The findings of this study can be found in the forthcoming chapter.

A related item for choosing the time step is the time scales, otherwise known as turnover time, of the eddies being resolved. The scales of eddies range from the largest having the most kinetic energy to the smallest at which this kinetic energy is dissipated. From the dimensions of the geometry and flow velocity the largest eddy sizes can be estimated. The dimension in this research limiting the size of the eddies formulated is the thickness of the profile. This value is referred to as the integral length scale and is assigned the value of 0.005 m. Using this value in conjunction with the flow velocity the integral time scale can be estimated.

$$t_L = L/U = 1.79 e^{-4} s$$

$$t_L = \textit{Integral time scale}$$

$$L = \textit{Integral length scale (0.005 m)}$$

$$U = \textit{Mean flow velocity (28 m/s)}$$

The smallest length scales can be estimated using Kolmogorov's relationship between viscosity and the rate of energy dissipation and are thus called the Kolmogorov length scales. With the dissipation rate being approximated as the rate at which kinetic energy is produced the following relationship can be stated:

$$\eta = \left(\frac{\nu^3}{\epsilon}\right)^{\frac{1}{4}} = \left(\frac{\nu^3 L}{U^3}\right)^{\frac{1}{4}} = 5.44 e^{-6} m$$

$\nu = \text{Viscosity } (15.68 e^{-6} m^2/s)$
 $\epsilon = \text{Energy dissipation rate } (U^2/t_L)$

Similarly, the Kolmogorov time scale can be approximated using viscosity and rate of energy dissipation:

$$t_\eta = \left(\frac{\nu}{\epsilon}\right)^{\frac{1}{2}} = \left(\frac{\nu L}{U^3}\right)^{\frac{1}{2}} = 1.90 e^{-6} s$$

Comparing the integral time scale of the eddies to the time step it can be determined that 1.25e-5 second time step is considerably smaller and is capable of resolving the large eddies present in the wake of the geometry. However, the Kolmogorov time scales are far too small to be resolved directly with this time step and will be approximated with the use of the turbulence model.

Mesh Refinement Study

To determine if the initial refinement levels of the mesh are adequate a mesh refinement study was performed. Increasing the refinement levels of the entire domain is not necessary since the flow mechanics of interest will occur around and downstream of the geometry. Three different areas have been chosen to focus the refinement process and determine if the flow is impacted as resolution of a refinement region is increased. These areas were the vortex region, the step region and the wake region. The step and wake region underwent only a change in resolution where the study of the

vortex region also included an evaluation of its dimensions. The study was performed on Case 1A where each area was altered in turn while leaving the other two in their original state. As it was for the runtime study the results from each mesh refinement simulation were compared through their respective spectral density graphs. The results of the mesh refinement study are provided in the next chapter.

CHAPTER IV

RESULTS

In this chapter the findings from the initial simulation setup studies will be presented as well as key images capturing the mesh structure, flow field, pressure field, and power spectral densities for the 12 cases outlined previously. The flow and pressure field are of the final time step at the end of the 0.275 second simulation time and depicts the characteristics of flow at an instantaneous point in time.

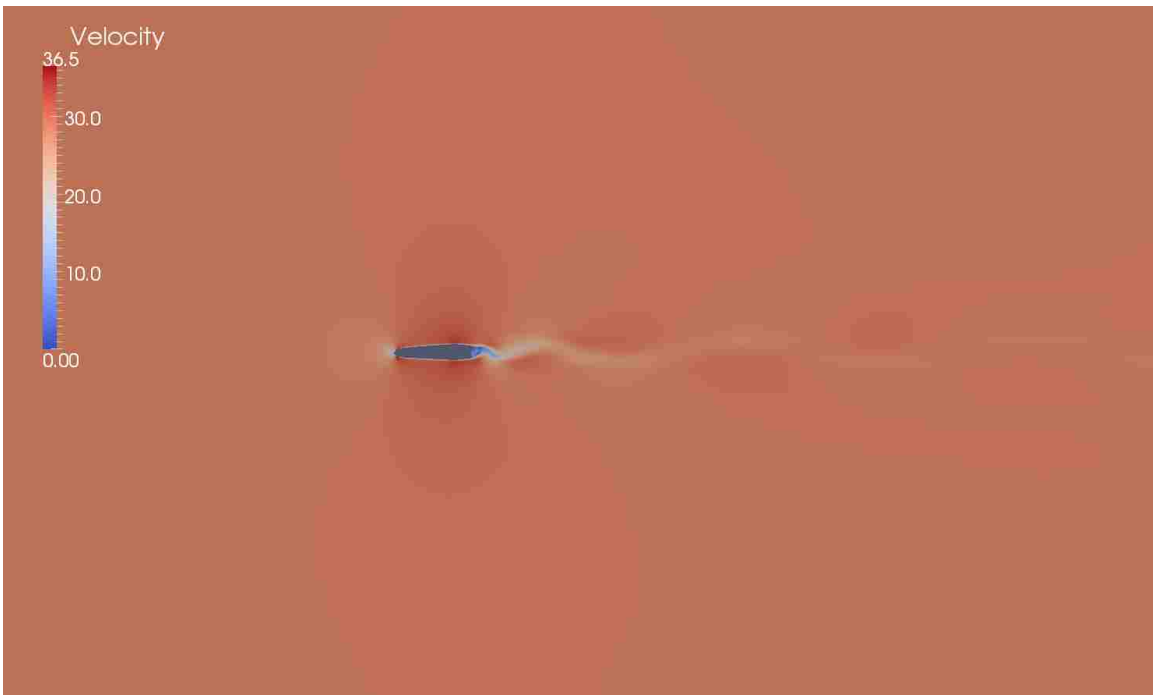


Figure 14: Case 1A RAS Velocity Field

Simulation Runtime Study

One of the first tasks completed in determining the final design for all the cases is the simulation runtime study. As mentioned before, this was conducted on a non-refined mesh with a time step $5e-5$ seconds through DES simulation initialized with the results of a converged RAS calculation. Figure 14 and Figure 15 below show the RAS and DES results for the refined simulations of Case 1A. Although not the same as the output during the studies, the visual results are very similar.

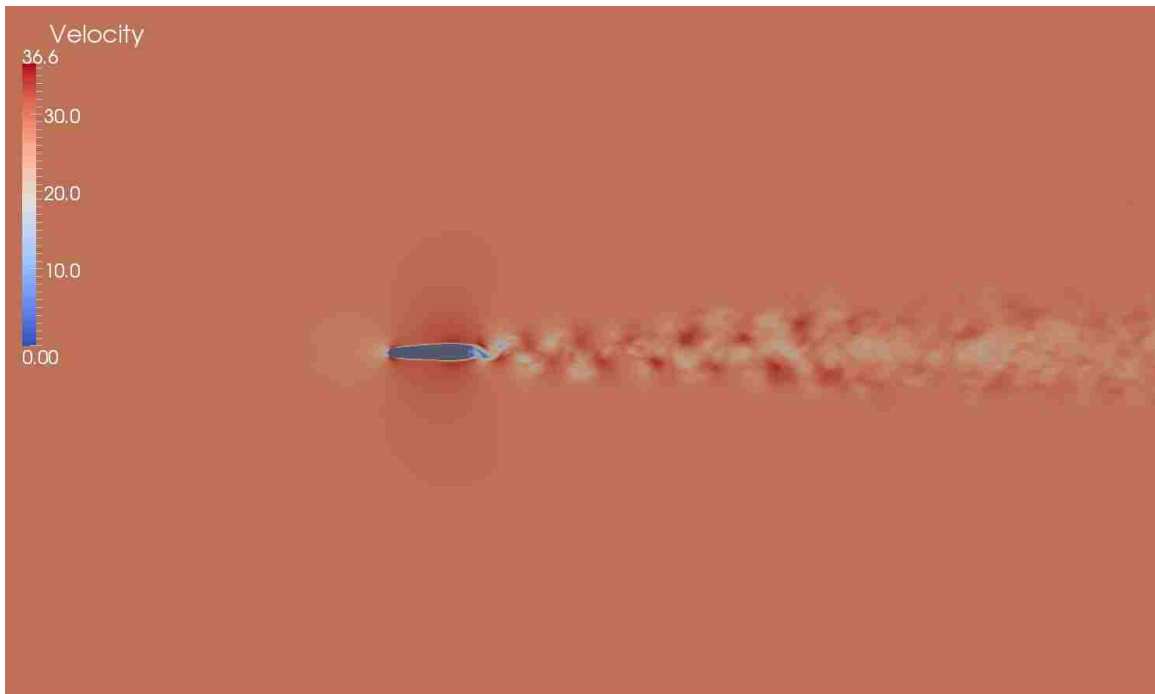


Figure 15: Case 1A DES Velocity Field

The difference between the steady RAS results to those of the DES is clear. The DES captures the undulating behaviour of the shedding vortices. The pressures recorded at each probe location were operated on with an FFT to produce a visual representation plotting the amplitude in dB versus frequency as shown in Figure 16. This figure compares the behaviour captures at each of the 12 positions. A quick examination reveals three basic curves that the probes tend to follow, distinctly that of 0 degree, 180 degrees and the remainder. Because of their close similarity only one probe position was chosen to represent all those that do not lie on the horizontal plane to maintain legible graphs. The pressure results are also symmetrical about the profile as one would predict from the nature of the geometry. The probe at 90 degrees was chosen because of its relatively large amplitude and for its position directly between the upper and mid profiles in the three-fin array. Using the results of this probe each simulation can be benchmarked against each other to record the changes in frequency and intensity as the studies are conducted.

Probe Comparison

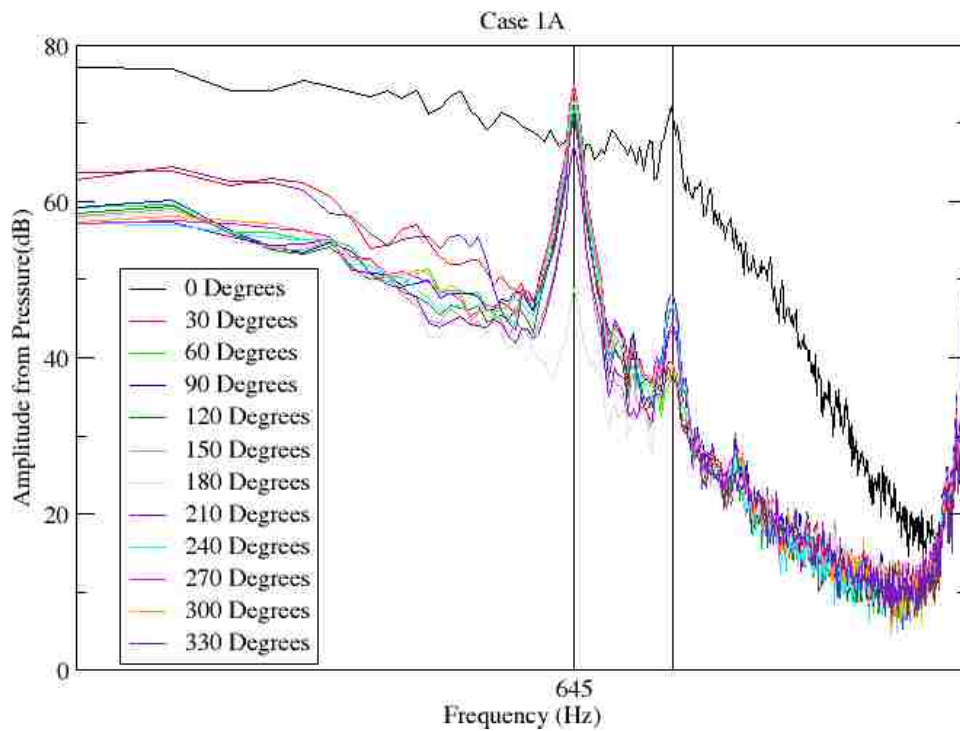


Figure 16: Probe Location Comparison

Sampleset Study

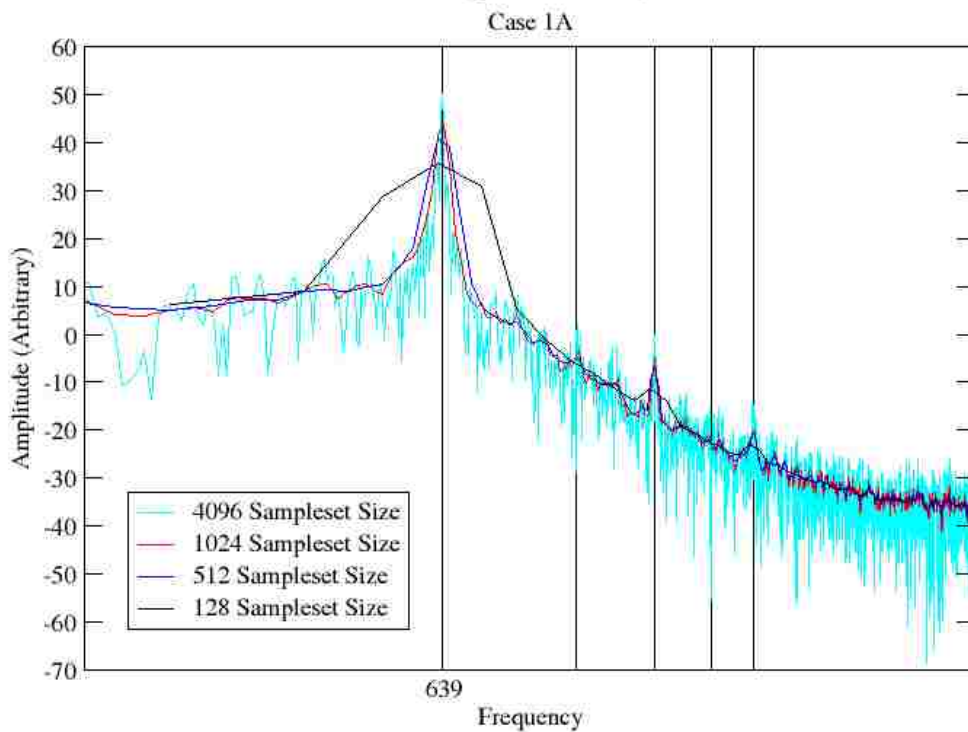


Figure 17: Simulation Runtime Study

Figure 17 shows several FFT analyzes of the same simulation using subsets of different lengths. It is clear that as a larger subset is used the narrower the frequency bands become. Though a subset of 128 measurements still reveals a peak around 645 Hz there is a chance that weaker but equally significant peaks are damped out or absorbed by adjacent ones, not to mention the apparent uncertainty in the accuracy. Another phenomenon is revealed as the subset becomes much larger. The resolution is much higher but there is an introduction of a lot of noise which can obscure the smaller peaks. It was decided that subsets of 1024 values adequately captures the frequency peaks with good resolution while maintaining a low level of noise. While using this subset length and slowly reducing the total number of measurements, thus reducing the total simulation time, it was determined that a minimum of 0.25 seconds was to be acquired before resolution and accuracy began to deteriorate.

Time Step Study

Now having the minimum simulation time to maintain a constant resolution for comparing results the time step can be varied and compared to determine the optimum step in achieving good accuracy but approaching the run time target in the least number of steps. Figure 18 shows four curves of different time steps decreasing from $5e-5$ to $6.25e-6$ seconds. The position of the peak exponentially slows as it transverses from right to left as the time step increases approaching a value of approximately 1320 Hz. The purpose is to choose the step that will closely achieve this value but not demand a large amount of computational resources. The peak for the time step of $1.25e-5$ seconds has an error of approximately 5% compared to that of $6.25e-6$ seconds and of 7% to that of the estimate value being approached. It was deemed that a $1.25e-5$ second time step would be accurate enough to determine if the procedure to follow would capture the differences between the original and revised flow simulations.

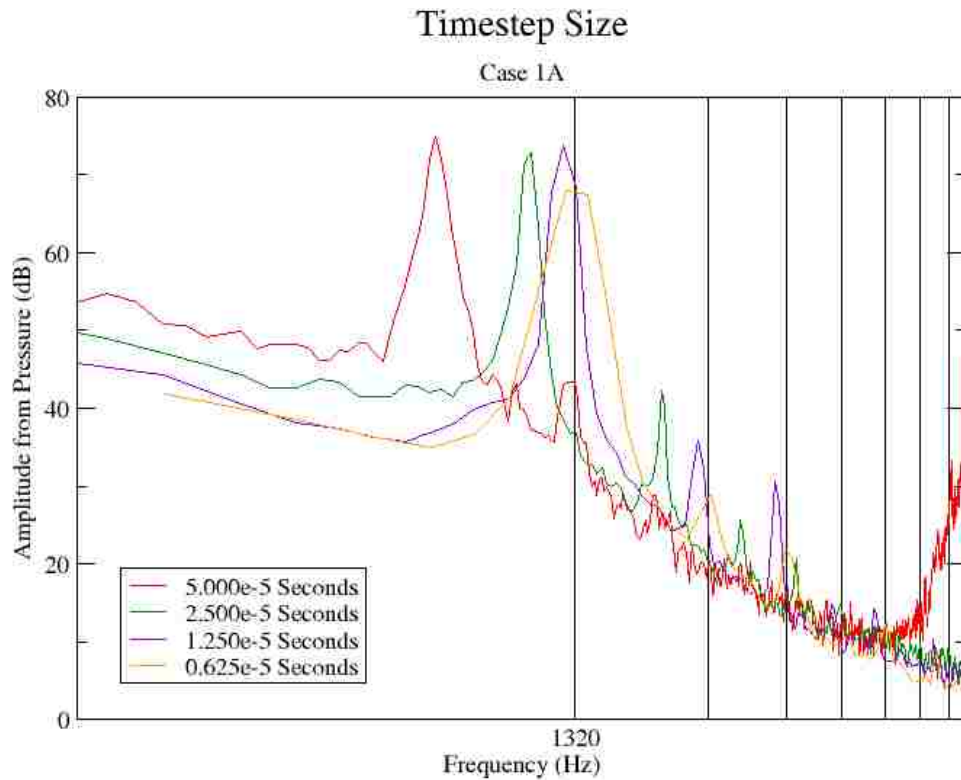


Figure 18: Time Step Study

Similarly to mesh resolution the simulations conducted are limited to a maximum measurable frequency before aliasing occurs. Again, this maximum frequency is half of the sampling frequency selected as outline in equation 4. Before moving forward with the 1.25e-5 second time step a quick evaluation of the maximum frequency measurable was made. The time step is easily related to frequency by the relationship $f_s = 1/t_s$ yielding a value of 80 000 Hz. From the Nyquist sampling theory the maximum measurable frequency that can be accurately captured is 40 000 Hz, more than 7 times the 5550 Hz frequency of interest.

Mesh Refinement Study

Using the time step and simulation runtime now determined the mesh refinement was conducted. Determining how to approach the local mesh refinement of several regions within the domain was not a trivial task. The process was one of trial

and error, manually refining regions both independently and in groups to find the peak value that lies closest to the predicted frequency of 1320 Hz. After many attempts and slowing improvements to the presumed accuracy of the output the mesh construction and resolution was decided on as presented previously in Table 2. The following figures show several images of the mesh output from the OpenFOAM snappyHexMesh utility following this study. Figure 19 captures the full length of the fluid domain to show the extent and resolution of the wake region refinement and resembles the meshes used for initializing all single profile simulations.

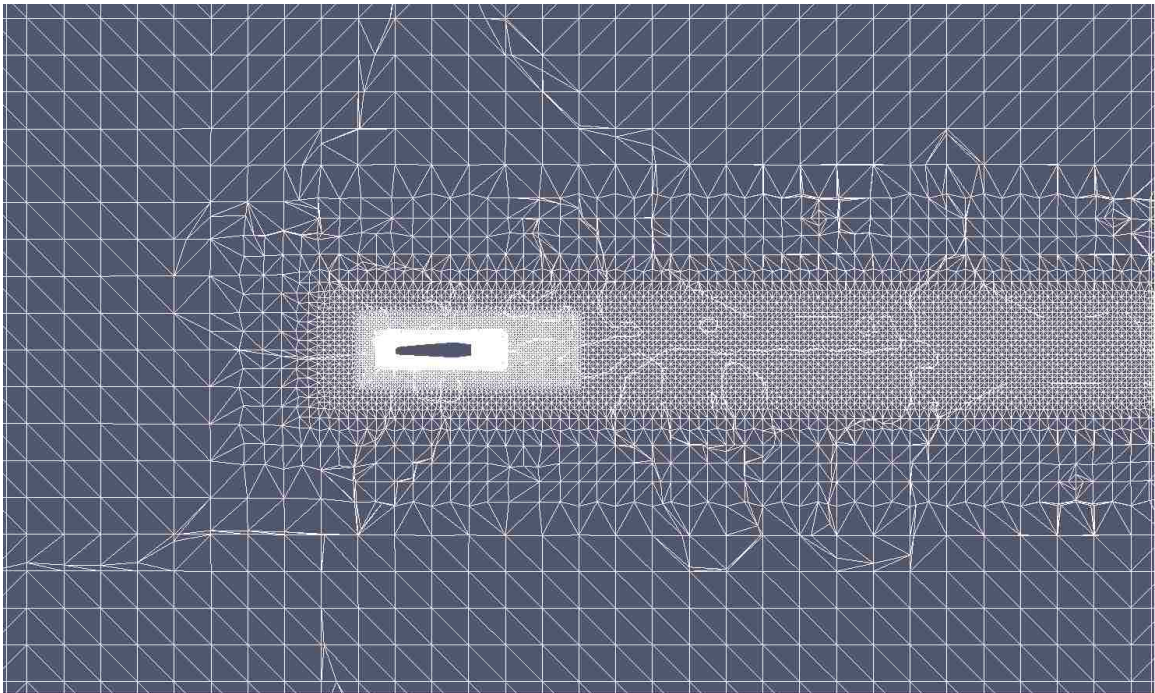


Figure 19: Case 1A RAS Mesh

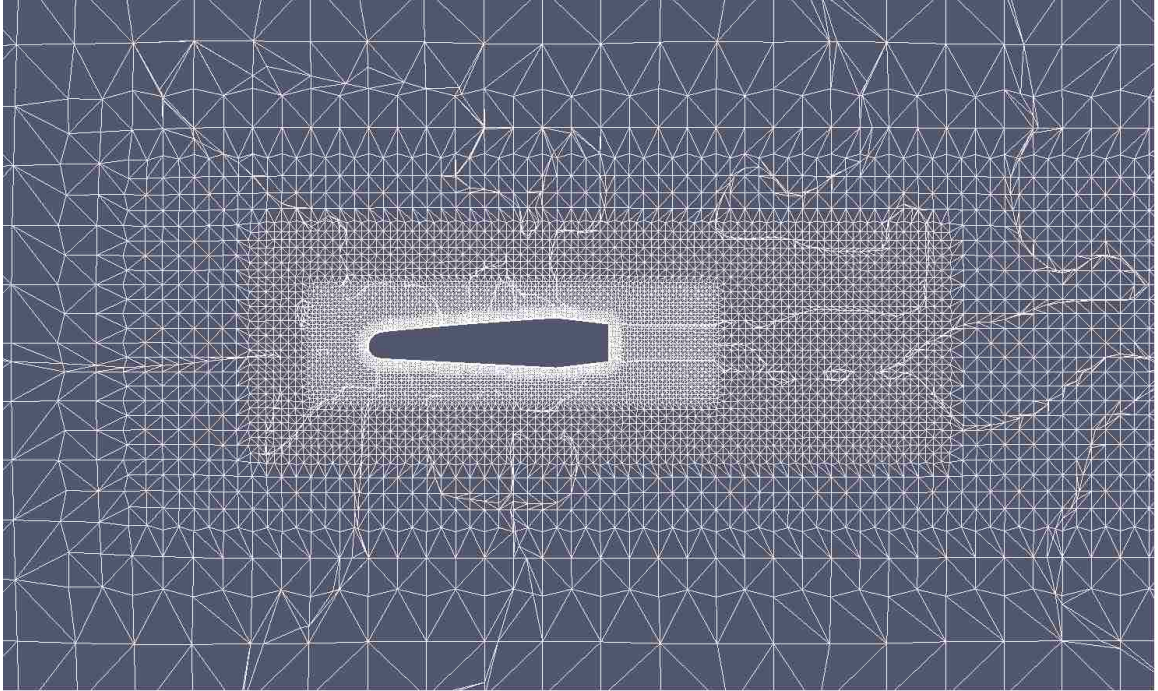


Figure 20: Case 1A RAS Mesh Enlarged

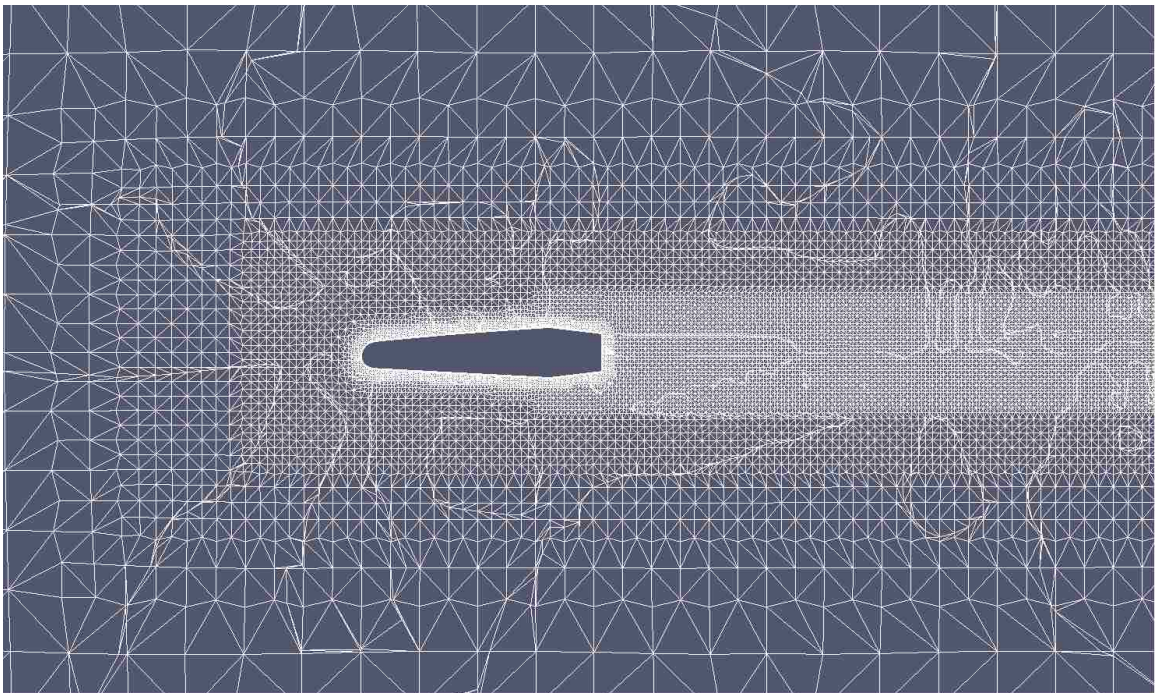


Figure 21: Case 1A DES Mesh Enlarged

The difference between the RAS and DES mesh can be seen from Figure 20 and Figure 21. The RAS is intended only for initializing the DES and thus contains a slightly coarser mesh and smaller refinement regions which results in far fewer cells to compute the flow over. From these first few mesh images the process of decomposing a hexahedral mesh into tetrahedral and pyramid is visually evident. The curvature seen in some regions of the mesh occurs during snapping where nodes created during the castellation phase that lie near the geometry are aligned to its surface. Smoothing and wrapping operations within this step are controlled through mesh quality checks defined in the `snappyHexMeshDict` to help maintain the characteristics of the geometry. The adjustments made to optimize the quality of the cells will often cause them to conform slightly to the contour of the geometry. The strange curves and patterns also visible in these images are a result of the cutting plane used for flow visualization. The cells no longer lie in a planer fashion once the mesh has been optimized around the geometry thus the plane cuts through cells at different depths across the domain.

The following Figure 22 and Figure 23 illustrate the additional refinement region in the presence of the added step to better follow the geometry. This is the only difference over the domain existing between the original and revised profiles. Figure 24 depicts the mesh structure for the cyclic and symmetry DES simulations for both the original and revised profiles. As described in an earlier chapter the only difference between the two types of simulations is the definition of the upper and lower boundaries. The mesh for the array of three profiles is seen in Figure 25. The boundary regions around the profile and in the region of the step are equivalent to those of Figure 22 and Figure 23.

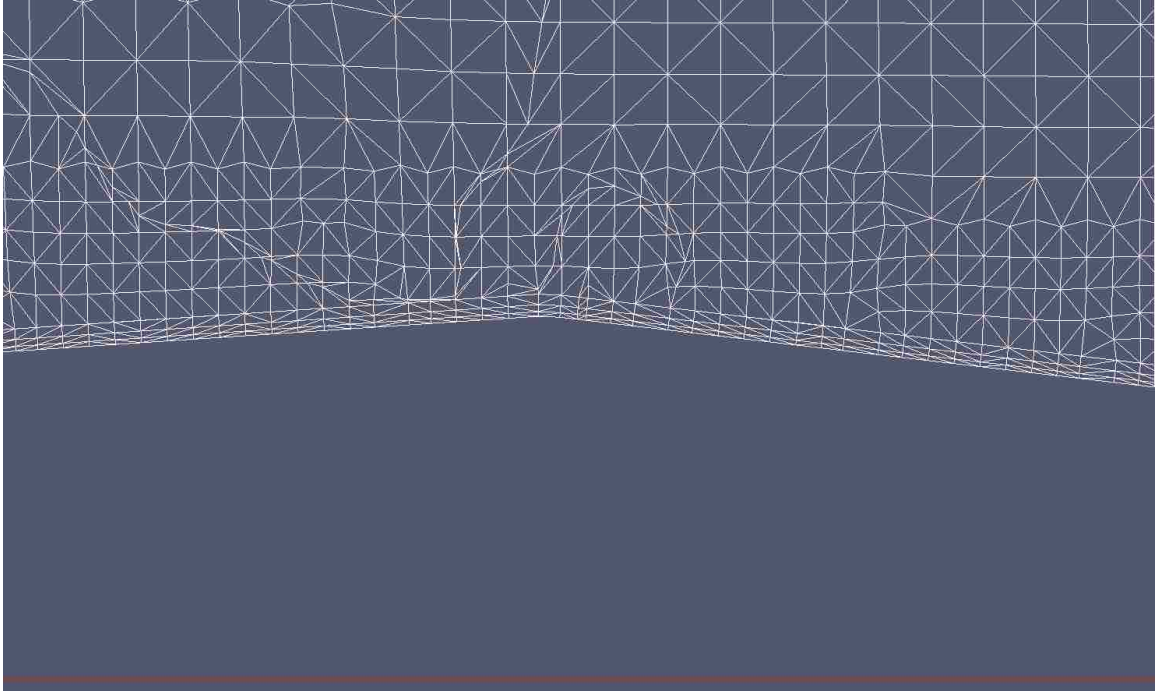


Figure 22: Case 1A DES Mesh Step Region

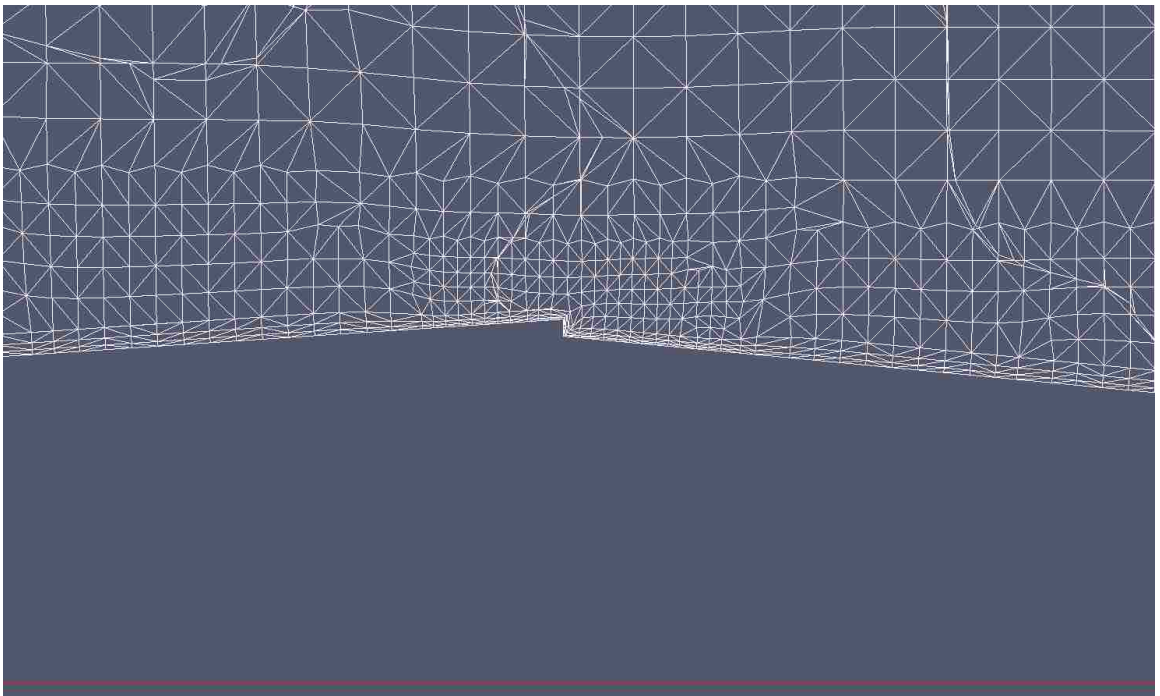


Figure 23: Case 1B DES Mesh Step Region

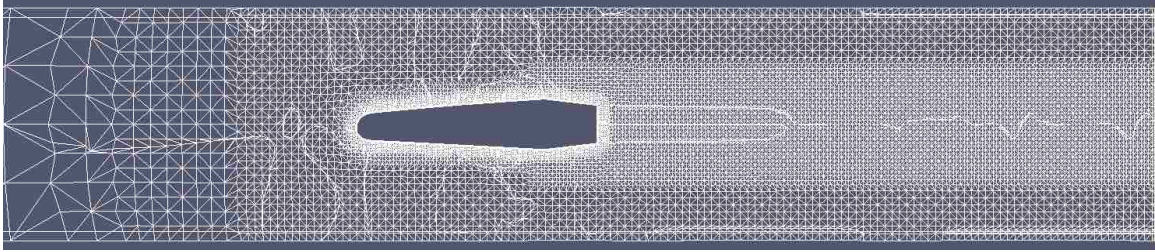


Figure 24: Case 2A and Case 3A DES Meshes Enlarged

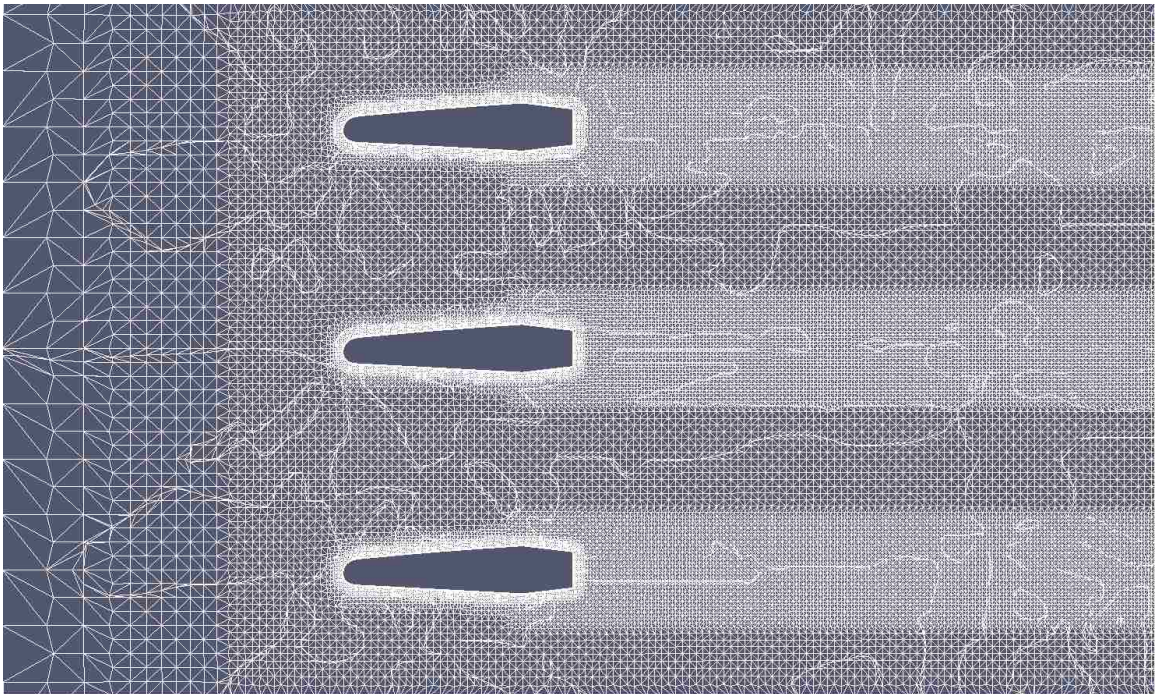


Figure 25: Case 4A DES Mesh Enlarged

Computational Time

With the mesh resolutions, time step and simulation runtimes determined the twelve cases were run and Table 7 created to show the computational resources required to solve each simulation. The majority of the cases used 12 CPU's to complete each simulation with the exception of a few when a greater number of CPU's were available at the research facility. For this reason the final column labeled "Computation Time X CPU" was added to provide a clearer comparison between all cases. It would have been ideal to use the same number of CPU's for all cases for comparison since the

use of parallel processing isn't a linear relationship between computational time and number of CPU's used. Due to the time restrictions on completing the research more resources were needed to complete all the cases within the given time frame.

Case Name	Mesh Cells	Mesh Nodes	# of CPU	Computation Time (h)	Computation Time X CPU (h)
Case 1A	2 297 279	1 946 874	12	40.6	487.2
Case 2A	2 175 897	1 907 045	12	47.0	564.0
Case 3A			12	47.6	571.2
Case 4A	6 648 471	5 736 890	12	138.0	1 656.0
Case 1B	2 454 805	2 054 072	12	42.2	506.4
Case 2B	2 333 423	2 014 243	12	49.2	590.4
Case 3B			12	54.6	655.2
Case 4B	7 121 141	6 058 448	12	149.2	1 790.4
Case 1C	2 297 279	1 946 874	12	83.5	1 002.0
Case 4C	6 648 471	5 736 890	24	160.8	3 859.2
Case 1D	2 454 805	2 054 072	16	77.0	1 232.0
Case 4D	7 121 141	6 058 448	24	415.7	9 976.8

Table 7: Mesh Characteristics and Computation Time

From this table it is apparent that the revised profiles will take 5 to 10 percent longer than their respective cases evaluating the original profile. Similarly the compressible cases took over twice as long as the incompressible cases. There is one exception to these patterns, however, between Case 4C and Case 4D. The results presented later in the chapter provide a better foundation in understanding this discrepancy between the compressible cases for an array of three fins.

Simulation Outputs

This section of the chapter presents the velocity and pressure plots of the final time steps of the simulations performed and will begin with incompressible simulations of the original profile. The velocity results for Case 1A have been delivered at the beginning of this chapter and Figure 26 has been provided to better reveal the shedding vortices from the trailing edge of the profile. The related pressure field in Figure 27 clearly highlights the trailing vortices as well as the high pressure regions ahead and behind the profile and low pressure regions above and below.

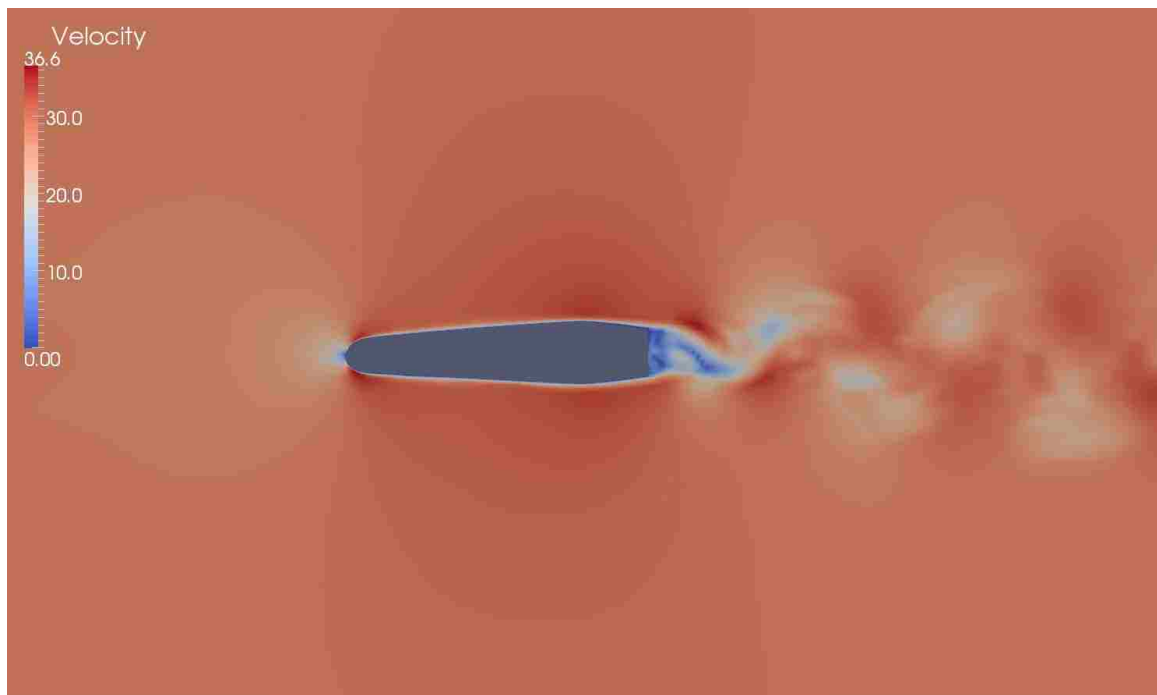


Figure 26: Case 1A DES Velocity Field Enlarged

When performing the array of fins using symmetry boundaries Figure 28 reveals that the peak velocity is 3 m/s faster than it was for the single profile case. The high velocity region above and below the geometry also extends further into the domain than that of Case 1A. Figure 29 also shows a substantial difference from the pressure map of Case 1A with a much higher pressure ahead of the profile. This is the result of the symmetric conditions applied at the upper and lower boundaries which act like a channel. Fluid

cannot flow through the boundaries from the high pressure region to one of lower pressure thus the flow around the profile is highly restricted. The cyclic evaluations of Case 3A produce graphical results very similar to those of symmetry and will not be presented. Immediately it can be determined that use of these boundary conditions are not adequate for representing a geometrical array of fins.

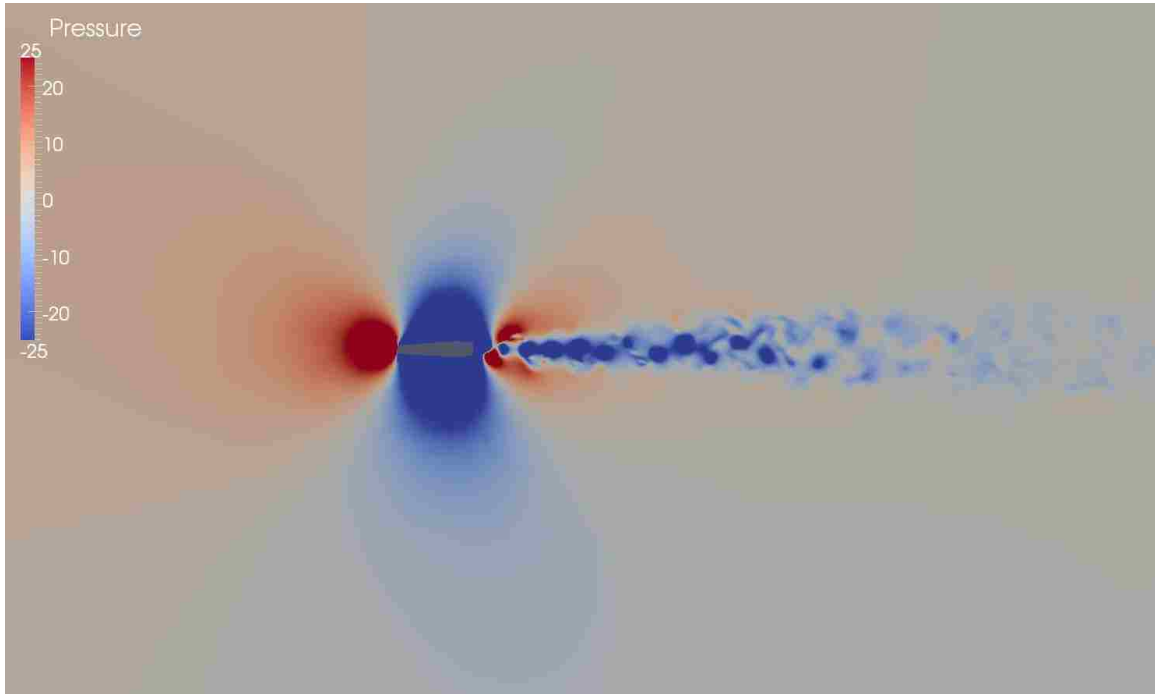


Figure 27: Case 1A DES Pressure Field

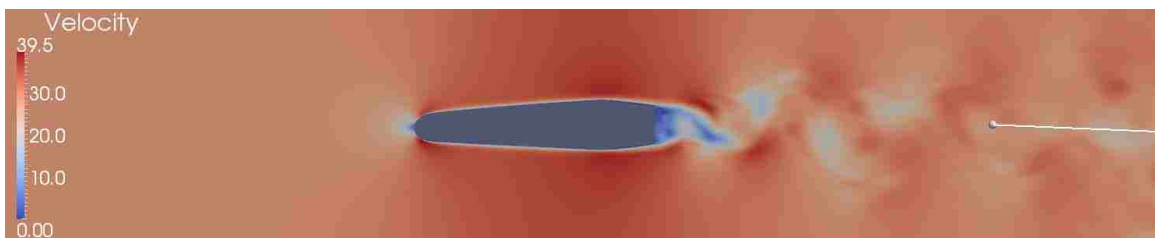


Figure 28: Case 2A DES Velocity Field Enlarged

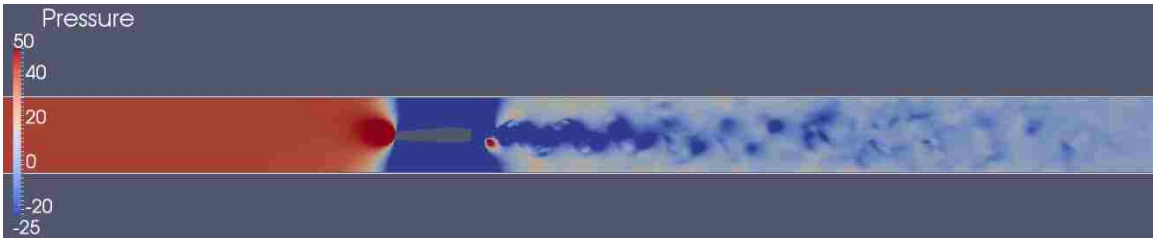


Figure 29: Case 2A DES Pressure Field

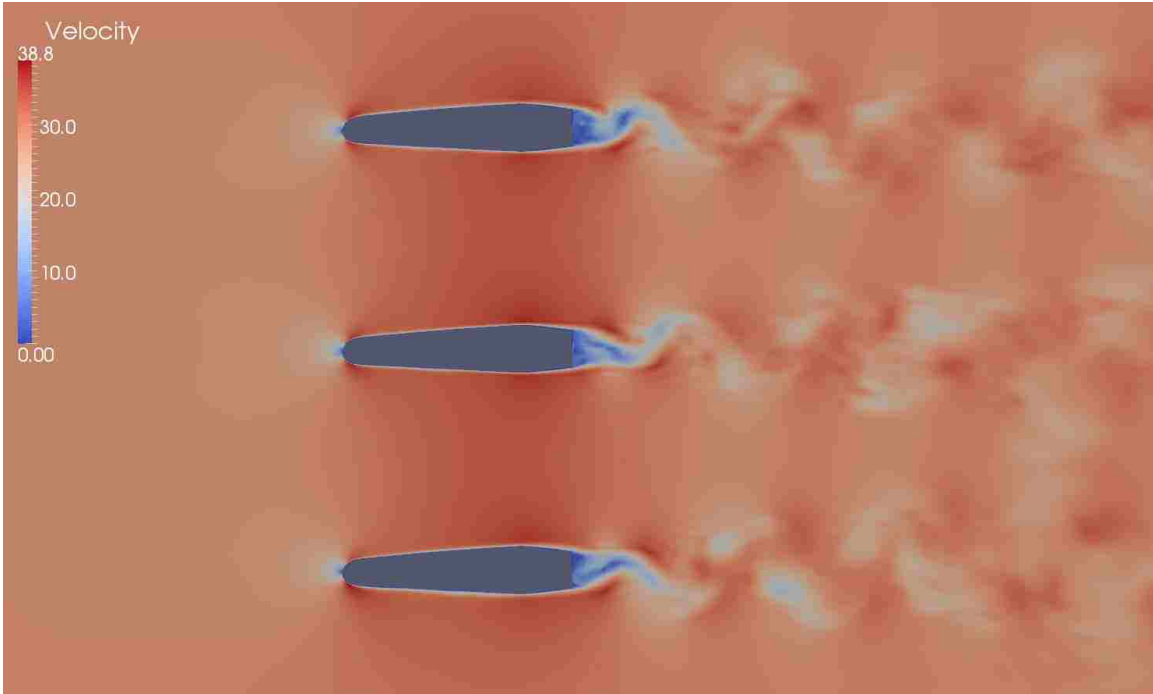


Figure 30: Case 4A DES Velocity Field Enlarged

Moving toward the physical profile array the velocity field of Figure 30 looks to resemble something between the single and the boundary array cases with a velocity slightly biased to that of the symmetric and cyclic cases within 1 m/s. The fluctuating behaviour of the wake does not seem to form a pure cyclic or pure symmetric condition but something in between. Perhaps for this reason the physical array of fins will result in a more realistic and accurate representation of the phenomenon to be captured. Figure 31 also seems to show something of a compromise between the single and boundary arrays with its presentation of the pressure field.

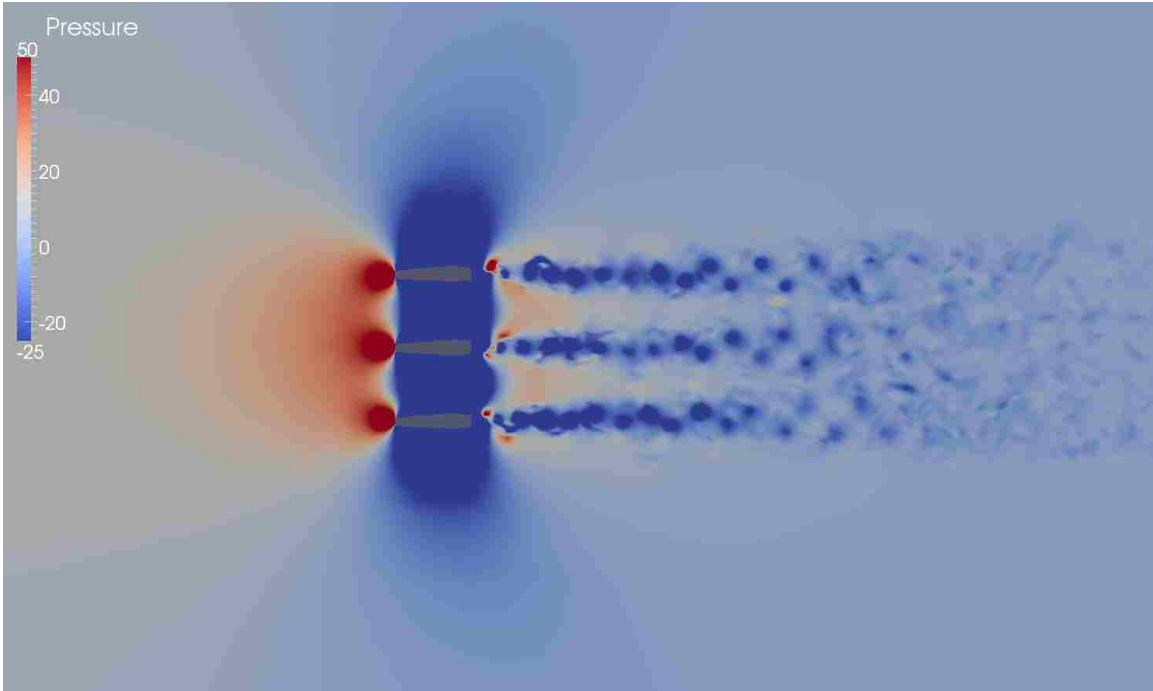


Figure 31: Case 4A DES Pressure Field

The cases for all incompressible simulations against the revised profile with the step geometry all return visual results that are visually the same as those of the original profile with equivalent velocity and pressure scales. For this reason the incompressible images of the original profile will be supplemented for any reference to the visual results for the incompressible cases of the revised geometry. With the incompressible simulations showing no visual differences between the two geometries being evaluated it is becoming apparent that the phenomenon related to the presence of the step cannot be determined with these solvers. The measurements recorded by the pressure probes at each time step could possibly reveal some minute details setting the results of Cases 1X apart from Cases 2X. Before moving into the FFT analysis of these cases to generate SPD charts the compressible cases will first be discussed.

Starting again with the single profile arrangement of the original geometry Figure 32 presents the velocity field results for the compressible DES simulation. Immediately, differences can be seen particularly the peak velocity recorded within domain. The compressible case is producing a peak velocity value of 41.7 m/s, which is

15 percent higher than the 36.6 m/s yielded from the incompressible equivalent. Taking a closer look at the vortices shedding immediately after the trailing edge Figure 33 reveals that the intensity of the calculated vortex trail is visibly higher than that seen in Figure 26. The greatest difference is seen in Figure 34 which introduces the pressure field acquired from the compressible approach. Other than the high pressure region at the leading edge, the low pressure areas above and below the profile and the vortex trail the results is completely different from Case 1A. Though very crude the alternating bands of high and low pressure regions suggest the presence of pressure waves that could very well be perceived as audible noise. The pressure waves appear to radiating from regions very close to the profile in question though a precise location cannot be determined from this image.

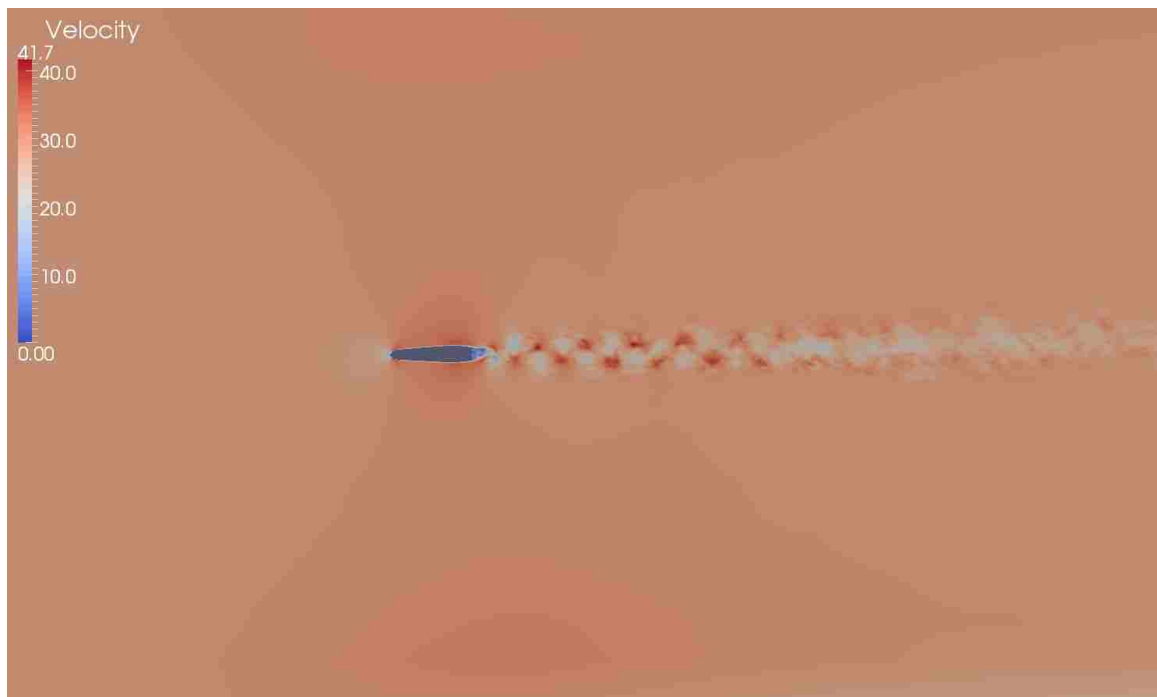


Figure 32: Case 1C Compressible DES Velocity Field

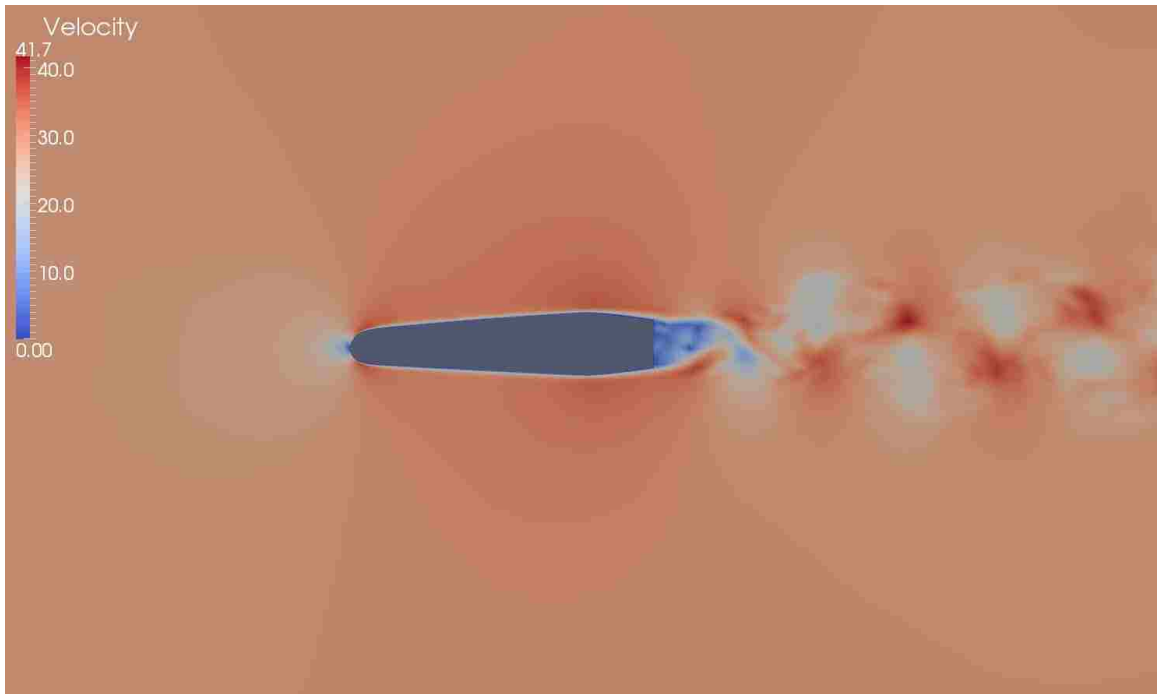


Figure 33: Case 1C Compressible DES Velocity Field Enlarged

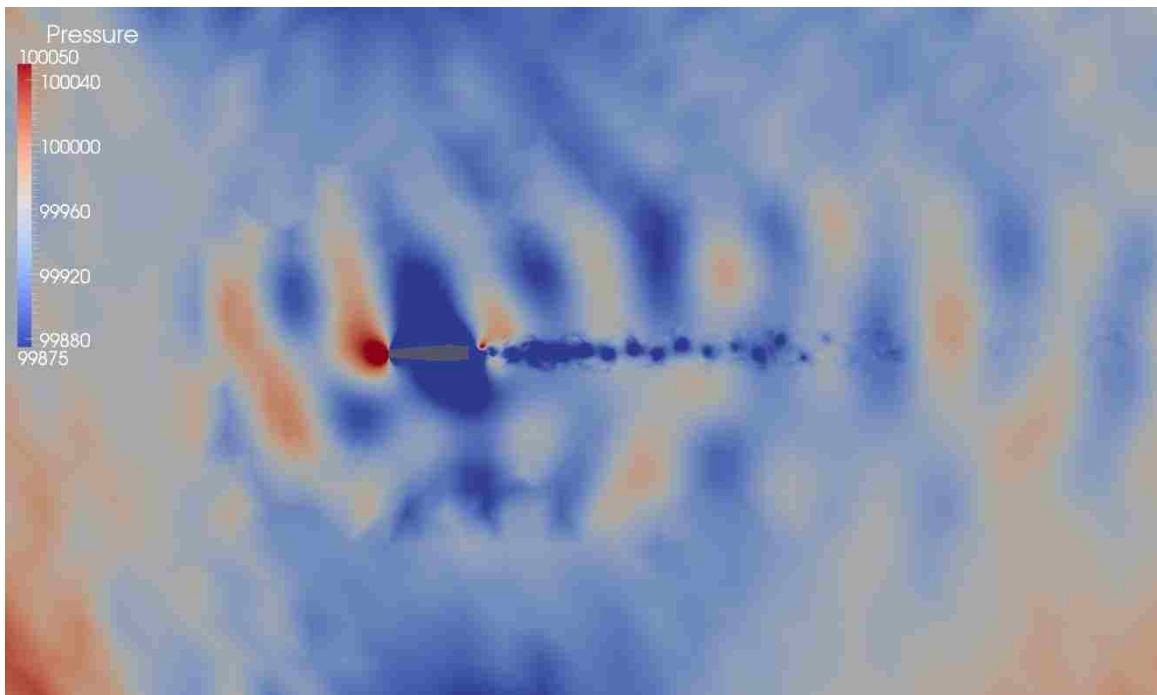


Figure 34: Case 1C Compressible DES Pressure Field

When comparing the compressible result for the stepped profile no visible differences are seen between the velocity field results of both geometries, however, a very different result is clearly evident within the pressure field. Figure 35 shares the same propagating pressure waves present in Case 1C but of a tighter grouping. The closer proximity of the pressure peaks and valleys relate to shorter wavelengths and higher fluctuating frequencies. When related to audible noise this would be perceived as a higher pitch noise but as it was for the original profile the source cannot be determined visually. Further evaluation of the pressure probes may reveal some insight as to where the noise source, or sources, may lie and are provided in the following chapter.

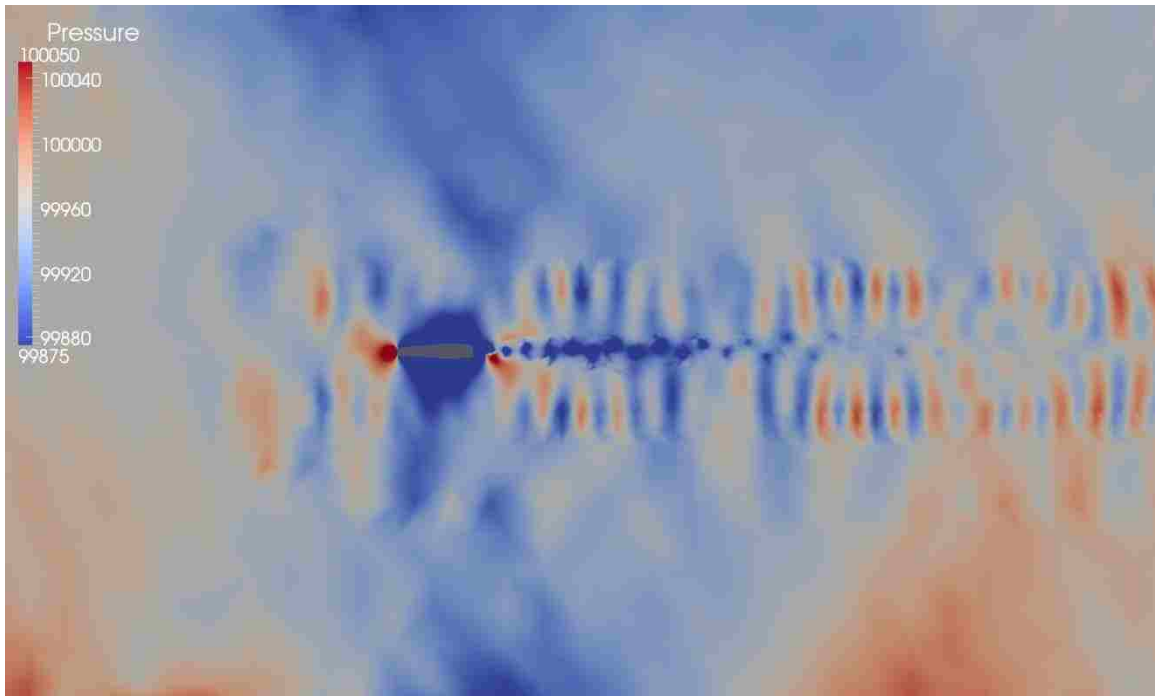


Figure 35: Case 1D Compressible DES Pressure Field

The resulting velocity field in Figure 36 resembles that of the incompressible equivalent Case 4A and as it were for the single profile scenario the peak velocities are higher across the mesh. Looking only in the region between the fins a similar phenomenon of the velocities being approximately 15% higher than the incompressible

results is present. An interesting phenomenon that is apparent in this image is the high velocity turbulent flow at the outlet of the mesh. This case has been run several times to yield a condition similar to this at the end of each simulation and is investigated in the discussion of this thesis.

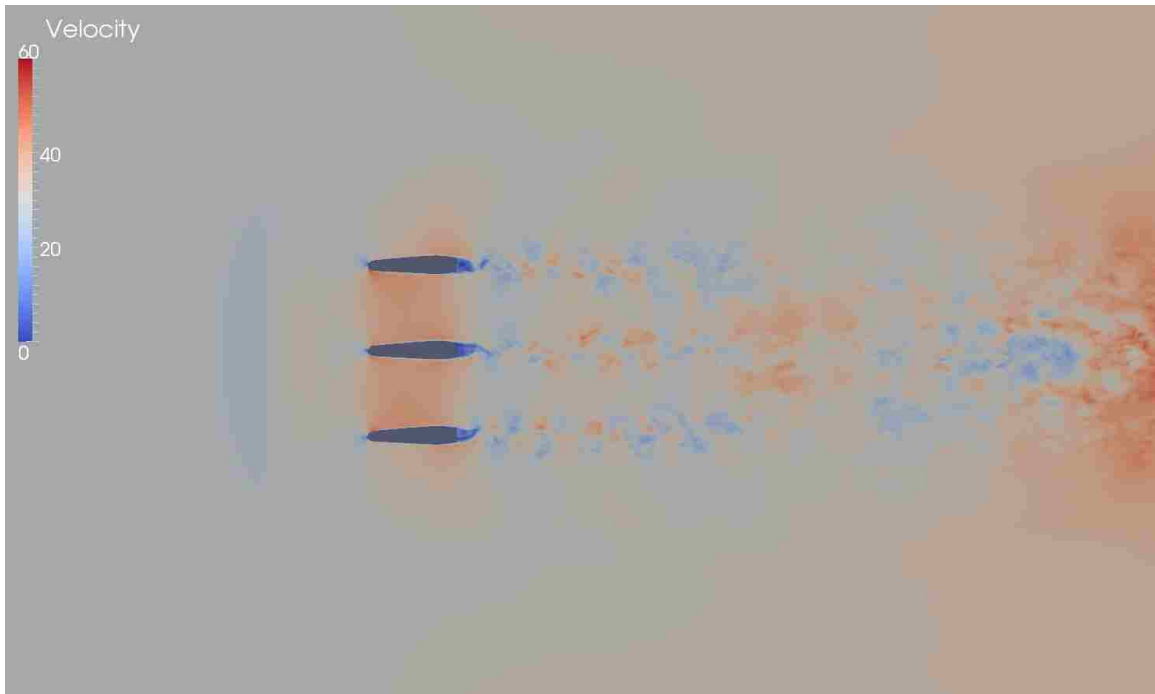


Figure 36: Case 4C Compressible DES Velocity Field

The accompanying pressure field appears to be strongly influence by the above velocity abnormality. The faint resemblance of pressure propagation in Figure 37 could potentially be reflecting off the wave transmissive outlet boundary specifically implemented to prevent this very phenomenon.

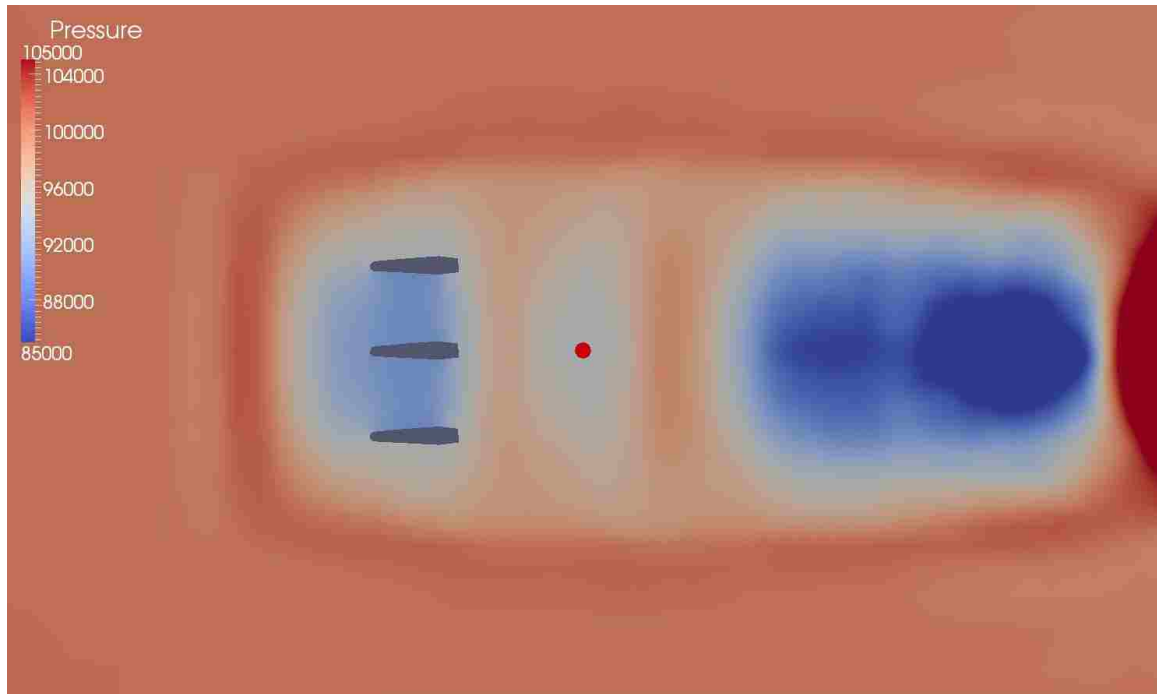


Figure 37: Case 4C Compressible DES Pressure Field

Preceding with the revised profile Figure 38 show some unusual disturbances within the velocity field as it was for the original geometry. In this image the presence of propagating pressure waves are visual in the alternating bands of high and low velocity regions that correlate with the varying pressure regions in Figure 39. The tighter grouping of the fluctuating pressure regions reiterates the phenomenon of higher frequency pressure waves for the stepped geometry than for the original profile. Looking at the arched shape of the pressure waves for Case 4D it appears that the outlet may be contributing with the reflection of the waves intended to leave the domain. Further investigation of the patterns seen in the compressible pressure fields will be discussed in the next chapter.

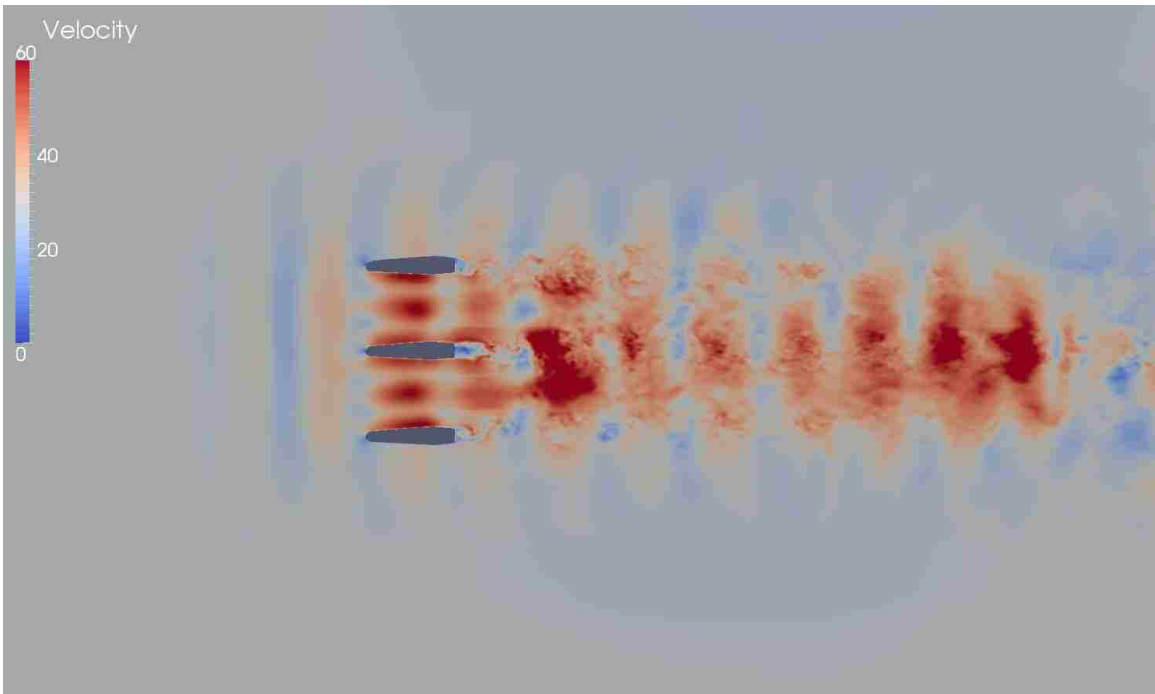


Figure 38: Case 4D Compressible DES Velocity Field

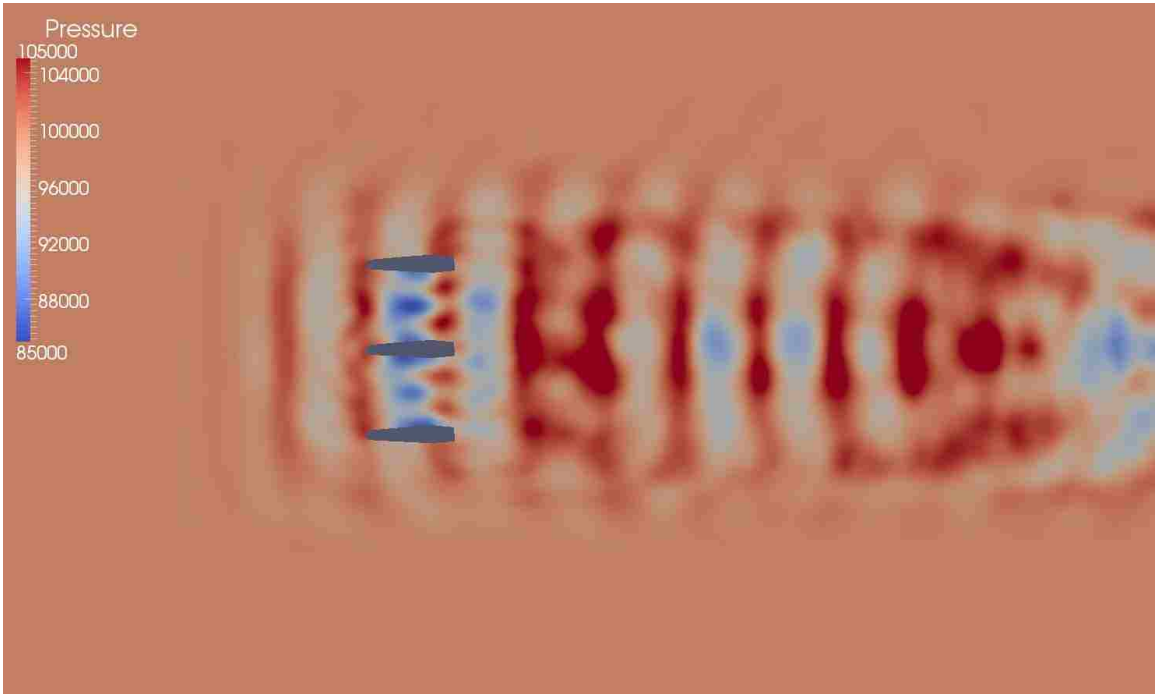


Figure 39: Case 4D Compressible DES Pressure Field

Power Spectral Density Analysis

The visual results for the flow fields of the simulations do not present all the key factors needed to provide an understanding of the research in whole. For this reason the pressure probes were implemented to record the local values at each time step with aims to capture the frequency and intensity of the pressure fluctuations. With these data sets the following PSD graphs are generated through FFT to compare the original and revised geometry by frequency, as it was done experimentally. Beginning again with the Case 1A, Figure 40 presents the peak frequency for the single original profile where the difference in the peak value when comparing to Figure 16 is the result of refinement through the studies previously outlined. At 0 degrees the frequency is double that of any other position around the profile. This is due to this probes position within the wake where the shedding vortices move past both above and below the probe. The location also contributes to its higher amplitude due to the close proximity of the vortices.

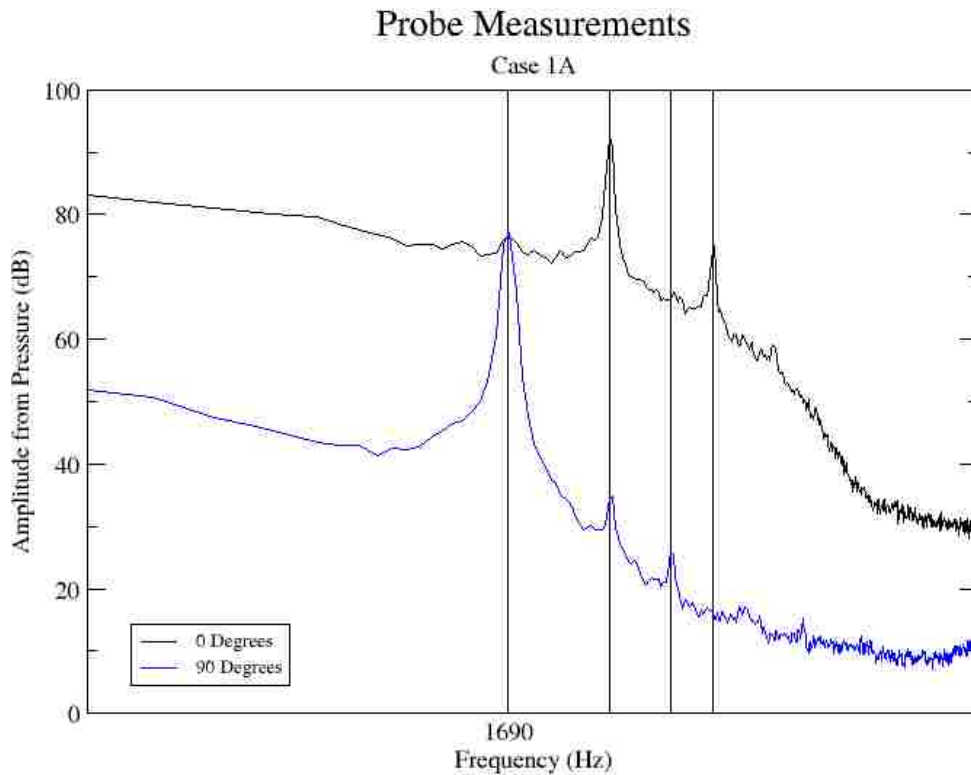


Figure 40: Case 1A DES Probe Measurements

The results of the stepped profile for Case 1B closely reflect those of the Case 1A stating that both geometries will produce the same frequency under the same flow conditions. We know this to be false from the supporting experimental data where we would expect a difference between the two. This conclusion for the single profile DES PSD agrees with the results of the velocity and pressure fields where no visual differences were apparent. The same conclusion is drawn for both the symmetric and cyclic cases.

Figure 41 and Figure 42 show the differences from altering the flow domain and its boundaries to replicate symmetric and cyclic geometric arrays respectively. The symmetric simulations in a higher peak frequency of 1800 Hz at 90 degrees from that of 1690 in the single setup. The amplitudes also vary being lower in the vortex stream and higher at all other probe positions.

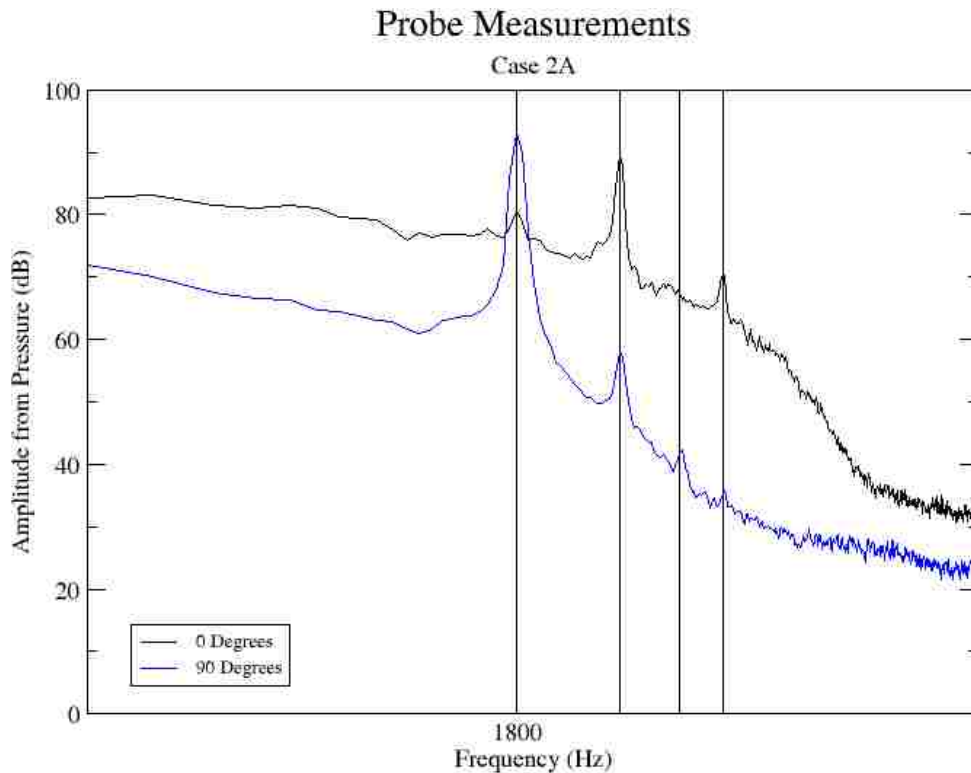


Figure 41: Case 2A DES Probe Measurements

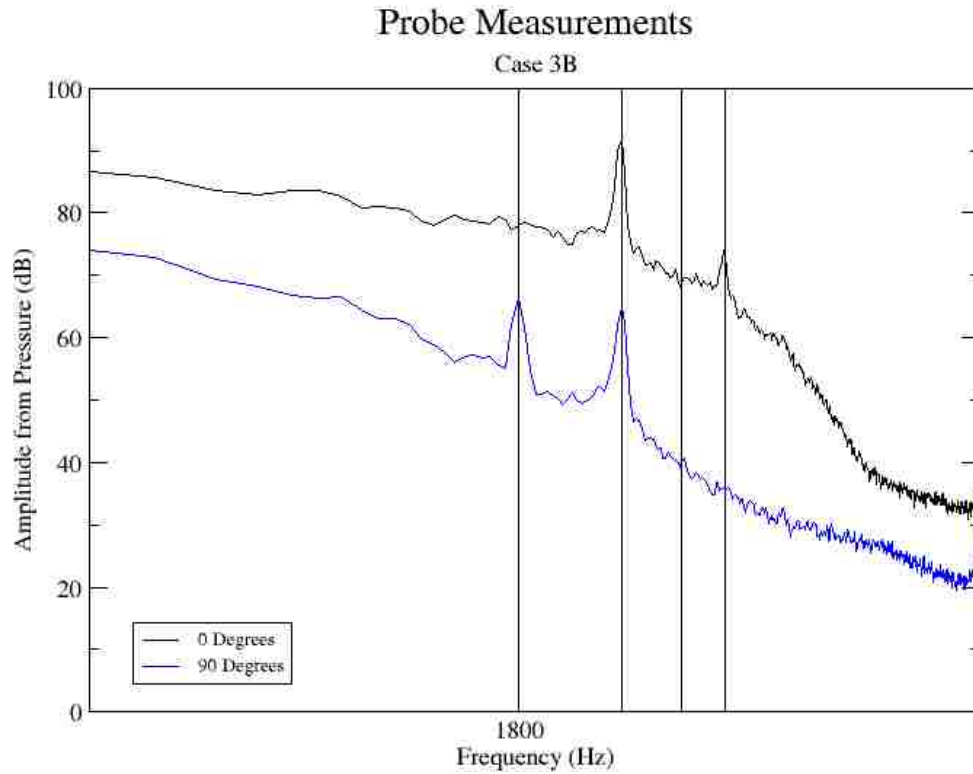


Figure 42: Case 3B DES Probe Measurements

Looking at the cyclic graph the amplitude in the wake is relatively the same as the symmetric scenario but is much lower for all other probe positions. The estimated fundamental frequency however is the same between the two. These results suggest that the wake generated by an array where each individual profile sheds vortices symmetric to those adjacent results in a more intense pressure amplitude than if shedding vortices were cyclic. Figure 43 for the incompressible simulations of the original profile physical array yields a peak amplitude between that of the symmetric and cyclic cases. This figure once again represents the results for the revised profile where both reveal a peak fundamental frequency slightly lower than the boundary array cases at 1725 Hz.

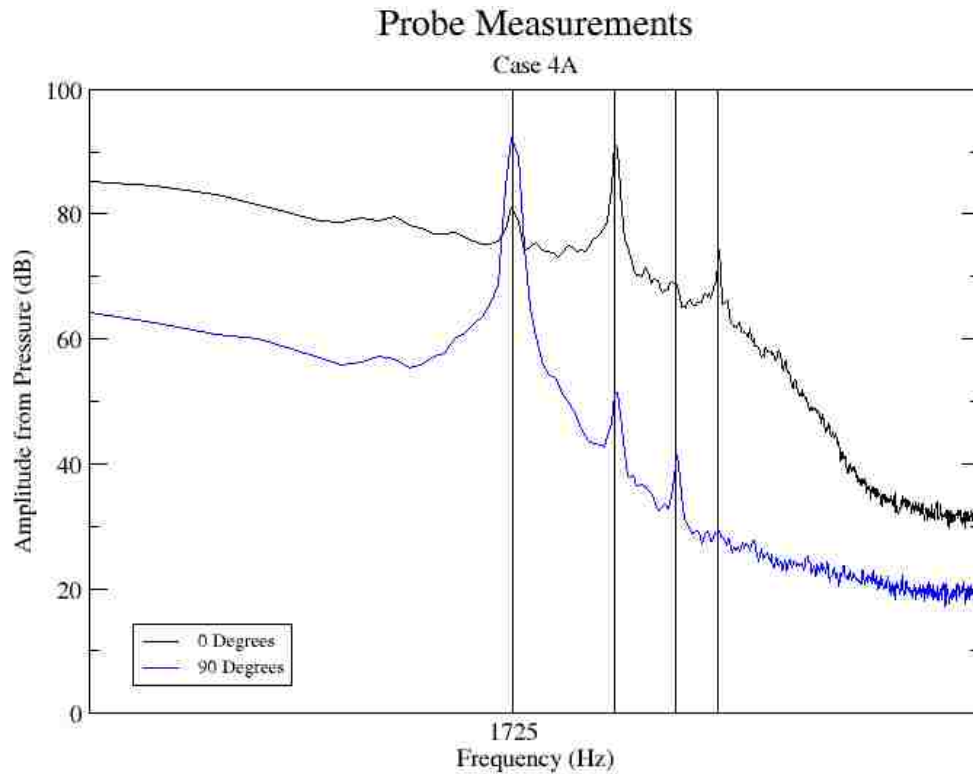


Figure 43: Case 4A DES Probe Measurements

The compressible results for the single original profile differs quite a lot than the incompressible in Figure 40 with the highest pressure peak for the probes, other than 0 degrees, being around 10500 Hz as show in Figure 45 and acts as a fundamental frequency for subsequent spikes. There is also a peak around the 1800 Hz depicted previously in the incompressible boundary array evaluations. For the revised profile an additional probe was included in the three images provided to highlight the peak pressure frequencies since the probe at 90 degrees didn't accurately represent those at 30 and 330 degrees. The fundamental frequency, although weak, appears around 2100 Hz where the first harmonic is the peak pressure for the probe at 0 degrees. The probes represented by the 90 degrees curve have a fundamental frequency of around 11500 Hz and those at 30 and 330 degree have its highest peak at around 29400 Hz. These are presented in Figure 46, Figure 47 and Figure 48.

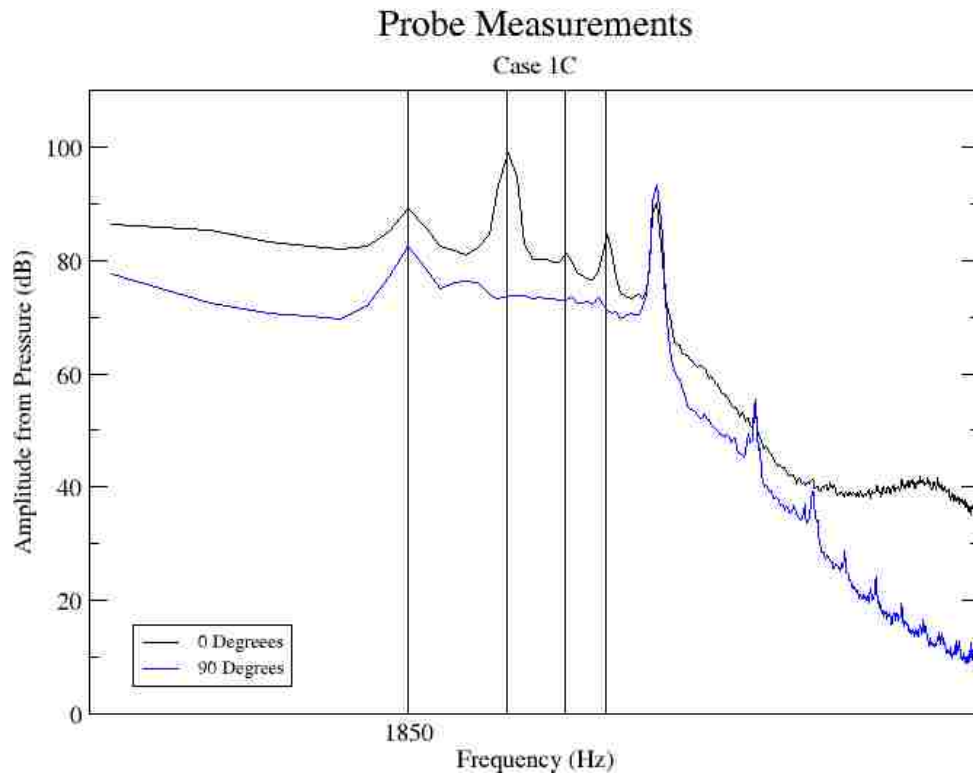


Figure 44: Case 1C Compressible DES Probe Measurements

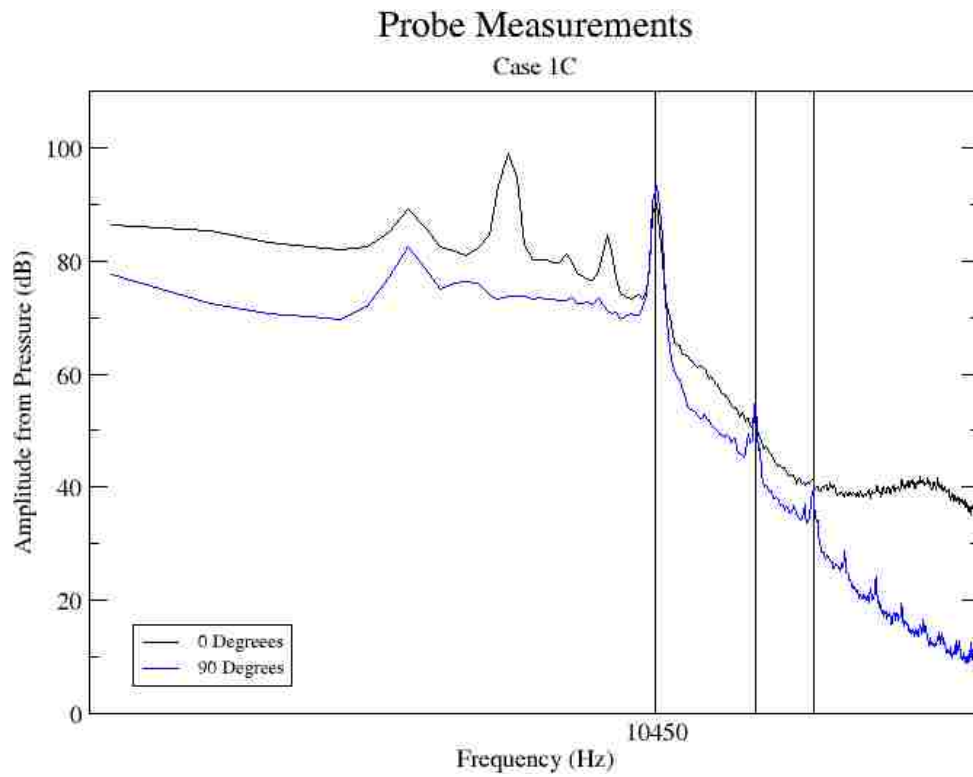


Figure 45: Case 1C Compressible DES Probe Measurements

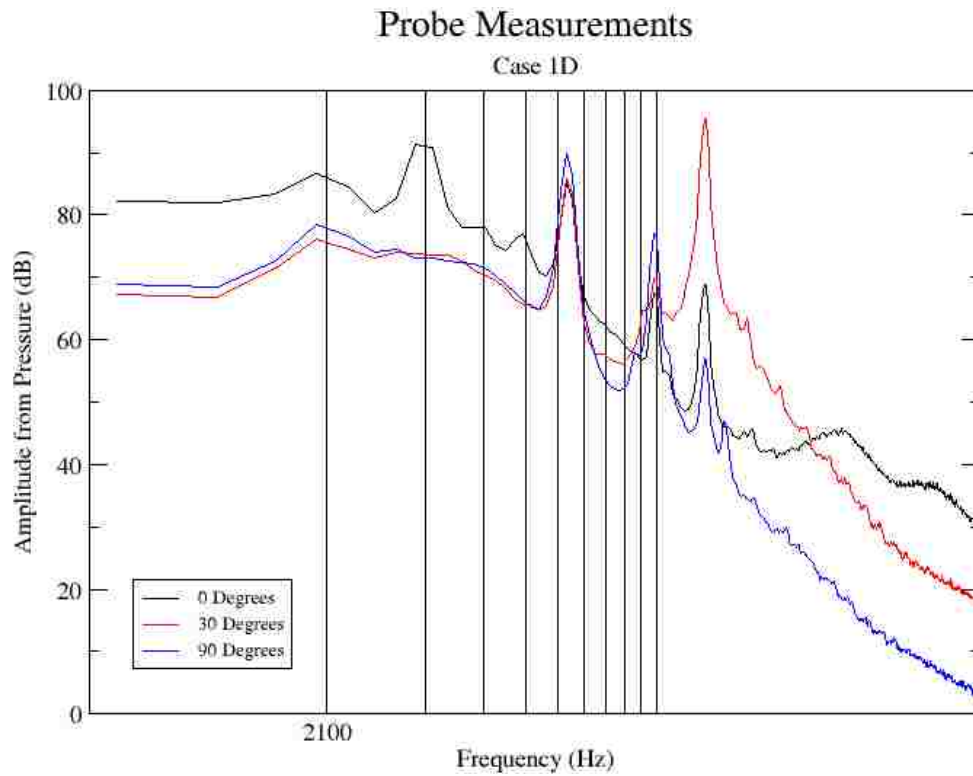


Figure 46: Case 1D Compressible DES Probe Measurements

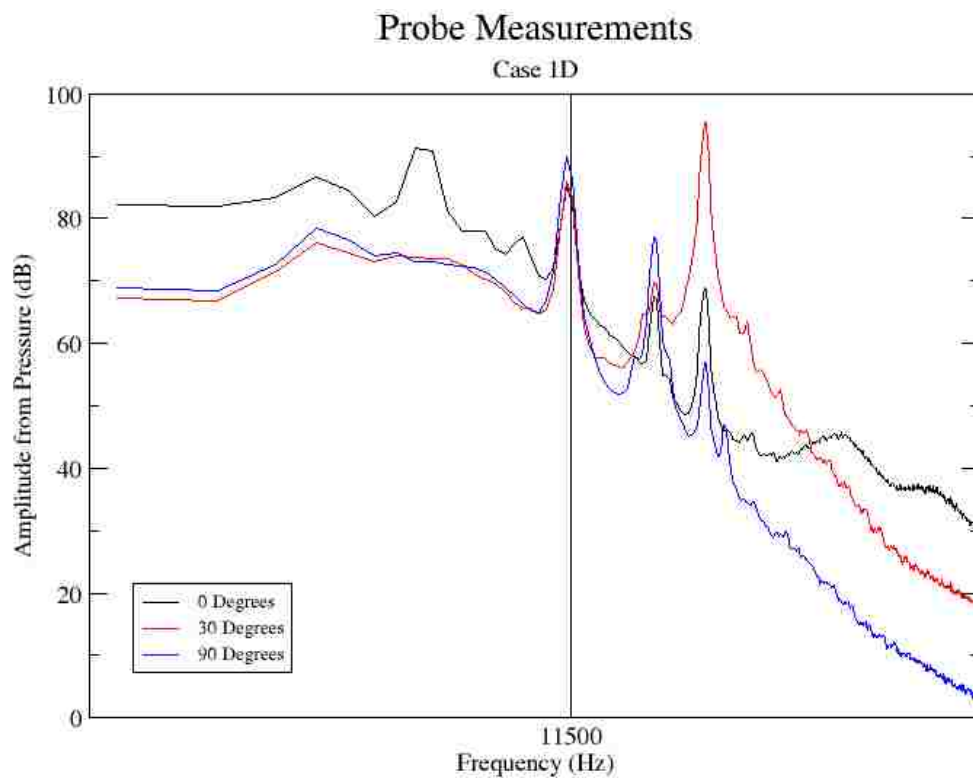


Figure 47: Case 1D Compressible DES Probe Measurements

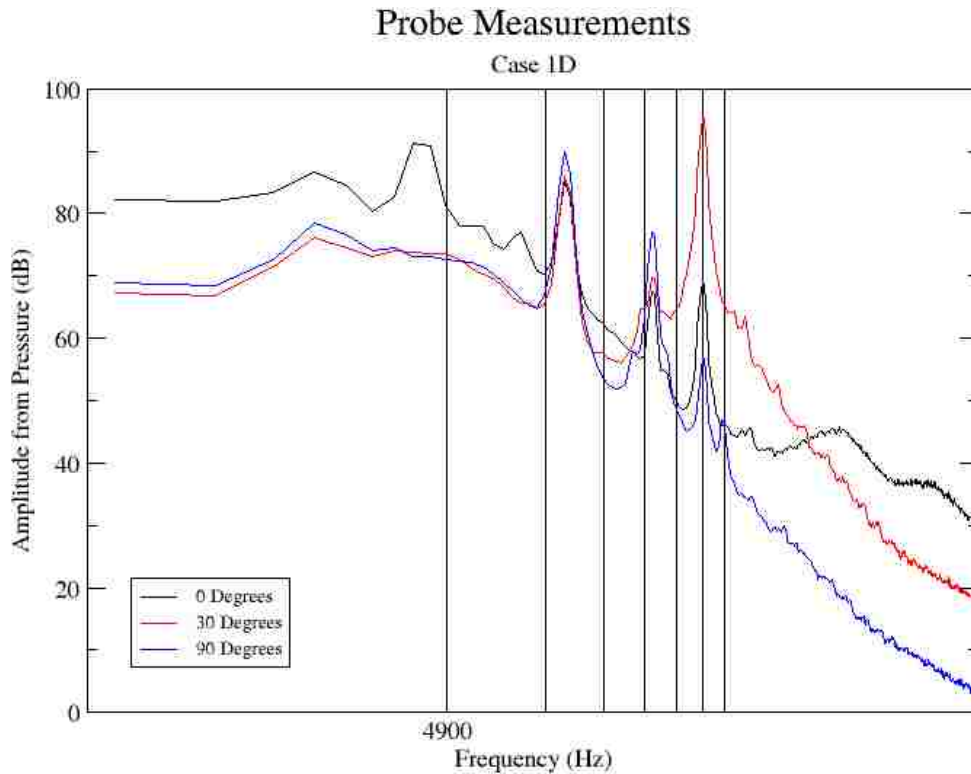


Figure 48: Case 1D Compressible DES Probe Measurements

Lastly the results from compressible simulations of the physical array of three fins are presented. Immediately it can be seen from Figure 49 that the original profile shows nearly the same curve for all probes. As it was for the single profile there appears to be two fundamental frequencies yet with the lowest have a value of approximately 3600 Hz and the highest around 10000 Hz. The figures for the revised profile show that the 30 degrees probe, and symmetrically at 330 degrees, are experiencing the same frequency peaks as the probe at 0 degrees directly in the wake with a lowest fundamental frequency of about 6700 Hz and the probe at 90 degrees has its highest amplitude pressure peak at approximately 30000 Hz. While the incompressible and compressible cases for a single profile showed similar peak amplitudes, the original and revised compressible cases for three fins yielded a peak pressure amplitude fluctuation of 30 to 40 dB higher than their respective incompressible results. The peaks for Case 4D and their marked frequencies are provided in Figure 51, Figure 52 and Figure 53.

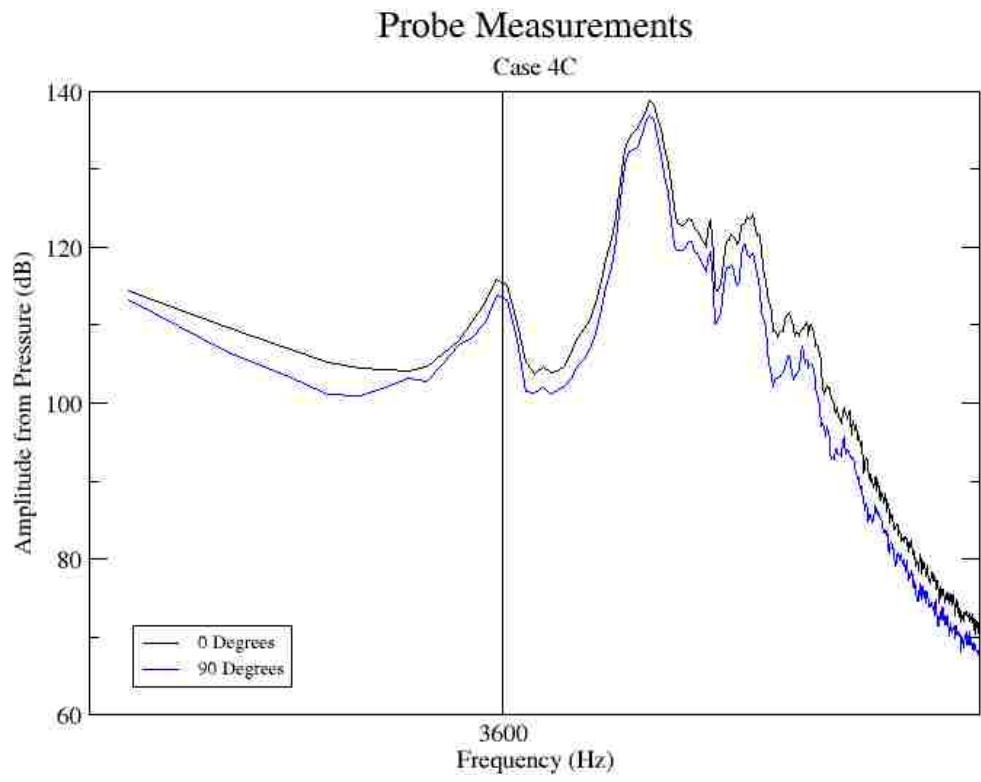


Figure 49: Case 4C Compressible DES Probe Measurements

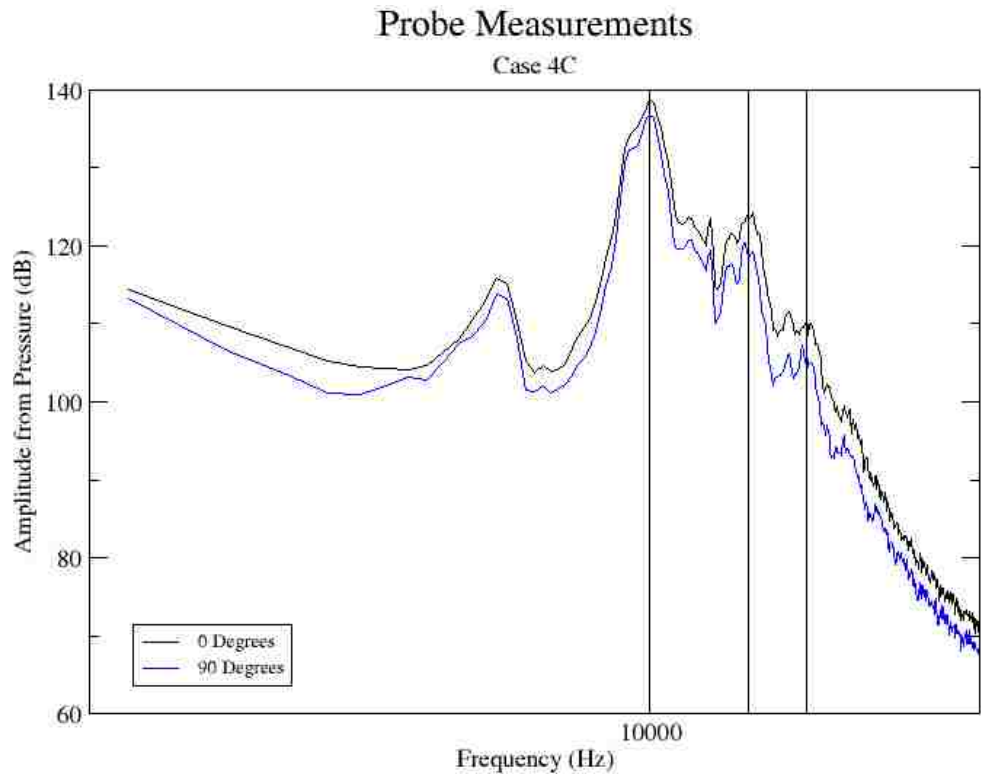


Figure 50: Case 4C Compressible DES Probe Measurements

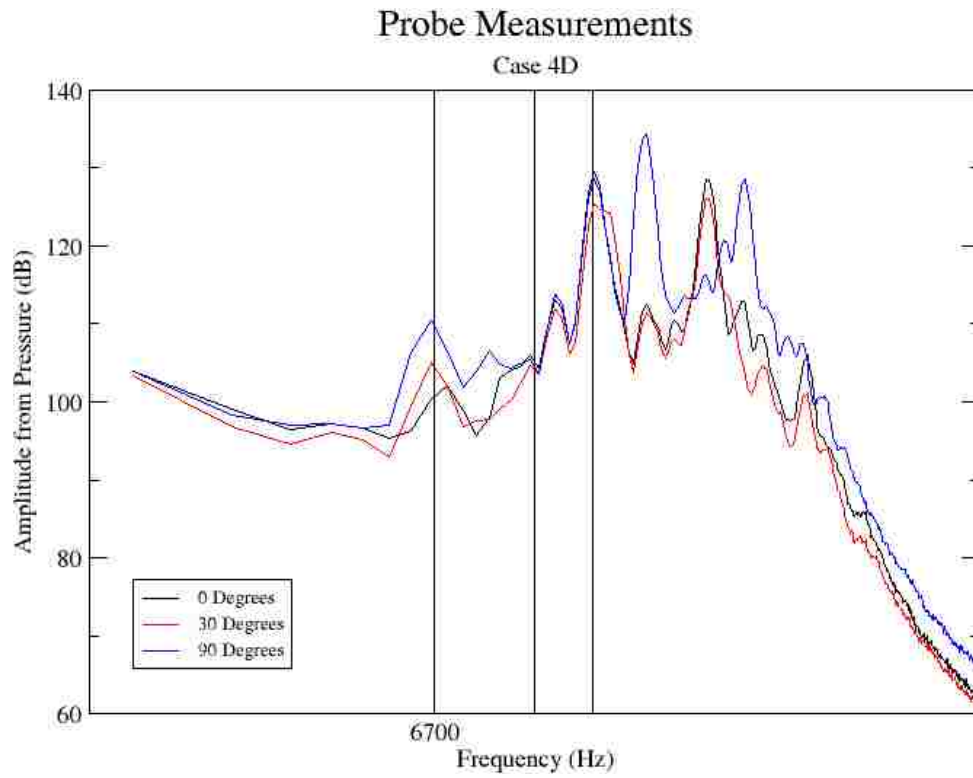


Figure 51: Case 4D Compressible DES Probe Measurements

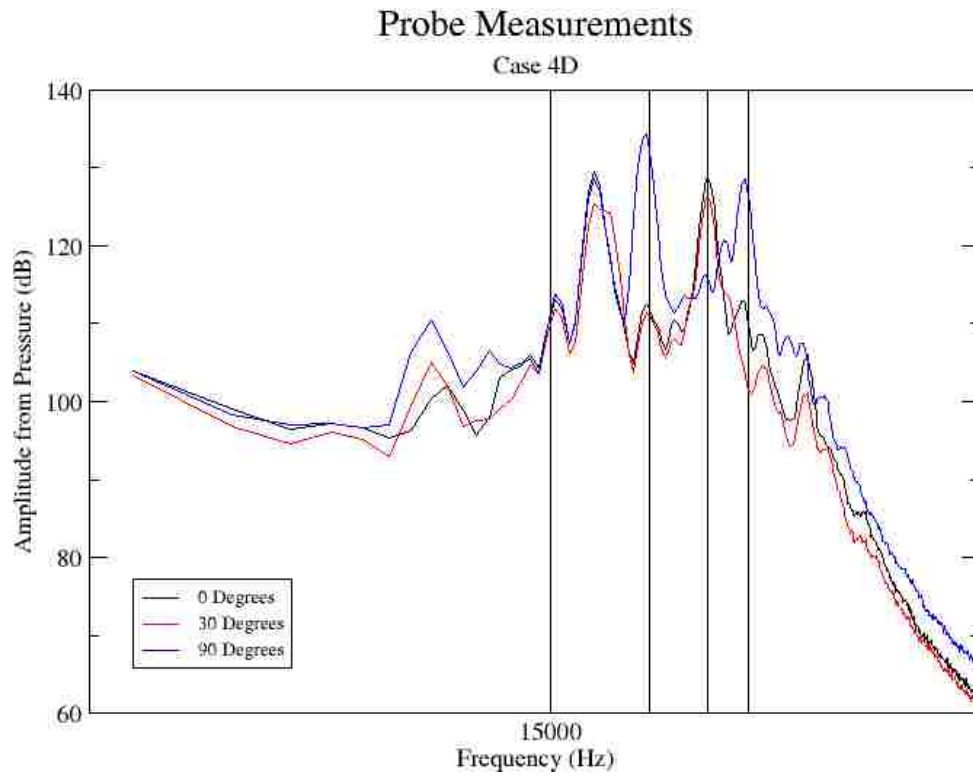


Figure 52: Case 4D Compressible DES Probe Measurements

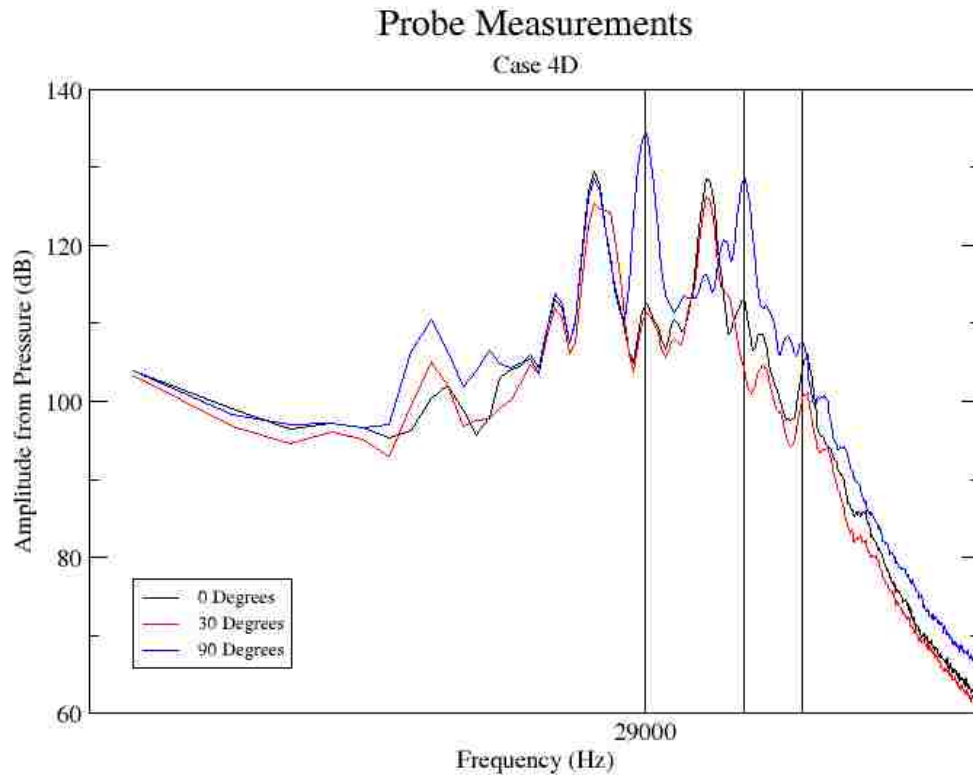


Figure 53: Case 4D Compressible DES Probe Measurements

CHAPTER V
DISCUSSION

In this chapter the findings of the simulations presented previously are discussed to determine the significance of their results. As a reference the experimental data provided at the beginning of the thesis in Figure 6 will be presented in the same manner as the simulation probe results for easier comparison. Figure 54 shows the recorded audible noise frequencies of a test run at 140 km/h on the isolated grill fixed to the support illustrated earlier. As depicted in Figure 6 the frequency of the sound recorded is constant for large ranges of flow velocities and thus comparing these results to the simulations run at 100 km/h should be acceptable. From the simulations we would expect to yield curves and peak frequencies similar to the one seen in this figure below.

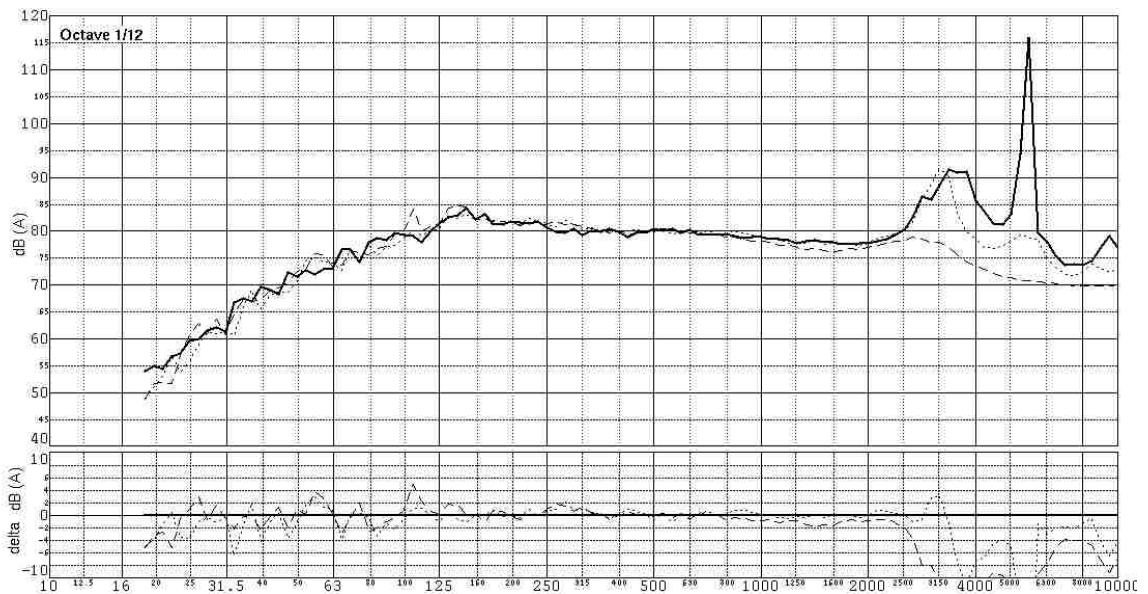


Figure 54: Results of Experimental Tests

Solid Line: Original grill geometry
Dotted Line: Revised grill geometry
Dashed Line: Grill fixture without part

Immediately we can begin to conclude from the peak frequencies indicated in all the incompressible cases that they do not relate to the audible noise captured from the experimental test which measure more than double the simulated results. Rather these incompressible results better represent the frequency of the physical pressure fluctuations of the wake measured by hot wire anemometer and recorded to be near 750 Hz. Though the refined incompressible cases yield a peak frequency of twice this value the initial incompressible simulation for a single profile of original geometry produced a value within 100 Hz (Figure 16). It would appear that an incompressible approach will not suffice to predict the complex interactions of adjacent vortex steams. This is likely due to the inherent nature of instantaneous wave propagation.

Investigating the results of the compressible cases there are visibly large differences in the curves of the single profiles in comparison with the physical array. These flow predictions suggest that the audible phenomenon is a product of multiple fins in close proximity where the pressure waves propagating from their shedding vortices are interacting with those from adjacent wakes. The probe at 0 degrees in the single compressible cases such as in Figure 44 show resemblance to the curves in the experimental data but the peak frequencies are much lower, again with the first peak occurring at around 1800 Hz as opposed to the approximate 3600 Hz expected. When moving away from the wake the probes show negligible correlation to the experiments in regards to frequencies.

The array of three bodies under compressible DES evaluation better resemble the frequencies at which the peaks occur as well as their relative amplitudes and holds true for not just the probe within the wake but at all positions radially around the central geometry. The amplitudes of the three fin array are also visibly higher than the single fin in Case 1C and 1D. The results for both the original and revised profile arrays are presented together in Figure 55. From this it is clear that the original geometry has a maximum peak which follows an initial peak of lesser amplitude, a trend that is found in the experimental recordings. This first peak occurs at approximately 3600 Hz and agrees well with the physical results however the maximum is simulated to present

itself between 8000 and 10000 Hz, substantially higher than the 5550 Hz yielded from the microphone recording. This large error could stem from the abnormalities pointed out in the previous chapters.

Figure 56 shows the pressure measurements for this case at the probe located in the wake at 0 degrees. The first section of negligible pressure fluctuation closely resembles the output from the RAS solution used to initiate the DES domains. Figure 57 shows the same probe location for the revised profile and is representative of the other DES cases as well. Case 4C almost appears as if the compressible DES solver had not initiated until almost 0.2 seconds. This shortened run time from 0.200 to 0.275 seconds in addition to the flow abnormalities seen in Figure 36 and Figure 37 it suggests that the flow may not have reached quasi steady-state throughout domain by the final time step. After reviewing the case setup files for this simulation there were no error to be found related to simulation start and end times. As mentioned before, this case was run several times each yielding very similar results.

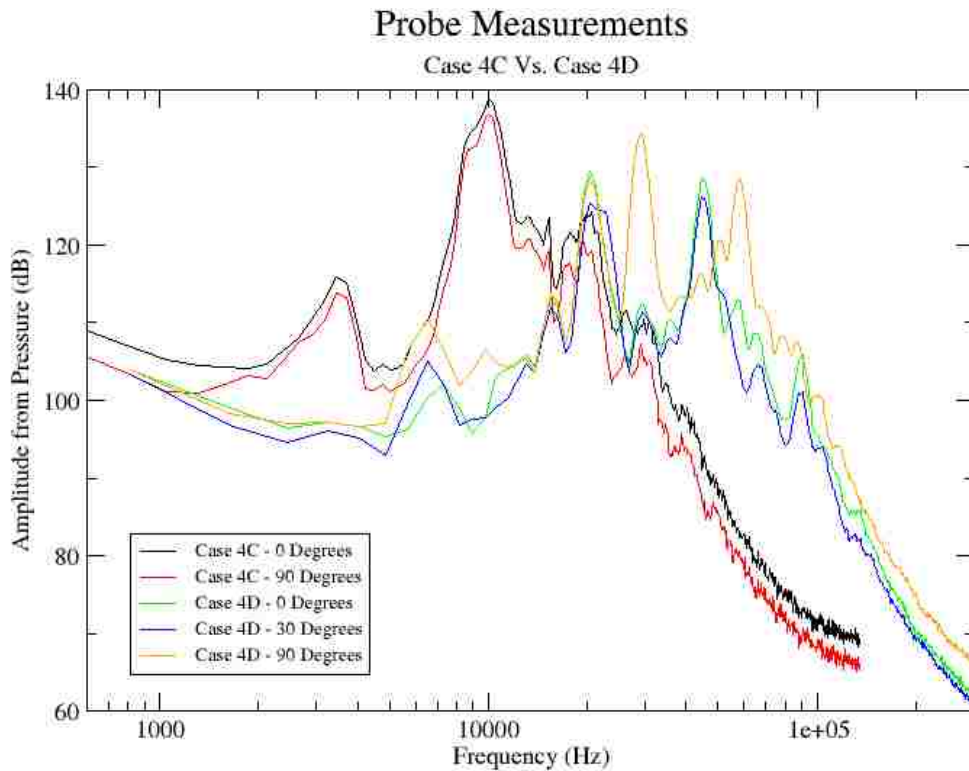


Figure 55: Case 4C versus Case 4D Compressible DES Probe Measurements

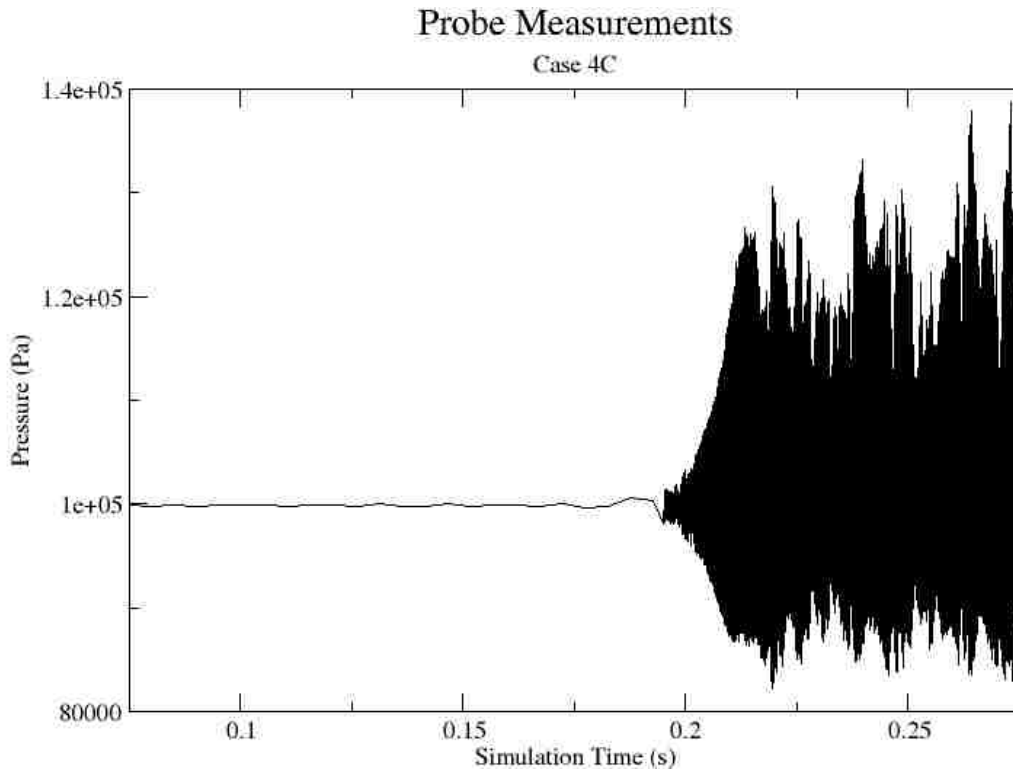


Figure 56: Case 4C Simulation Pressure at 0 Degrees Probe

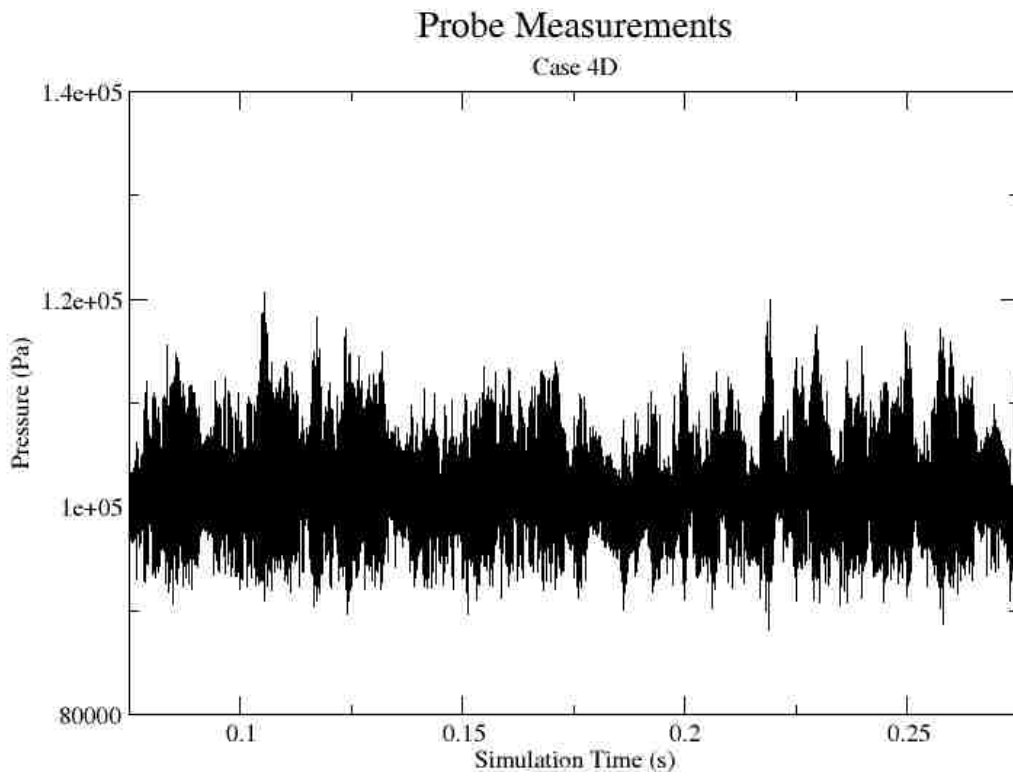


Figure 57: Case 4D Simulation Pressure at 0 Degrees Probe

With this inconvenience aside and looking at the delta between the high and low pressure limits it is evident that the original profile has a greater value than the revised geometry and is reflected in Figure 55. As it is seen this results in the original profile having a greater decibel level of approximately 10 dB for the first two peaks. The following equation relates decibel level to perceived loudness:

$$\Delta SPL = 10 \cdot \log_2(x) = 10 \cdot \frac{\log(x)}{\log(2)} = 33.22 \cdot \log(x) \quad (5)$$

Where x is the ratio for perceived loudness and can be rearranged for as follows:

$$33.22 \cdot \log(x) = \Delta SPL \rightarrow \log(x) = \frac{\Delta SPL}{33.22} \rightarrow x = 10^{\frac{\Delta SPL}{33.22}} \quad (6)$$

Substituting 10 dB in for the sound pressure level a loudness ratio of 2 is yielded meaning that the original profile creates a pressure fluctuation capable of producing a tone twice as loud as the revised profile according to these simulation results.

As an additional evaluation of the erroneous data for Case 4C the first section related to the RAS results were removed from the data set used for the PSD analysis. This resulted in nearly the same curve however the first and second peak shifted further up the frequency spectrum and in line with those of Case 4D as it is seen in the experimental results. With this revision three major differences exist between the experimental and simulated results.

The first item is again the position of the frequency peaks. The position of 6700 Hz and 20000 Hz is quite far off from the 3600 Hz and 5550 Hz expected for the first and second peaks. This could be the result of many things stemming from the setup of the simulations such as the use of an unstructured mesh, mesh resolution, simulation run time, choice of solver etc. In order to determine which combination would achieve

results that better reflect the experiment further research and studies would have to be conducted. These variables may also contribute to the second item of interest being the second peak for Case 4D. The experimental results do not show such a peak of this relative magnitude for the revised profile. The third major item that stands out is the magnitude of the SPL. As it was for the first two items the setup of the simulation will have an impact on the amplitude of the calculated pressure fluctuations and the positions of the probes relative to these undulations will change as they are moved further from the source. The experimental data has also plotted frequency against the A-weighted SPL generated from the front grill. This is simply an adjustment to the actual decibel levels to account for the sensitivity of the human ear across the frequency spectrum.

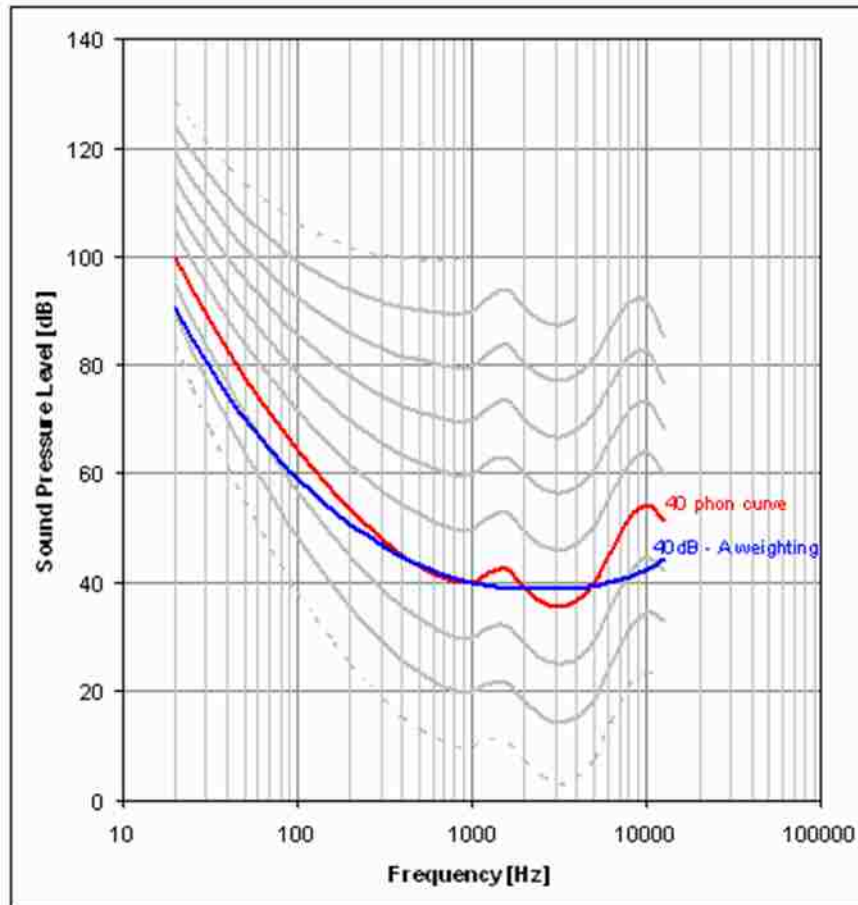


Figure 58: A-Weighted Curve

Figure 58 shows the A-Weighted curve that approximates the 40 phon curve which is the result of extensive research on many groups of subjects. This curve is constructed around a noise of constant power at the 1000 Hz frequency having an SPL of 40 dB. As the frequency is adjusted at constant power the curve will intersect a decibel level that would be perceived as the equivalent loudness of 40 dB. For example at 3000 Hz a tone with approximately 38 dB would be perceived at an intensity of 40 dB. When comparing simulated results to this curve it is found that the peaks at 6700 Hz fall in a range of hearing far more sensitive than the 20000Hz range, which is the upper extent of the human hearing range. Thus the noise heard is most likely that of the first peak.

Investigating the results of the simulations further the SPL of each probe can be plotted in space to get an idea of where the emanating source is located. Figure 59 suggests that the strongest sound source for the original profile is located somewhere downstream of the trailing edge of the array where the revised case in Figure 60 suggests that the strongest source for noise is somewhere between the array geometries near the position of the step.

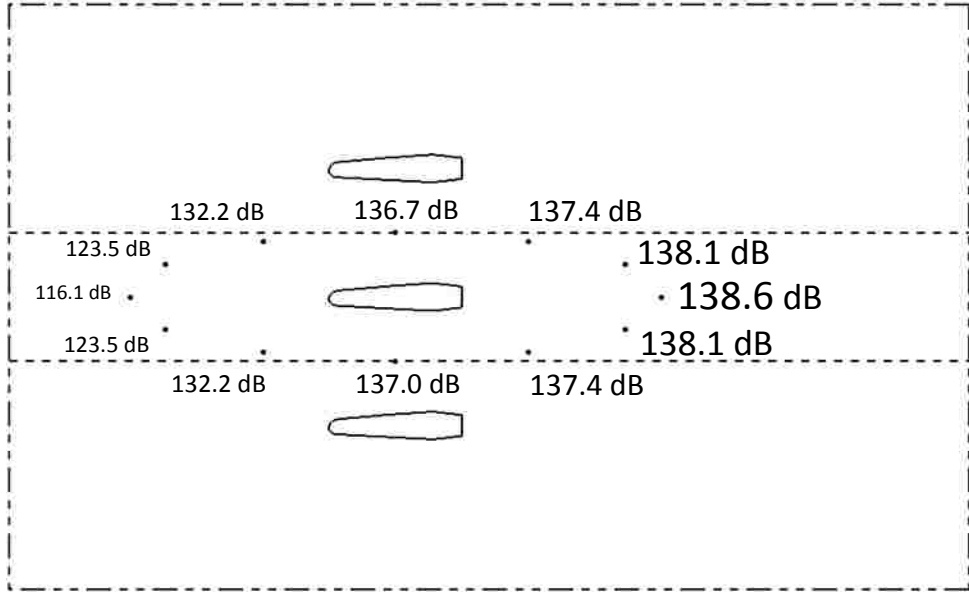


Figure 59: Case 4C Probe Sound Pressure Levels

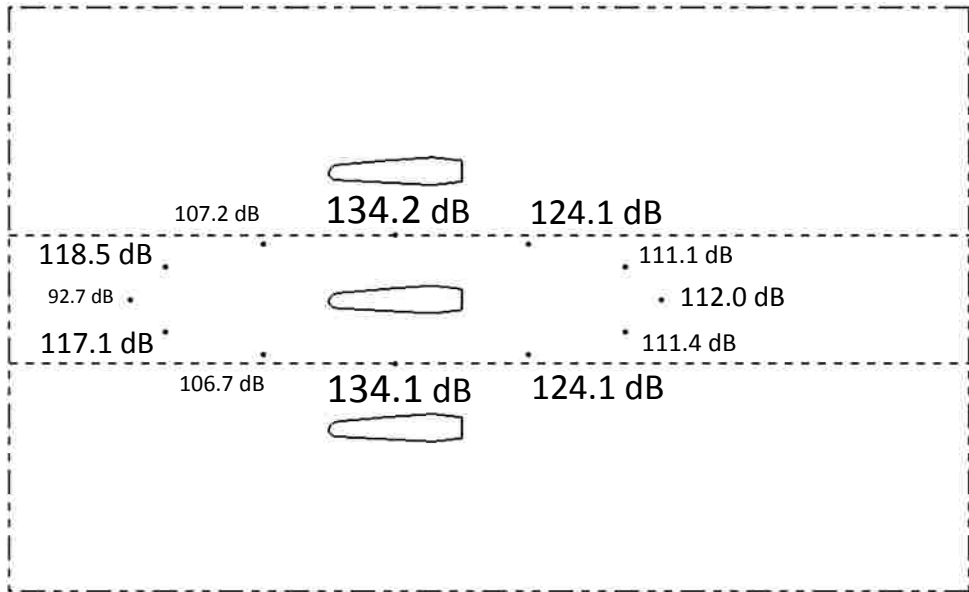


Figure 60: Case 4D Probe Sound Pressure Levels

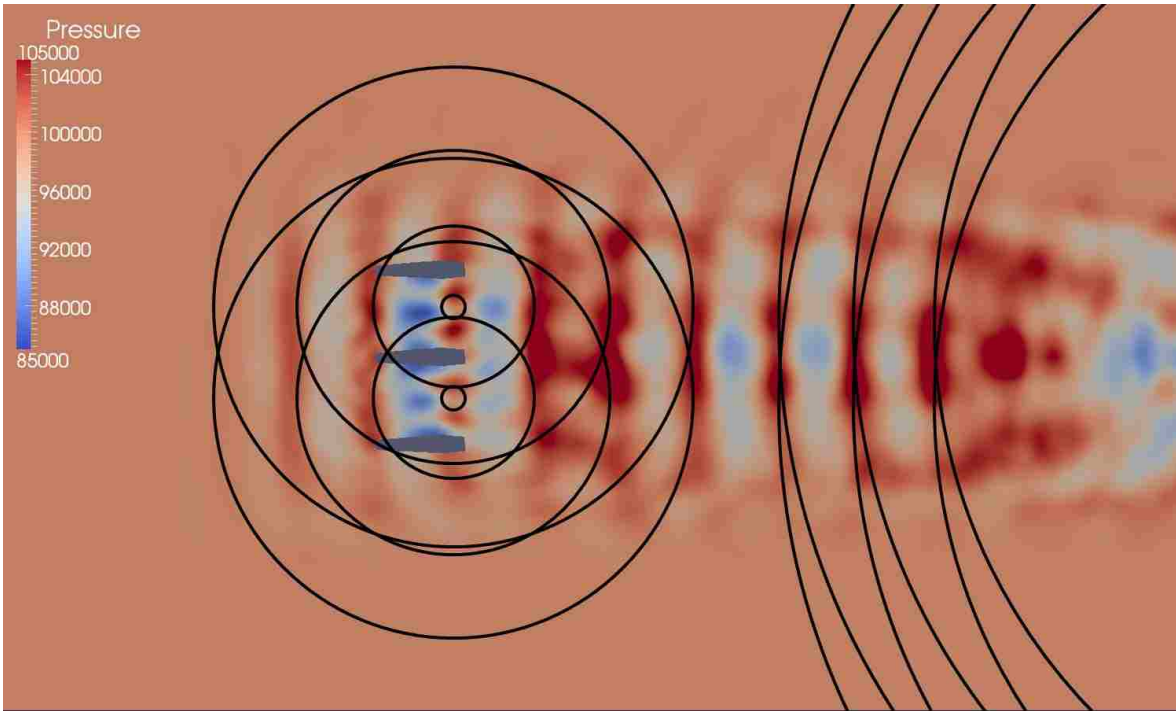


Figure 61: Case 4D Pressure Wave Propagation

Figure 61 provides a graphical representation of what the propagation from the assumed sound sources for the revised geometry would potentially look like. Also included is the possible reflection of the pressure waves off the outlet. If the latter coexists with the former then perhaps this interaction is responsible for the near doubling of the expected peak frequency of 3600 Hz that the experimental evaluations yielded. For this reason the outlet boundary conditions should be reevaluated and refined to allow the frequency of 3600 Hz to pass through more efficiently. Another possible source for pressure fluctuation is from the domain mesh itself. With the use of an unstructured mesh there exists a rapid change in the cell size in comparison to a structured mesh as the resolution is adjusted over the domain. This could generate artificial pressure fluctuations at the interfaces of these mesh resolutions changes and ultimately influencing the predicted fundamental frequencies of the noise source.

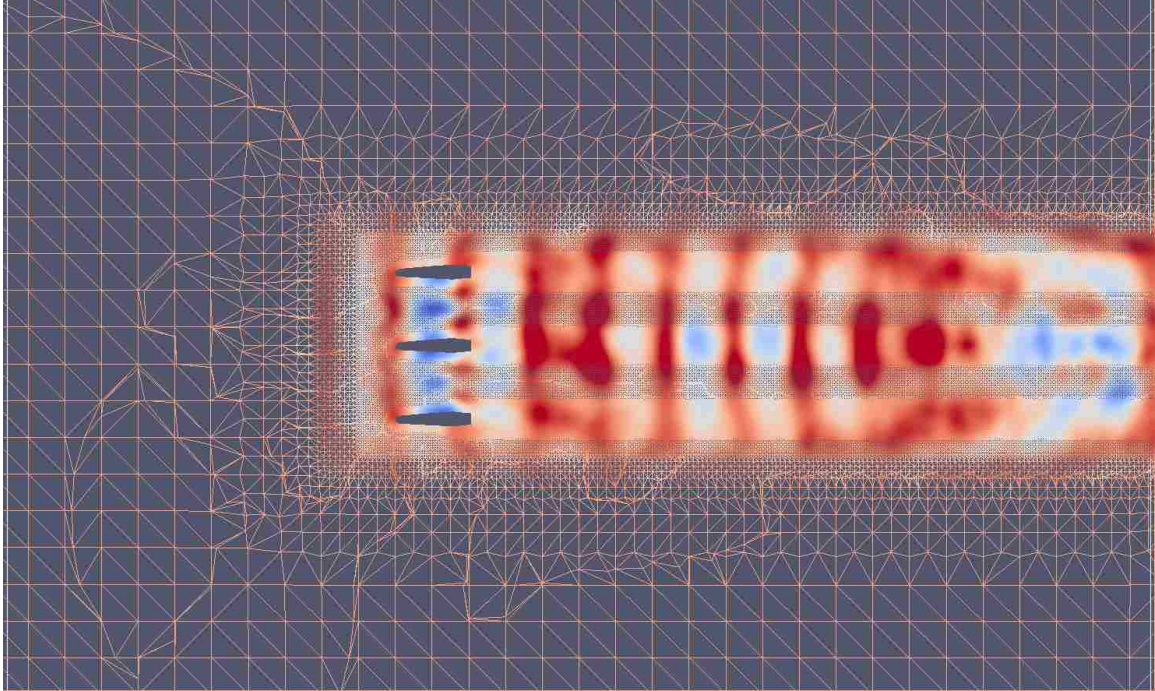


Figure 62: Pressure Field over Mesh Resolution

Figure 62 show agreement to this phenomenon with the high pressure regions at the boundaries of the changing mesh size. It also shows that as the resolution become very coarse the pressure waves are no longer visible due to the lack of points that are required to accurately capture the detail. As mentioned in the literature review a good representation of a wave usually requires a minimum of 7 points per wavelength. Perhaps if the mesh resolution was constant over all three wake regions the pressure waves may appear as solid vertical lines. The use of a structured mesh would have most likely minimize this effect but as mentioned in the literature review implementing this type in OpenFOAM while using a quasi-3D domain is a very cumbersome task.

The pressure fields for the compressible cases can also be used to estimate the frequency of fluctuations through measuring the distance between the high pressure bands and using the following equation:

$$f = v/\lambda \quad (7)$$

$$\lambda = \textit{Wavelength}$$

$$v = \textit{Wave propagation velocity (340 m/s in air)}$$

$$f = \textit{Frequency}$$

The measured wavelength Case 4C was approximately measured to be 40 mm resulting in a predicted frequency of 8500 Hz. This value may not agree to the 10 000 Hz maximum pressure peak yielded through FFT but it is close considering the measurements are taken from a pressure plot of fairly low detail. The same can be said for Case 4D with a measured value of 20 mm suggesting a peak value of 17 000 Hz in comparison to the 20 000 Hz pressure peak achieved through FFT. Perhaps if the mesh was finer to provide a sharper pressure plot precise measurements could be made that better reflect the FFT analysis. The secondary peaks visible in the FFT's are not visible within the pressure field because the amplitude of the largest peak pressure fluctuations dominates over the amplitudes of the subsequent peaks.

CHAPTER VI

CONCLUSION

From these findings presented it may be possible that the frequencies of the experimental noise of the front grill of a vehicle can be predicted using a refined compressible DES evaluation of the flow domain around a small section of the geometry in question. The results produced were not accurate in accordance with those of the experiment but they did show similar trends in spacing and relative amplitude of the apparent frequency peaks. With some further refinement perhaps the correct frequency can be achieved but at the cost of more computational resources. The outcome of the research conducted suggests that an accurate predictive method will likely require reasonably large amount of resources to capture the correct frequency of the phenomenon.

Recommendations

After evaluating the results of each case several areas of improvement have been realized for future works regarding the need of a low-resource, dependable and quick prediction of possible noise predictions of a particular design. OpenFOAM seems to be a capable toolset in using CFD in predicting the pressure fluctuations that are potentially linked to the noise source that is sought after. To ensure these predictions contain enough information to make an accurate assumption of whether a geometry is a good design free of producing an audible noise source other proven software designed for aeroacoustic computation should be implemented on the same geometry as a benchmark to further confirm that OpenFOAM CFD is an inexpensive and reasonable program for preliminary design evaluation of vehicle components. One major area to consider changing in the OpenFOAM cases themselves is the mesh discretization from and unstructured form to a structured form. This was initially avoided for its demand of intensive construction and large amount of time required for creating a quality

structured mesh, though they often require less computation time than unstructured meshes due to their more efficient algorithms.

Another item for further consideration is the non-reflective boundaries implemented at the outlet and the upper and lower wall for the compressible cases. If there is indeed the presence of reflected pressure waves present within these simulations then there could be some further settings available for this boundary utility in refining the performance and yielding better results, or perhaps an alternative developed by the open source groups that contribute to this code. One easy method to visually identify if reflection is in fact occurring at the wave transmissive boundaries is to create a short video of several time steps. One was not created during this research due to limited storage space available at the industry partner facility. The smallest DES meshes of 2.2 million cells would generate such a large volume of data that only a few frames worth of time steps could be stored. To better understand the wave transmissive utility a set of simulations could be conducted on known flow models such as NACA air foils, Ahmed bluff bodies or resonating cavities. Areas of studies such of those listed often have a common geometry evaluated in a flow with specific parameters that has been studied by several different researchers using a variety of software. The accumulated results would provide a sound basis for benchmarking the use of non-reflective boundaries in OpenFOAM in evaluating their effectiveness. In relation to the wave transmissive boundary implementation there was the issue with achieving convergence for the cyclic and symmetric arrangements where the geometry was in close proximity with these boundaries. Despite the attempt to achieve compressible cases for these boundary arrays and support from a third party software company a comparison of these to the physical array of three fins could not be provided. From the results provided for the incompressible symmetric and cyclic boundaries there would be no need to further investigate convergence of the compressible cases due to their inaccurate representation of the geometrical array.

There is also the question of the simulation time acquired for the PSD analysis. It is possible that using only 0.25 seconds is not adequate in accurately revealing the

frequency of the pressure peaks generated. Although there was a study performed to determine how long of a simulation time was required for maintaining reasonable accuracy it was performed on an incompressible DES case for a single profile to reduce the total amount of labour involved in creating these evaluations, as this was a criteria to be met for this research. Now knowing that the incompressible cases were not capable of reproducing the experimental data trends, focus can be set on refining the compressible cases in aims to create a methodology for quick and adequate prediction of possible noise generation. There is also the option of exploring other types of solvers, such as the DDES that is available in the OpenFOAM toolkit potentially achieving better results than DES as it was designed to be an improvement on this approach. Evaluating the performance of various turbulence models against Spalart-Allmaras could have revealed a more efficient option. Despite solving for an additional equation the use of a two equation model such as k-omega-SST could have performed better than the one equation Spalart-Allmaras if implemented on a good mesh. OpenFOAM has two utilities available to calculate and output y^+ values at various time steps which their values could be utilized to select a more appropriate turbulence model.

Aside from the setting and options available in the code having impact on the results yielded there is also the consideration for the extent of the actual geometry used. With the difference of resulting peak pressure frequencies between the single fin and three fin cases the argument could be made that an array of five fins, as exists with the actual grill component, may predict a completely different peak frequency curve. The interactions between the wakes of a five-fin simulation could result in a frequency prediction that more accurately reflects the experimental evaluations. In this research only a small section of the horizontal fin was used to make these predictions and treated as an infinite length. In actuality the vehicle grill under speculation was constructed of both horizontal and vertical risers. If the interaction of vortex streams of adjacent profiles in close proximity is creating this noise source as suggested in the findings then perhaps the presence of the vertical portions are further influencing the overall pressure fluctuations in the flow domain. For this reason a larger section could

be considered, perhaps an entire boxed region formed by two horizontal and vertical members. It should be restated that this would greatly increase the total number of cells while using a mesh of the same resolution and thus computational time would grow much longer. If it was determined as a necessary section of geometry required in capturing the phenomenon found from experiment then this method would quickly deviate from the goal of being inexpensive in terms of required resources and time.

Another geometric assumption that could have impacted the outcome of this research was treating the geometry as a perfectly rigid body. As mention in the literature review noise is often produced in the presence of a resonating object within a flow similar to those of Aeolian tones. This would have to take the complete geometry into account to accurately simulate the vibrational modes of the grill component as a whole. Having set up the simulations allowing the geometry to deflect in the presence of shedding vortices could have resulted in different frequency values for the recorded pressure peaks completely. With this said analyzing the behaviour of the geometry during experimental procedures would likely have provided critical information on deflection and vibrational characteristics of the grill in the presence of flow. The fixture used to support the grill during experimental evaluation could have also influenced the frequency being measured. Even though an audible noise was being recorded it could have been of a different frequency than what is being experienced in situ. If vibration and flexibility of the support is indeed playing an important role in the production of audible noise then the rigid body simulations will not accurately represent the results of the experiment.

To summarize, it has been concluded that OpenFOAM has potential in achieving the goals set out in this research but further work must be done to improve the accuracy and ultimately determine if a set of criteria in relation to simulation setup can be implemented that achieves a reasonably quick runtime while using minimal resources. Many variables have not been explored in this research and their investigation could potentially yield results that better reflect the measurements of the experimental data.

REFERENCES

- [1] R. F. Jones, "AEROACOUSTICS OF AEOLIAN TONES AND EFFECTS OF PERIODIC HOLES," presented at the 16th Australasian Fluid Mechanics Conference, Crown Plaza, Gold Coast, Australia, 2007.
- [2] J. Milbank and S. Watkins, "DEVELOPMENT OF A SMALL SCALE AEROACOUSTIC OPEN JET OPEN RETURN WIND TUNNEL FOR CAVITY NOISE AND COMPONENT TESTING," presented at the SAE 2000 World Congress, Detroit, Michigan, United States SAE International, 2000.
- [3] V. Madani and S. Ziada, "AEROACOUSTIC CHARACTERISTICS OF AUTOMOTIVE HVAC SYSTEMS," presented at the SAE World Congress & Exhibition, Detroit, Michigan, United States, SAE International, 2008.
- [4] L. Leep-Apolloni, G. S. Strumolo, and W. Gulker, "WIND NOISE SPECTRAL PREDICTIONS USING A LATTICE-BASED METHOD," presented at the Noise & Vibration Conference & Exposition, Traverse City, Michigan, United States, SAE International, 1999.
- [5] J. Park and H. Lee, "NUMERICAL SIMULATIONS OF WHISTLE NOISE FROM AIR VENTILATION DUCT," presented at the SAE 2005 Noise and Vibration Conference and Exhibition, Grand Traverse, Michigan, United States SAE International, 2005.
- [6] E. Védy, L. V. Lier, R. R. Parchen, J. Golliard, and P. J. G. v. Beek, "APPLICATION OF STATISTICAL NOISE GENERATION AND RADIATION FOR ACCOUSTIC NOISE PREDICTIONS IN THE AUTOMOTIVE INDUSTRY," presented at the SAE 2005 Noise and Vibration Conference and Exhibition, Grand Traverse, Michigan, United States SAE International, 2005.
- [7] D. Lepley, S. Senthoooran, D. Hendriana, and T. Frazer, "NUMERICAL SIMULATIONS AND MEASUREMENTS OF MIRROR-INDUCED WIND NOISE," presented at the SAE 2009 Noise and Vibration Conference and Exhibition, St. Charles, Illinois, United States SAE International, 2009.
- [8] A. Ayar, R. Ambs, C. Capellmann, B. Schillemeit, and M. Matthes, "PREDICTION OF FLOW-INDUCED NOISE IN AUTOMOTIVE HVAC SYSTEMS USING A COMBINED CFDCA APPROACH," presented at the SAE 2005 World Congress & Exhibition, Detroit, Michigan, United States SAE International, 2005.
- [9] T. Biermeier and S. Becker, "ACOUSTIC INVESTIGATION OF HVAC SYSTEMS IN VEHICLES," presented at the SAE 2012 World Congress & Exhibition, Detroit, Michigan, United States, SAE International, 2012.
- [10] Y. Li, N. Kasaki, H. Tsunoda, T. Nakamura, and T. Nouzawa, "EVALUATION OF WIND NOISE SOURCES USING EXPERIMENTAL AND COMPUTATIONAL METHODS," presented at the SAE 2006 World Congress & Exhibition, Detroit, Michigan, United States SAE International, 2006.
- [11] A. Devesa and T. Indinger, "FUEL CONSUMPTION REDUCTION BY GEOMETRY VARIATIONS ON A GENERIC TRACTOR TRAILER CONFIGURATION," presented at

- the SAE 2012 World Congress & Exhibition, Detroit, Michigan, United States SAE International, 2012.
- [12] C. Bailly, C. Bogey, and O. Marsden, "PROGRESS IN DIRECT NOISE COMPUTATION," *International Journal of Aeroacoustics*, vol. 9, pp. 123-143, 2010.
 - [13] V. John and A. Tambulea, "ON FINITE ELEMENT VARIATIONAL MULTISCALE METHODS FOR INCOMPRESSIBLE TURBULENT FLOWS," presented at the European Conference on Computational Fluid Dynamics, Delft, The Netherlands, 2006.
 - [14] P. Tóth, A. Fritsch, and M. M. Lohász, "APPLICATION OF COMPUTATIONAL FLUID DYNAMICS SOFTWARES FOR 2D ACOUSTICAL WAVE PROPAGATION," presented at the Gépészet 2008, 2008.
 - [15] F. Mendonça, A. Read, V. G. Silva, and F. H. J. Imada, "EFFICIENT CFD SIMULATION PROCESS FOR AEROACOUSTIC DRIVEN DESIGN," presented at the II SAE Brasil International Noise and Vibration Congress, Santa Catarina, Brasil, SAE International, 2010.
 - [16] Y. Kato, "NUMERICAL SIMULATION OF AEROACOUSTIC FIELDS AROUND AUTOMOBILE REAR-VIEW MIRRORS," presented at the SAE 2012 World Congress & Exhibition, Detroit, Michigan, United States SAE International, 2012.
 - [17] C. K. W. Tam, "RECENT ADVANCES IN COMPUTATIONAL AEROACOUSTICS," *Fluid Dynamics Research*, vol. 38, pp. 591-615, 2006.
 - [18] J. Nilsson, "IMPLEMENTATION OF ACOUSTICAL ANALOGIES IN OPENFOAM AND CALFEM," Lund University, 2010.
 - [19] M. Piellard and C. Bailly, "SEVERAL COMPUTATIONAL AEROACOUSTICS SOLUTIONS FOR THE DUCTED DIAPHRAM AT LOW MACH NUMBER," presented at the 16th AIAA/CEAS Aeroacoustics Conference, American Institute of Aeronautics and Astronautics, 2010.
 - [20] K. y. Takahashi, M. Miyamoto, Y. Ito, T. Takami, T. Kobayashi, A. Nishida, and M. Aoyagi, "NUMERICAL ANALYSIS ON 2D AND 3D EDGE TONES IN TERMS OF AERODYNAMIC SOUND THEORY," in *Proceedings of 20th International Congress on Acoustics*, Sydney, Australia, 2010, pp. 1-8.
 - [21] M. Miyamoto, Y. Ito, K. y. Takahashi, T. Takami, T. Kobayashi, A. Nishida, and M. Aoyagi, "APPLICABILITY OF COMPRESSIBLE LES TO REPRODUCTION OF SOUND VIBRATION OF AN AIR-REED INSTRUMENT," in *Proceedings of 20th International Symposium on Music Acoustics*, Sydney and Katoomba, Australia, 2010, pp. 1-6.
 - [22] B. Lokhande, S. Sovani, and J. Xu, "COMPUTATIONAL AEROACOUSTIC ANALYSIS OF A GENERIC SIDE VIEW MIRROR," presented at the SAE 2003 Noise & Vibration Conference and Exhibition, Grand Traverse, Michigan, United States SAE International, 2003.
 - [23] S. M. Salim and S. C. Cheah, "WALL Y+ STRATEGY FOR DEALING WITH WALL-BOUNDED TURBULENT FLOWS," in *Proceedings of the International MultiConference of Engineers and Computer Scientists*, 2009, pp. 1-6.

- [24] M. Islam, F. Decker, E. d. Villiers, A. Jackson, J. Gines, T. Grahs, A. Gitt–Gehrke, and J. C. i. Font, "APPLICATION OF DETACHED EDDY SIMULATION FOR AUTOMOTIVE AERODYNAMICS DEVELOPMENT," presented at the SAE World Congress & Exhibition, Detroit, Michigan, United States, SAE International, 2009.
- [25] B. Greschner, J. Grilliat, M. C. Jacob, and F. Thiele, "MEASUREMENTS AND WALL MODELED LES SIMULATION OF TRAILING EDGE NOISE CAUSED BY A TURBULENT BOUNDARY LAYER," *International Journal of Aeroacoustics*, vol. 9, pp. 329-355, 2010.
- [26] M. Zhu, Y. Hanaoka, K. Aoki, H. Miyata, and I. Terada, "A NUMERICAL STUDY OF WIND NOISE AROUND FRONT PILLAR," presented at the International Congress & Exposition, Detroit, Michigan, United States, SAE International, 1993.
- [27] V. K. Krastev and G. Bella, "ON THE STEADY AND UNSTEADY TURBULENCE MODELING IN GROUND VEHICLE AERODYNAMICS DESIGN AND OPTIMIZATION," presented at the 10th International Conference on Engines & Vehicles, Naples, Italy SAE International, 2011.
- [28] J. Wojciak, B. Schnepf, T. Indinger, and N. Adams, "STUDY ON THE CAPABILITY OF AN OPEN SOURCE CFD SOFTWARE FOR UNSTEADY VEHICLE AERODYNAMICS," presented at the SAE 2012 World Congress & Exhibition, Detroit, Michigan, United States SAE International, 2012.
- [29] L. Gagnon, M. Richard, G. Beardsell, and M. Boudreau, "THE PROCESS OF MAKING AN AERODYNAMICALLY EFFICIENT CAR BODY FOR THE SAE SUPERMILEAGE COMPETITION," presented at the SAE 2012 World Congress & Exhibition, Detroit, Michigan, United States SAE International, 2012.
- [30] M. Wang, "COMPUTATION OF TRAILING-EDGE AEROACOUSTICS WITH VORTEX SHEDDING," presented at the Center for Turbulence Research, 2005.
- [31] A. Singh, S. Kumar, and K. Nikam, "HIGH PERFORMANCE CFD COMPUTATIONS FOR GROUND VEHICLE AERODYNAMICS," presented at the Symposium on International Automotive Technology, India, SAE International, 2011.
- [32] M. Wang, S. Moreau, G. Iaccarino, and M. Roger, "LES PREDICTION OF WALL-PRESSURE FLUCTUATIONS AND NOISE OF A LOW-SPEED AIRFOIL," *International Journal of Aeroacoustics*, vol. 8, pp. 177-197, 2008.
- [33] G. Wickern and M. Brennerberger, "SCALING LAWS IN AUTOMOTIVE AEROACOUSTICS," presented at the SAE World Congress & Exhibition, Detroit, Michigan, United States SAE International, 2009.
- [34] N. M. Murad, J. Naser, F. Alam, and S. Watkins, "COMPUTATIONAL AEROACOUSTICS OF VEHICLE A-PILLAR AT VARIOUS WINDSHIELD RADII," presented at the Fifth International Conference on CFD in the Process Industries, Melbourne, Australia, 2006.
- [35] C. K. W. Tam, "COMPUTATIONAL AEROACOUSTICS AN OVERVIEW," presented at the RTO AVT Symposium on Ageing Mechanisms and Control: Part A – Developments in Computational Aero- and Hydro-Acoustics, Manchester, United Kingdom, 2001.

- [36] J. L. Mead and R. A. Renaut, "HIGH ORDER METHODS FOR PROBLEMS IN COMPUTATIONAL AEROACOUSTICS," *Arizona State University*, pp. 1-3.
- [37] C. K. W. Tam, "COMPUTATIONAL AEROACOUSTICS EXAMPLES SHOWING THE FAILURE OF THE ACOUSTIC ANALOGY THEORY TO IDENTIFY THE CORRECT NOISE SOURCES," *Journal of Computational Acoustics*, vol. 10, pp. 387-405, 2001.
- [38] D. Baeder, T. Indinger, N. Adams, and F. Decker, "COMPARISON OF NUMERICAL SIMULATIONS WITH EXPERIMENTS OF BLUFF BODIES INCLUDING UNDER HOOD FLOW," presented at the SAE 2011 World Congress & Exhibition, Detroit, Michigan, United States, SAE International, 2011.
- [39] H. Lai and K. H. Luo, "LARGE-EDDY SIMULATION AND CONTROL OF CAVITY AEROACOUSTICS," presented at the Conference on Turbulence and Interactions, Porquerolles, France, 2006.
- [40] K. Yamamoto, T. Imamura, and Y. Yokokawa, "PROGRESS ON EXPERIMENTAL AND NUMERICAL RESEARCH FOR SLAT NOISE IN JAXA," *International Journal of Aeroacoustics*, vol. 10, pp. 443-464, 2011.

APPENDICES

Sample BlockMeshDict (CASE 1A)

```
FoamFile
{
  version      2.0;
  format       ascii;
  class        dictionary;
  object       blockMeshDict;
}
// ***** //

convertToMeters 1;

vertices
(
  (-0.1210 -0.0110 -0.1210)
  ( 0.2310 -0.0110 -0.1210)
  ( 0.2310  0.0110 -0.1210)
  (-0.1210  0.0110 -0.1210)
  (-0.1210 -0.0110  0.1210)
  ( 0.2310 -0.0110  0.1210)
  ( 0.2310  0.0110  0.1210)
  (-0.1210  0.0110  0.1210)
);

blocks
(
  hex (0 1 2 3 4 5 6 7) (32 2 22) simpleGrading (1 1 1)
);

edges
(
);

patches
(
  symmetryPlane sides
  (
    (3 7 6 2)
    (1 5 4 0)
    (4 5 6 7)
  )
);
```



```
    (0 3 2 1)
  )

  patch inlet
  (
    (0 4 7 3)
  )

  patch outlet
  (
    (2 6 5 1)
  )
);

mergePatchPairs
(
);

//
*****
//
```

Sample SnappyHexMeshDict (CASE 1A)

```
FoamFile
{
  version      2.0;
  format       ascii;
  class        dictionary;
  object       snappyHexMeshDict;
}

// ***** //

castellatedMesh      true;
snap                 true;
addLayers            true;
autoBlockMesh       false;
blockData            (0.512 0);
crackDetection       true;

// ***** //

geometry
{
  singleflat.stl      //Profile
  {
    type triSurfaceMesh;
  }

  refinementBox1      //Outer box
  {
    type searchableBox;
    min (-0.0220 -0.0110 -0.0165);
    max ( 0.2310  0.0110  0.0165);
  }

  refinementBox2      //Middle box
  {
    type searchableBox;
    min (-0.0110 -0.0110 -0.0110);
    max ( 0.2310  0.0110  0.0110);
  }

  refinementBox3      //Inner box
```

```

{
  type searchableBox;
  min ( 0.0165 -0.0110 -0.0055);
  max ( 0.0440 0.0110 0.0055);
}

refinementBox4          //Stream box
{
  type searchableBox;
  min ( 0.0440 -0.0110 -0.0055);
  max ( 0.2310 0.0110 0.0055);
}
}

// ***** //

castellatedMeshControls
{
  maxLocalCells          2000000;
  maxGlobalCells         64000000;
  minRefinementCells     20;
  nCellsBetweenLevels    3;

  features
  (
  );

  refinementSurfaces
  {
    singleflat.stl
    {
      level (6 6);
    }
  }

  resolveFeatureAngle    -40;
  featureRefineAngle     15;

  refinementRegions
  {
    refinementBox1
    {
      mode inside;

```

```

    levels ((1 3));
}

refinementBox2
{
    mode inside;
    levels ((1 4));
}

refinementBox3
{
    mode inside;
    levels ((1 5));
}

refinementBox4
{
    mode inside;
    levels ((1 5));
}

}

locationsInMesh          ((-0.115 0.120 0.120));
allowFreeStandingZoneFaces true;

include "$FOAM_CONFIG/snappyMesh.castellated";
}

// ***** //

snapControls
{
    featureEdges
    {
    }

    globalFeatureEdges      true;
    globalRegionSnap        true;
    nSmoothPatch             2;
    tolerance                4;
    nRelaxIter               5;
    zoneFeatureSnapping     false;
    directFeatureSnapping   true;
}

```

```

regionFeatureLines      true;
geometryFeatureLines    true;
snapSurfBoundary        true;
collapseTol              0.25;

include "$FOAM_CONFIG/snappyMesh.snap";
}

// ***** //

addLayersControls
{
  layers
  {
    singleflat.stl_CATIASTL
    {
      nSurfaceLayers      3;
      expansionRatio       1.5;
    }
  }

  include "$FOAM_CONFIG/snappyMesh.layers";
}

include "$FOAM_CONFIG/snappyMesh.qualityDict";
include "$FOAM_CONFIG/snappyMesh.misc";

// ***** //

meshQualityControls
{
  minVol      1e-15;
}

//
*****
//

```

Sample LESProperties (CASE 1A)

```
FoamFile
{
  version      2.0;
  format       ascii;
  class        dictionary;
  location     "constant";
  object       LESProperties;
}
// ***** //

LESModel      SpalartAllmaras;

turbulence    on;

printCoeffs   on;

SpalartAllmarasCoeffs
{
  fieldMaps
  {
    nuTilda      nuTilda;
    nuSgs        nuSgs;
  }
  alphaNut      1.5;
  Cb1           0.1355;
  Cb2           0.622;
  Cw2           0.3;
  Cw3           2;
  Cv1           7.1;
  Cv2           5;
  CDES          0.65;
  ck            0.07;
}

delta         smooth;

smoothCoeffs
{
  delta        cubeRootVol;
  cubeRootVolCoeffs
}
```

```
{
  deltaCoeff      1;
}
maxDeltaRatio    1.15;
}

//
*****
//
```

Sample turbulenceProperties (CASE 1A)

```
FoamFile
{
  version      2.0;
  format       ascii;
  class        dictionary;
  location     "constant";
  object       turbulenceProperties;
}
// ***** //

simulationType LESModel;

//
*****
//
```

Sample transportProperties (CASE 1A)

```
FoamFile
{
  version      2.0;
  format       ascii;
  class        dictionary;
  location     "constant";
  object       transportProperties;
}
// ***** //

transportModel      Newtonian;

NewtonianCoeffs
{
}

rho      rho [ 1 -3 0 0 0 0 ]      1.205;

nu      nu [ 0 2 -1 0 0 0 ]      1.58813278e-05;

Cp      Cp [ 0 2 -2 -1 0 0 ]      1006;

Prt      Prt [ 0 0 0 0 0 0 ]      0.85;

lambda      lambda [ 1 1 -3 -1 0 0 ]      0.024;

//
*****
//
```


Sample thermophysicalProperties (CASE 4A)

```
FoamFile
{
  version      2.0;
  format       ascii;
  class        dictionary;
  location     "constant";
  object       thermophysicalProperties;
}
// ***** //

thermoType
hPsiThermo<pureMixture<constTransport<specieThermo<hConstThermo<perfectGas>>
>>>;

mixture      air 1 28.9 1007 0 1.84e-05 0.7;

//
*****
//
```

Sample controlDict (CASE1A)

```
FoamFile
{
  version      2.0;
  format       ascii;
  class        dictionary;
  location     "system";
  object       controlDict;
}
// ***** //

startFrom      startTime;
startTime      0;
stopAt         endTime;
endTime        0.275;
deltaT         1.25e-05;
writeControl   timeStep;
writeInterval  10;
purgeWrite     2;
writeFormat    ascii;
writePrecision 10;
writeCompression compressed;
timeFormat     general;
timePrecision  6;
graphFormat    raw;
runTimeModifiable yes;
libs           ( "libturbTools.so" );
adjustTimeStep no;
maxCo          1;
maxDeltaT      1;
application    pisoFoam;

functions
(
  blendingFactors
  {
    functionObjectLibs ( "libturbTools.so" );
    phiName            phi;
    verbose            yes;
    stabilised         10;
    meshQuality
    {
```

```

    }
    fieldCoefficients      ( ( U 2 ) );
    region                 region0;
    type                   cflBlendingFactor;
}

courant
{
    functionObjectLibs    ( "libturbTools.so" );
    logToFile             true;
    region                region0;
    type                  courant;
}

volumeReport
{
    functionObjectLibs    ( "libsampling.so" );
    logToFile             true;
    fields                ( U p nuTilda );
    region                region0;
    type                  volumeReport;
}

liftDrag
{
    liftDragPatches
    {
        partialNamed      ( );
        exactNamed        ( singleflat.stl_CATIASTL );
    }
    functionObjectLibs    ( "libturbTools.so" );
    porosity              true;
    nAveragingSteps       1;
    outputRegionData      false;
    binData
    {
        nBins              10;
        axis                ( 1 0 0 );
    }
    maxCp                 1e+15;
    minCp                 -1e+15;
    Uinf                  ( 28 0 0 );
    rhoInf                1.165;
}

```

```

liftDirection      ( 0 0 1 );
dragDirection      ( 1 0 0 );
referenceArea      0.0005016;
referenceLength    0.0228;
referencePoint     ( -0.115 0.12 0.12 );
wheelbase         0.0228;
region            region0;
type              liftDrag;
}

Probes
{
  functionObjectLibs    ( "libsampling.so" );
  probeLocations        ( ( 0.0575 0 0 ) ( 0.0513372 0 0.023 ) ( 0.0345 0 0.0398372
) ( 0.0115 0 0.046 ) ( -0.0115 0 0.0398372 ) ( -0.0283372 0 0.023 ) ( -0.0345 0 0 ) ( -
0.0283372 0 -0.023 ) ( -0.0115 0 -0.0398372 ) ( 0.0115 0 -0.046 ) ( 0.0345 0 -0.0398372 )
( 0.0513372 0 -0.023 ) );
  fields                ( p U );
  region                region0;
  type                  volProbes;
}

)
;

//
*****
//

```

Sample fvSchemes (CASE 1A)

```
FoamFile
{
  version      2.0;
  format       ascii;
  class        dictionary;
  location     "system";
  object       fvSchemes;
}
// *****

ddtSchemes
{
  default      backward;
}

gradSchemes
{
  default      Gauss linear;
  grad(nuTilda)  cellLimited Gauss linear 1;
  grad(k)      cellLimited Gauss linear 1;
  grad(kl)     cellLimited Gauss linear 1;
  grad(omega)  cellLimited Gauss linear 1;
  grad(epsilon) cellLimited Gauss linear 1;
}

divSchemes
{
  default      Gauss linear;
  div(phi,U)   Gauss localBlended filteredLinear2V 0.5 0 upwind;
  div(phi,k)   Gauss linearUpwind cellLimited Gauss linear 1;
  div(phi,epsilon) Gauss linearUpwind cellLimited Gauss linear 1;
  div(phi,omega) Gauss linearUpwind cellLimited Gauss linear 1;
  div(phi,nuTilda) Gauss linearUpwind cellLimited Gauss linear 1;
  div(phi,kl)  Gauss limitedLinear 1;
  div(phi,R)   Gauss upwind;
  div(R)       Gauss linear;
  div((nuEff*dev(grad(U).T()))) Gauss linear;
}

interpolationSchemes
{
```

```
    default    linear;
}

laplacianSchemes
{
    default    Gauss linear limited 0.333;
}

snGradSchemes
{
    default    limited 0.333;
}

fluxRequired
{
    default    no;
    p          ;
}

//
*****
//
```

Sample fvSolution (CASE 1A)

```
FoamFile
{
  version      2.0;
  format       ascii;
  class        dictionary;
  location     "system";
  object       fvSolution;
}
// ***** //

SIMPLE
{
  nNonOrthogonalCorrectors  0;
  pressureImplicitPorosity  false;
  pRefCell                   0;
  pRefValue                   0;
  pdRefCell                   0;
  pdRefValue                   0;
}

solvers
{
  p
  {
    solver              GAMG;
    agglomerator         faceAreaPair;
    mergeLevels         1;
    cacheAgglomeration  true;
    nCellsInCoarsestLevel  200;
    tolerance            1e-10;
    relTol               0.01;
    smoother             GaussSeidel;
    nPreSweeps           0;
    nPostSweeps          2;
    nFinestSweeps        2;
  }
  U
  {
    solver              smoothSolver;
    smoother            GaussSeidel;
    tolerance            1e-06;
  }
}
```

```

    relTol                0;
}
k
{
    solver                smoothSolver;
    smoother              GaussSeidel;
    tolerance              1e-06;
    relTol                0;
}
kl
{
    solver                smoothSolver;
    smoother              GaussSeidel;
    tolerance              1e-06;
    relTol                0;
}
epsilon
{
    solver                smoothSolver;
    smoother              GaussSeidel;
    tolerance              1e-06;
    relTol                0;
}
R
{
    solver                smoothSolver;
    smoother              GaussSeidel;
    tolerance              1e-06;
    relTol                0;
}
nuTilda
{
    solver                smoothSolver;
    smoother              GaussSeidel;
    tolerance              1e-06;
    relTol                0;
}
omega
{
    solver                smoothSolver;
    smoother              GaussSeidel;
    tolerance              1e-06;
    relTol                0;
}

```



```

}
h
{
    solver          smoothSolver;
    smoother        GaussSeidel;
    tolerance        1e-06;
    relTol          0;
}
T
{
    solver          smoothSolver;
    smoother        GaussSeidel;
    tolerance        1e-06;
    relTol          0;
}
rho
{
    solver          PCG;
    preconditioner  DIC;
    tolerance        0;
    relTol          0;
}
pFinal
{
    solver          GAMG;
    agglomerator    faceAreaPair;
    mergeLevels     1;
    cacheAgglomeration true;
    nCellsInCoarsestLevel 200;
    tolerance        1e-06;
    relTol          0.0001;
    smoother        GaussSeidel;
    nPreSweeps      0;
    nPostSweeps     2;
    nFinestSweeps   2;
}
}

relaxationFactors
{
    p          1;
    pd         1;
    U          1;
}

```

```

k            1;
kl           1;
epsilon      1;
R            1;
nuTilda     1;
omega        1;
h            1;
rho          1;
T            1;
}

PISO
{
  nCorrectors                3;
  nNonOrthogonalCorrectors   0;
  pressureImplicitPorosity    false;
  pRefCell                    0;
  pRefValue                    0;
  pdRefCell                    0;
  pdRefValue                    0;
  pMin                         pMin [ 1 -1 -2 0 0 0 ] 100;
}

//
*****
* //

```

VITA AUCTORIS

NAME	Tyler Bevan
PLACE OF BIRTH	Windsor, Ontario
YEAR OF BIRTH	1984
EDUCATION	Belle River District High School, Belle River, Ontario 1998-2003 St. Clair College, Windsor, Ontario 2003-2006, Diploma University of Windsor, Windsor, Ontario 2007-2009, B.A.Sc. University of Windsor, Windsor, Ontario 2009-2013, M.A.Sc. Politecnico Di Torino, Torino, TO, Italy 2011-2013, M.A.Sc.